2-DIMENSIONAL COMPUTATIONAL FLUID DYNAMIC MODELING ON COMSOL MULTIPHYSICS OF FISCHER TROPSCH FIXED BED REACTOR USING A NOVEL MICROFIBROUS CATALYST AND SUPERCRITICAL REACTION MEDIA

A Thesis

by

AYA EMHEMED ABUSRAFA

Submitted to the Office of Graduate and Professional Studies of
Texas A&M University
in partial fulfillment of the requirements for the degree of

MASTER OF SCIENCE

Chair of Committee,	Nimir Elbashir
Co-Chair of Committee,	Patrick Linke
Committee Member,	Ibrahim Hassan
Head of Department,	Arul Jayaraman

December 2019

Major Subject: Chemical Engineering

ABSTRACT

Fischer Tropsch synthesis (FT) is a highly exothermic catalyzed reaction to produce a variety of hydrocarbon products and value-added chemicals. To overcome the limitations associated with conventional FT reactors, utilizing high conductivity catalytic structures consisting of microfibrous entrapped cobalt catalyst (MFECC) has been proposed to enhance heat removal from the reactor bed. Additionally, utilization of supercritical fluids (SCF-FT) as a reaction media with liquid-like heat capacity and gas-like diffusivity have been employed to mitigate hot spot formation in FT reactors.

The objective of the present study is to investigate the performance of FT Fixed bed/PB reactors operating using SCF-FT as a reaction media and MFECC structures using a conventional cobalt-based catalyst in terms of thermal management, syngas conversion, and product selectivity. A 2-D Computational Fluid Dynamics (CFD) model of an FT reactor was developed in COMSOL® Multiphysics v5.3a for three systems; non-conventional MFECC bed and conventional PB under gas-phase conditions (GP-FT) and non-conventional PB in SCF-FT media. The potential of scaling-up a typical industrial 1.5" diameter reactor bed to a larger tube diameter (up to 4” ID) was studied as a first step towards process intensification of the FT technology. An advantage of increasing the tube diameter is that it allows for the use of higher gas flow rates, thus enabling higher reactor productivity and a reduction in the number of tubes required to achieve a targeted capacity. The high fidelity 2-D model developed in this work was built on experimental data

generated at a variety of FT operating conditions both in conventional GP-FT operation and in SCF-FT reactor bed.

Results showed that the MFECC bed provided excellent temperature control and low selectivity toward undesired methane (CH_4) and high selectivity toward the desired hydrocarbon cuts (C_{5+}). For the 4" diameter, the maximum temperature rise in the MFECC bed was always 2% below the inlet operational temperature. However, in PB the temperature can go up to 53% higher than the inlet temperature. This resulted in 100% selectivity toward methane and 0% selectivity toward the higher hydrocarbon cuts (C_{5+}). On the other hand, the CH_4 selectivity in the MFECC case was maintained below 24%, while the C_{5+} selectivity was higher than 70%. Similarly, the maximum temperature rise in SCF-FT for a 4” ID bed was just 15 K compared to ~800 K in GP-FT bed. The enhancement in thermal performance in the SCF-FT reactor bed is attributed to the high thermal capacity of SCF media (~2500 J/kg/K) compared to the GP media (~1300 J/kg/K), which resulted in the elimination of hotspot formation.

DEDICATION

I dedicate this thesis to my dear parents, who have always been a constant source of support and compassion throughout my whole life, who always taught me to work hard for my goals and aspired me to reach the place am I now. Thank you very much for everything.

ACKNOWLEDGEMENTS

I would like to express my thanks to my thesis supervisor, Prof. Nimir Elbashir, for his continuous guidance and support throughout this research. His motivation, excitement, useful comments and remarks toward this work has made this an unforgettable experience and a great learning opportunity. I would also like to thank my mentors Mr. Mohamed S. Challiwala and Dr. Hanif Choudhury, who were always available whenever I ran into a trouble spot or had enquires about my research. I am very grateful for Prof. Elbashir's research group who were always committed to help and to provide useful advice and tips to improve this research outcome. I would also like to acknowledge Dr. Ben Wilhite for his cooperation in the model development, for which I thank him.

Thanks for all my dear friends and colleagues and the department faculty and staff for making my time at Texas A&M University a great experience.

Finally, thanks to my parents for their continuous advice, encouragement and patience, and for always being there for me whenever I ran into life difficulties and obstacles to make sure I always followed the right path.

CONTRIBUTORS AND FUNDING SOURCES

Contributors

This work was done under the supervision of the dissertation committee consisting of Professor Nimir Elbashir and Patrick Linke from the Department of Chemical engineering and Professor Ibrahim Hasan from the Department the mechanical engineering department

The model was developed with the help of Mr. Mohamed Sufiyan Challiwala and Dr. Bejamin Wilhite. The experimental campaign for supercritical Fischer-Tropsch was done in Professor Elbashir's lab at Texas A&M University at Qatar and by Dr. Hanif Choudhury and Mr. Mohamed Sufiyan Challiwala.

All other work conducted for the thesis was completed by the student independently.

Funding Sources

Graduate study was supported by a fellowship from Texas A&M University at Qatar. This work was also made possible in part by a grant from Qatar National Research Fund (QNRF) under Grant Number (7-865-2-320) and NPRP exceptional grant award [NPRP-EP X-100-2-024].

NOMENCLATURE

α Chain growth probability

α_i Parameter in MSRK Eos

$\alpha_{w,int}$ Heat transfer coefficient from the bed to the inner wall of the tube, [W/m^2/K]

$\alpha_{w,ext}$ Heat transfer coefficient from the tube wall to the cooling liquid, [W/m^2/K]

ϵ_{bed} Bed porosity

κ_{bed} Bed permeability, [m^2]

μ_f Fluid viscosity, [Pa. s]

$\emptyset_p$ Sphericity

λ_{er} Effective radial heat coefficient [W/m/K]

λ_w Thermal conductivity of reactor wall, [W/m/K]

γ_i Parameter in MSRK Eos

ρ_f Density of the fluid mixture [kg/m^3]

α_n Chain growth probability n C-atoms

α_i Parameter in MSRK Eos

$\alpha_{w,int}$ Heat transfer coefficient from the bed to the inner wall of the tube

$\alpha_{w,ext}$ Heat transfer coefficient from the tube wall to the cooling liquid

ϵ_{bed} Bed porosity

κ_{bed} Bed permeability

μ_f Fluid viscosity

μ_i Pure component viscosity

$\emptyset_p$ Sphericity

$\emptyset_{ij}$ Dimensionless energy parameter

λ_{er} Effective radial heat coefficient

λ_w Thermal conductivity of reactor wall

γ_i Parameter in MSRK Eos

ρ_f Density of the fluid mixture

ρ_i Pure component density

a_0 Pre-exponential kinetic parameter

a_M Reaction order of CO

a_{ii} Binary interaction parameter between species (i) in a mixture

a_{ij} Binary interaction parameter between species (i) and (j) in a mixture

a_m Parameter in MSRK Eos

A_k Pre-exponential factor

A_a Pre-exponential factor

$\mathrm{A_M}$ Pre-exponential factor

b_m Parameter in MSRK Eos

b_M Reaction order of H_2,

β_f Forchheimer drag coefficient

b_{ii} Binary interaction parameter between species (i) in a mixture

b_{ij} Binary interaction parameter between species (i) and (j) in a mixture

b_0 Pre-exponential kinetic parameter

$C_{p,f}$ Fluid heat capacity

C_{p_s} Solid heat capacity

C_p Heat capacity within the reactor bed

Cp_i Pure component molar heat capacity

c_{ij} Binary interaction parameter between species (i) and (j) in a mixture

d_k Diffusional driving force of species

d_p Average particle diameter

d_t Tube diameter

d_w Wall thickness

D_{ik} Binary pair Maxwell Stefan diffusivities

$\mathrm{E_k}$ Activation energy factor in kinetic expression

E_a Activation energy factor in kinetic expression

$\mathrm{E_M}$ Activation energy factor in kinetic expression

f_{co} Fugacity of CO

f_{H_2} Fugacity of H_2

j_i Diffusive flux vector

k Kinetic parameter

k_{ij} Binary interaction parameter between species (i) and (j) in a mixture

K_1, K_2, K_3 Kinetic parameters

k_{eff} Effective bed thermal conductivity

k_s Thermal conductivity of solid phase

k_M Kinetic parameter

k_{bed} Thermal conductivity of the bed

k_f Thermal conductivity of fluid phase

K_i Equilibrium constants

k_i Kinetic rate constants

k_i Pure component thermal conductivity

MW_i Molecular weight of species (i)

$\dot{m}$ Mass flow rate

m_i Parameter in MSRK Eos

m_M Water effect coefficient

n Carbon number

N_i Total flux of species i

p Local reactor pressure

P_{co} Partial pressure of CO

P_{H_2} Partial pressure of H_2

$P_{c,i}$ Critical pressure of species (i)

Pr Prandtl number

Q Heat source or sink

q Conductive heat flux

r Radial dimension

r_{bed} Bed radius

$-R_{CO}{}^{\mathrm{YS}}$ Rate of carbon monoxide consumption (Yates and Satterfield model)

$R_{CH_4}{}^{Ma}$ Rate of formation of methane (Ma model)

$-R_{H_2}$ Rate of hydrogen consumption

R_{H_2O} Rate of water formation

$R_{C_2H_4}{}^{\mathrm{Prod}}$ Rate of ethene formation according to detailed kinetics

$R_{C_nH_{2n+2}}{}^{\mathrm{Prod}}$ Rate of n-paraffin formation according to detailed kinetics

$R_{C_nH_{2n}}{}^{\mathrm{Prod}}$ Rate of 1-olefins formation according to detailed kinetics

R_i Rate of consumption or production of species i

Re_{pa} Reynolds number

R Universal gas constant

$[S]$ Fraction of vacant sites

T, T_c Local temperature/ Coolant Temperature

$T_{c,i}$ Critical temperature of species (i)

$\mathbf{u}$ Local velocity vector

$U_{overall}$ Overall heat transfer coefficient

$V_{c,i}$ Molar volume of species (i)

ν_i Stoichiometry coefficient of species (i)

w_i Weight fraction of each species (i)

ω_i Acentric factor

x_i Mole fraction of species (i)

z Axial dimension

ΔH_{rxn} Enthalpy of FT reaction

Z Compressibility factor

TABLE OF CONTENTS

Page

LIST OF FIGURES

Page

LIST OF TABLES

Page

1. INTRODUCTION

The global energy demand is increasing at a fast rate, as the world's population is growing and the economy is developing [1]. Extensive research has been done over the past years to find clean energy resources to minimize the impact on the environment. Even though clean energy alternatives such as renewables including solar and wind have been applied to reduce the world's dependence on fossil fuels; coal, crude oil, and natural gas will continue to be the main energy sources in the following years. Currently, coal, crude oil and natural gas cover around 85% of the total global energy demand [2]. Of the three energy sources, natural gas is the fastest growing energy source per annum. The contribution of natural gas in the total global energy sources has increased by 40% from 1995 to 2017 [3]. In 2011, the International Energy Agency (IEA) reported that the world demand for natural gas is expected to rise by more than 50% by 2035 [4]. EIA also reported that the natural gas consumption/demand is estimated to increase by 1.9% per annum as shown in Figure 1 [5]. This considerable growth is mainly due to the large availability of shale gas reserves and the abundant natural gas production from the Middle East fields [6, 7]. Moreover, natural gas is a cleaner source of energy and has a less environmental impact than crude oil and coal. Thus, the environmental policies implemented by many developing countries nowadays facilitated the growth of natural gas exploration and consumption. However, one of the main drawbacks associated with natural gas is difficult accessibility through pipelines to remote markets.

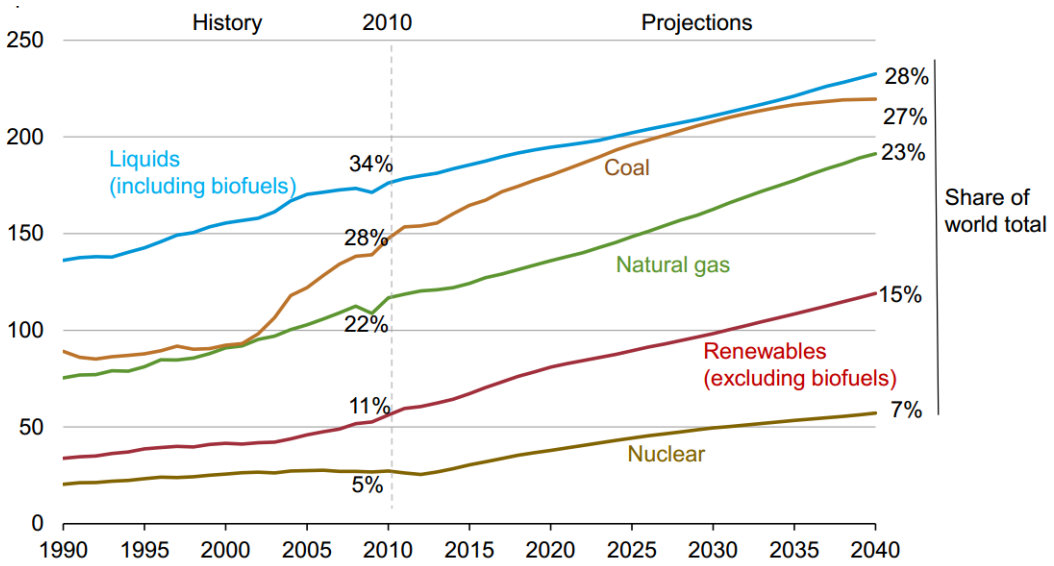

Figure 1: World energy consumption based on energy source 1990-2040 reprinted from [5].

With the increase in natural gas consumption and the abundance in natural gas reserves, there is a global demand to develop efficient and economical gas processing technologies for the production of high-value chemical products, and easily-transportable hydrocarbons [8, 9]. Gas to liquid processing (GTL), has become a viable option for monetizing remote natural gas toward the production of liquid fuels and value-added chemicals like olefins, oxygenates and others through Fischer Tropsch synthesis (FT). The increased interest in GTL process is mainly due to its ability to produce a variety of ultraclean fuels without aromatic, sulfur, or nitrogen compounds, which are more environmentally friendly than products emerging from crude oil [10, 11]. Moreover, in view of the depletion in oil reserves, the fluctuating oil prices and the continuous discovery of shale gas and natural gas reserves, the demand for natural gas will continue. This can be seen in Figure 2, which shows the past and the prospected demand for natural gas in

different countries around the globe. Therefore, the GTL process will continue to gain significant interest from the industrial and scientific community, offering the global market diversification to remote natural gas reserves [12, 13].

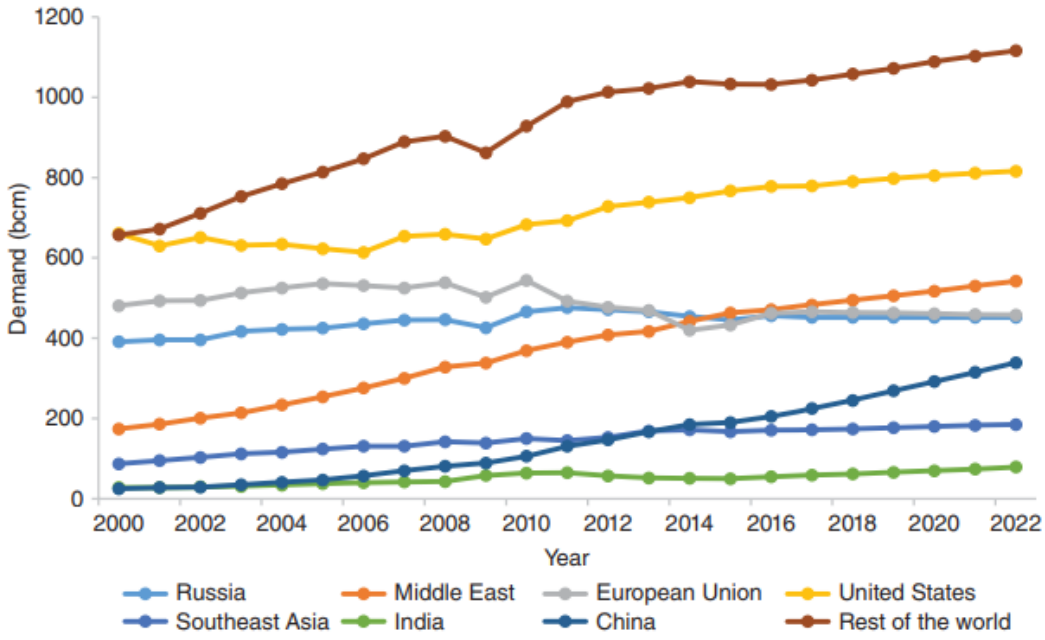

Figure 2: The past and the prospected demand for natural gas in different countries reprinted from [3].

The GTL process as shown in Figure 3 consists of three main steps: a) Natural gas conversion to synthesis using steam reforming, autothermal reforming or partial oxidation, b) Conversion of synthesis gas to liquid hydrocarbons through Fischer Tropsch synthesis (FT), c) product-upgrading steps involving hydrocracking, hydroisomerization, etc.

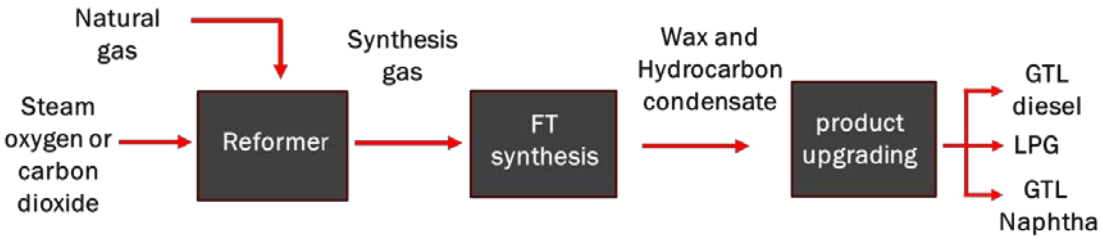

Figure 3: Schematic of the overall GTL process.

1.1. Literature review

1.1.1. Syngas production

Natural gas reforming or methane reforming is a key step toward the production of synthesis gas (a mixture of hydrogen (H_2) and carbon monoxide (CO)), which is a feedstock for the various chemical processes including FT synthesis [14]. As mentioned previously there are currently three technologies that are commercially employed for methane reforming including; steam reforming (SRM), autothermal reforming (ARM) or partial oxidation (POX). Steam reforming is the dominant process for producing synthesis gas since it is a well-established technology. The feed to SRM consists of a mixture of hydrocarbons mainly methane and steam (H_2O). In this process, the H_2/CO ratio is typical ≥ 3, but the required H_2/CO ratio for the FT process is 2. Partial oxidation has also gained significant interest for industrial applications, where oxygen (O_2) reacts with methane to produce synthesis gas as a result of the incomplete combustion of methane. SRM is favored over POX since no air separation unit is required to obtain pure oxygen [15]. Autothermal reforming combines both the POX and SRM process, where methane is partially oxidized with hydrogen with the addition of steam. H_2/CO ratio obtained using the ARM technology is ~2.5. Moreover, other than the conventional SRM, ARM and

POX conventional processes, dry reforming of methane (DRM), which utilizes carbon dioxide (CO_2) to react with methane is another route toward the production of synthesis gas. In contrast to conventional reforming processes, DRM has great potential toward effective utilization and fixation of CO_2. Due to environmental concerns on greenhouse gas emissions, DRM has gained significant attention from the scientific community. However, the commercialization of DRM has been obstructed due to the limitations associated with the process. One of the main limitations is the high energy requirement which is around 1.2 times higher than that in the SRM, due to the endothermic nature of the DRM reaction[16]. Therefore, DRM is normally conducted at higher operating temperatures which promotes carbon deposition, leading to catalyst deactivation [17, 18]. Moreover, the H_2/CO ratio in DRM is typical ~ 1 (low-quality synthesis gas). A summary of the natural gas reforming technologies described earlier is presented in Table 1.

Table 1: Natural gas reformers

Technology	Description
Steam methane reforming (SMR)	An exothermic reaction in which methane and steam react to produce syngas $CH_4 + H_2O \leftrightarrow CO + 3H_2 \quad \Delta H_{298} = 206 \frac{kJ}{mol}$
Partial oxidation (POX)	An exothermic reaction in which methane and oxygen react to form syngas. $CH_4 + 0.5O_2 \leftrightarrow CO + 2H_2 \quad \Delta H_{298} = -35.2 \frac{kJ}{mol}$
Autothermal reforming (ATR)	This technology combines both the SRM and POX processes where oxygen and steam react in an endothermic reaction with methane to produce syngas. $CH_4 + H_2O \leftrightarrow CO + 3H_2 \quad \Delta H_{298} = 206 \frac{kJ}{mol}$ $CH_4 + 0.5O_2 \leftrightarrow CO + 2H_2 \quad \Delta H_{298} = -35.2 \frac{kJ}{mol}$

Table 1 continued

Technology	Description
Dry reforming of methane (DRM)	$CH_4 + H_2O \leftrightarrow 2CO + 2H_2 \qquad \Delta H_{298} = 247 \frac{kJ}{mol}$

1.1.2. Fischer Tropsch synthesis

The interest in Fischer Tropsch synthesis has significantly grown over the last century as a consequence of environmental regulations, technological developments and changes in fossil energy reserves. The history of Fischer Tropsch synthesis trades back to the beginning of the 20^{th} century. In the early 1920s, industrialized nations including Germany, France, Italy, and other couriers were mainly dependent on crude oil to drive their economies. However, in the period before and during World War II, Germany had faced a lack of oil supply since it did not have reserves of its own but was rich in coal. For that reason, the German government has supported research driven toward the production of synthetic oils through coal-to-liquids (CTL) process as a substitute for crude oil, to be used for its military machines.

The FT process was first invented by two German scientists; Franz Fischer (187-1947) and Hans Tropsch (1889-1935) in 1923 at the Kaiser Wilhelm Institute for Coal Research (KWI) in Mulheim [6, 19]. Fischer and Tropsch had discovered that under certain temperature and pressure conditions (400 ^{o}C, 100 atm), carbon monoxide (CO) and hydrogen (H_2) react to form liquid hydrocarbons over Iron catalysts [20]. They also synthesized high weight hydrocarbons over Fe_3O_4-ZnO catalysts at 370 C^{o} and 1 atm [21]. This was the first step toward developing the FT process. Later, studies focused on using cobalt and nickel catalysts due to the rapid deactivation rate of iron catalysts. In the early 1930s, Fischer and Meyer developed Ni-ThO2-Kieselguhr and Co-ThO2-Kieselguhr catalysts [22]. However, studies revealed that Nickel-based catalysts were highly selective

toward methane and as a result the focus has been shifted toward the cobalt-based catalysts.

The industrial application of the FT process took place in Germany during the 1930s. The first pilot-scale FT plant was constructed in Mulheim in 1932 [6]. After that, an industrial scale FT plant was built by Ruhrchemie A.G in Oberhausen, Germany in 1934 with a capacity of about 200 bbl/day [23]. During the same time, research on the FT process continued to find improved catalyst performance. In 1937, Fischer and Pichler discovered that at medium pressure conditions (5-30 atm) alkalized iron catalysts can provide better product yield and catalyst longevity [24]. In 1938, Picher observed the formation of hydrocarbon waxes over a ruthenium-based catalyst which was also proven to be active for the FT process [25].

By 1944, there were nine industrial sized FT facilities in operation with a total production of about 660×10^3 tons per annum [26]. At that time, FT products accounted for about 9-15% of the total production capacity in Germany. Although these plants were shut down after World War II, the interest in FT continued because there was a general perception that the oil reserves are very limited and will be depleted fast or the price of crude oil will rise.

In 1950, the first GTL plant utilizing an iron-based catalyst was constructed in Brownsville, Texas with a capacity of 7000 bbl/day [27]. However, the plant was shut down in the late 1950s due to the increase in the price of natural gas at that time. During the same period in 1955, an FT plant was constructed in Sasolburg, South Africa utilizing a cobalt-based catalyst by the South Africa Coal Oil and Gas Cooperation (Sasol 1 plant).

The interest in the FT process was mainly driven by the availability of cheap coal in South Africa. At that time, huge oil fields were discovered in the middle east which lead to a sharp decrease in oil prices[6]. However, Sasol 1 continued to operate and was able to withstand the decreasing interest in the FT process due to the ample supply of cheap oil from the Middle East.

The fluctuating prices of crude oil over the years (Figure 4) has made the FT process a viable alternative toward the production of value-added chemicals only when the price of crude oil was high. Therefore, investment in new FT plants was risky. Nevertheless, research on FT continued especially in countries that were rich in coal reserves. The oil crisis during the 1970s, supported Sasol to expand the Sasolburg plant by constructing two additional coal-based plants in South Africa, with a combined capacity of about 6×10^6 tons per annum for the three Sasol plants. The two new plants began operation in 1980 and 1982.

With the discovery of cheap natural reserves two new GTL plants were constructed, the first in 1992 by Shell in Bintulu, Malaysia utilizing a cobalt-based catalyst with an overall capacity a 5×10^5 tons per annum [26, 28]. The second plant was constructed in 1993 by PetroSA in Mossel Bay, South Africa utilizing an iron-based catalyst with an overall capacity a 1×10^6 tons per annum [20]. The profitability of the two new plants was low due to the low oil prices in the mid-1990s. However, in 1999 the price of crude oil increased sharply to above 30$ and the interest in commissioning new FT plans continued ever since.

Currently, the State of Qatar hosts two of the world's largest GTL facilities, the world largest GTL plant is owned jointly by Shell and Qatar Petroleum (the Pearl GTL plant) and the other plant, the ORYX GTL plant is owned jointly by Qatar Petroleum and Sasol with an overall capacity exceeding 180,000 barrels per day [29]. Since natural gas has become the one most growing energy resource nowadays, the demand for clean fuels and chemicals from synthesis gas using natural gas as a feedstock will continue to grow.

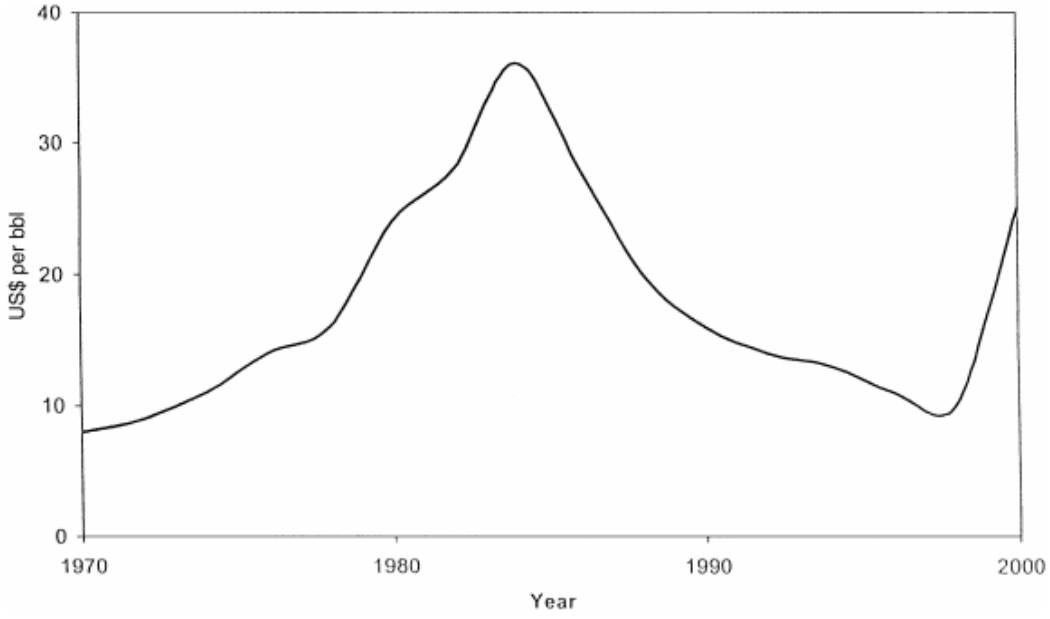

Figure 4: Variation in oil prices reprinted from [26]

1.1.2.1. Fischer Tropsch chemistry

Fischer Tropsch (FT) synthesis, which is the heart of the GTL process, is surface catalysed polymerization reaction in which synthesis gas is converted to a variety of hydrocarbons mainly paraffin and olefin products according to the following reactions [30-34].

$$nCO + (2n + 1)H_2 \rightarrow C_nH_{(2n+2)} + nH_2O \quad \text{(synthesis of paraffin)} \qquad (1)$$

$$nCO + 2nH_2 \rightarrow C_nH_{2n} + nH_2O \quad \text{(synthesis of olefins)} \qquad (2)$$

The main reactions (Eqs. 1 and 2), are highly exothermic, with around 140-160 KJ per mole of CO consumed [35]. Oxygenates (Eq. 3) are also formed in small amounts.

$$nCO + 2nH_2 \rightarrow C_nH_{(2n+1)}OH + (n-1)H_2 \quad \text{(synthesis of oxygenates)} \qquad (3)$$

Under FT synthesis conditions, undesirable side reactions occur in sequence and in parallel to the main reactions. This includes the reaction of the co-product H_2O with CO to produce carbon dioxide through the water/gas shift reaction (WGS) (Eq. 4).

$$CO + H_2O \leftrightarrow CO_2 + H_2 \qquad (4)$$

Other notable undesirable side reactions are the production of methane (Eq. 5) and carbon (Boudouard reaction Eq. 6).

$$CO + 3H_2 \rightarrow CH_4 + H_2O \qquad (5)$$

$$2CO \rightarrow C + CO_2 \qquad (6)$$

As depicted from the reactions above, a various range of hydrocarbon products are generated during the FT reaction ranging from C_1 (methane) up to $C_{100,}$ depending on the

catalyst used and the process conditions. This occurs due to the step-wise addition of the CH_x monomer into a growing aliphatic chain [32]. The polymerization reaction for FT synthesis follows a complex mechanism, thus predicting the product distribution is quite difficult. For this reason, the reaction mechanism that accurately describes the elementary steps during the FT reaction is still a subject of debate in the research community. The development and use of different catalysts have led to the proposal of various reaction mechanisms that attempt to accurately describe the steps involved in the FT reaction including; alkyl mechanism, CO insertion mechanism, carbide mechanism, and alkenyl mechanism. However, it has been agreed that the polymerization reaction follows a sequence of steps (as shown in Figure 5): 1) reactant adsorption; 2) chain initiation; 3) chain propagation; 4) chain termination; 5) product desorption; 6) readsorption and secondary reactions of the formed products [36, 37].

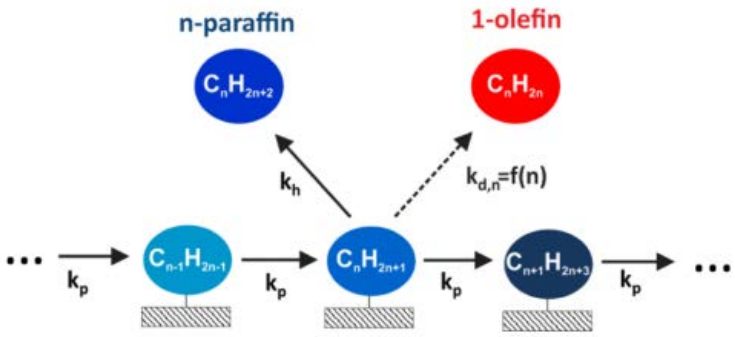

Figure 5: Schematic of chain propagation, readsorption, and secondary reactions during the FT reaction reprinted from [38]

The product distribution of the paraffin and olefins is described by the Anderson-Schulz Flory distribution (ASF) [39]. The ASF model quantifies the mole fraction of a certain carbon number in terms of the chain growth probability (α) as shown in Eq 7.

$$w_n = n(1-\alpha)^2\alpha^{n-1} \quad (7)$$

where x_n is the mole fraction of a hydrocarbon with n carbon atoms.

The relation between the weight fractions of the hydrocarbon products with respect to carbon number and the α value is presented in Figure 6. The chain growth probability mainly depends on the rates of propagation and the rate of termination and is independent of the carbon number (Eq. 8).

$$\alpha = \frac{r_p}{r_p + r_t} \quad (8)$$

where r_p is the rate of chain propagation and r_t is the rate of chain termination [32, 40].

The ASF model portrays that higher chain growth probability values indicate high selectivity toward heavy hydrocarbon products.

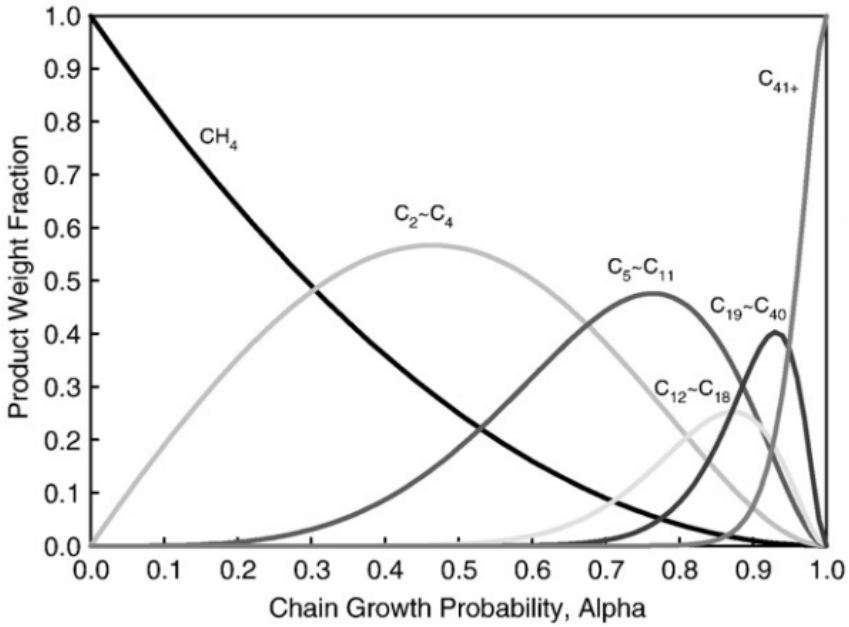

Figure 6: Product distribution by Fischer–Tropsch synthesis depending on chain growth probability reprinted from [10]

The typical ASF distribution with respect to carbon number follows a straight line with a constant slope representing the chain growth probability as shown in Figure 7a. However, it has been well demonstrated in the literature that the hydrocarbon selectivity deviates from the typical ASF model which can be seen from the non-ASF behavior in Figure 7a. Three main deviations have been observed a) higher than expected yield of methane, lower than expected yield of C_2 cuts (Mainly ethene) and an increased selectivity toward heavier hydrocarbons, which indicates the dependency of the chain growth probability on the carbon number [41, 42]. Many explanations for the latter deviations have been proposed in the literature. Out of the most well-known explanations are the secondary reactions of 1-olefins [43-47]. This theory assumes that 1-olefins are reabsorbed on the surface of the catalyst, which either contributes to the chain growth or undergoes

further hydrogenation to form n-paraffin [38]. The latter results in the production of higher weight hydrocarbons mainly paraffin, which explains the decreasing trend in olefin to paraffin ratio with carbon number (Figure 7b).

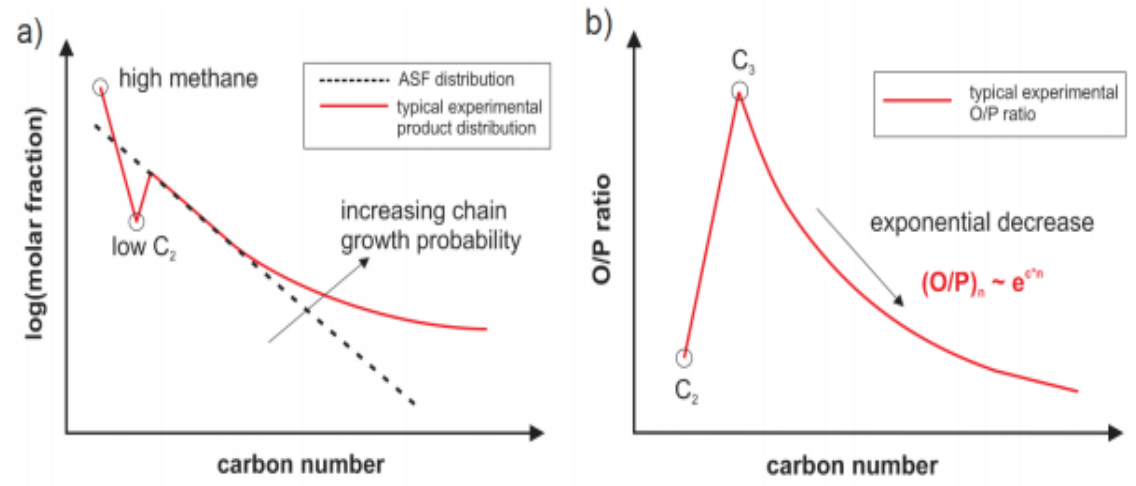

Figure 7: Typical ASF and non-ASF FT product distribution over cobalt-based catalyst reprinted from [48]

To develop cost-effective and efficient FT processes, the amount of low weight hydrocarbons particularly methane needs to be minimized, while the amount of C_{5+} components needs to be maximized (operating at high α values > 0.8). The main factors affecting the product selectivity are the catalyst type, process conditions, and reactor configuration. Therefore, a thorough understanding of the effect of those factors on the FT process is required to develop catalysts and reactor technologies that can tune the selectivity of the desired FT products.

1.1.2.2. Fischer Tropsch catalysts

The typical metals that are active as Fischer Tropsch catalysts are Iron (Fe), Cobalt (Co), Nickel (Ni) and Ruthenium (Ru) [6, 45]. The selection of the FT catalyst is made on the basis of catalyst cost, catalyst activity, selectivity, and feedstock used to produce syngas. Amongst all the metals, Ru is the most active FT catalyst, capable of operating at a low temperature < 150^{o}C [49], producing long-chain hydrocarbons. However, high costs and limited availability hinders its industrial applications[50]. Ni has a high hydrogenation activity and therefore has a high selectivity towards methane, which is counterproductive to the FT process [49]. Thus, Co and Fe are the only two metals that are currently used in the industry. Fe is the cheapest, and has low selectivity toward higher weight hydrocarbons and produces a high amount of olefins and oxygenates [50]. In addition, Fe exhibits a high activity toward the WGS, hence are suitable for FT process with low H_2 to CO ratio (H_2/CO molar ratio ~ 1), which is obtained from the reforming of coal or heavy oil. The activity of Fe declines due to product inhibition by water [51]. Moreover, Fe is subject to deactivate at a faster rate compared to Co. Generally, Fe requires more modifications such as the addition of promoters to attain good selectivity and stability. Co is more expensive than Fe, however, it is more active under low temperatures and has high selectivity to long chain paraffinic compounds and is more resistant to deactivation. Moreover, Co catalyst work well under selected H_2/CO molar ratios typically 2 and are therefore used when the feedstock for synthesis gas production is natural gas.

1.1.2.3. Fischer Tropsch limitations and reactors

As mentioned previously, FT is a highly exothermic reaction and therefore efficient heat removal is one of the main considerations while designing commercial scale FT reactors [52]. Uncontrollable temperature gradients lead to the formation of local hotspots and in some cases, unstable temperature runways may occur (radial and axial gradients). This promotes the formation of methane and lowers the selectivity of the desired hydrocarbon products. The secondary impact is realized on the catalyst as it leads to irreversible damages like sintering, coking, phase changes, etc. that demands more maintenance cycles (downtimes). Other issues related to mass transfer limitations are also observed in FT processes. The pores of the catalyst are most likely to be filled with liquid hydrocarbons (wax) during the FT reaction. This imposes diffusion limitations on the reactants and products within the catalyst pores, resulting in lower reaction rates, lower conversions, higher chain termination, and thus a decrease in the chain length of the hydrocarbon products. This shifts the selectivity of the FT reaction toward lower weight hydrocarbons (undesired methane).

From the beginning of Fischer Tropsch chemistry discovery until today different reactor technologies have been proposed, with the aim of improving both capacity, efficiency and performance. The first type of reactors that were employed before and during world war II are fixed bed reactors with; internal cooling operation, Multitubular reactor bed, adiabatic fixed bed [53]. Later developments on the FT reactor technologies were employed with increased potential for large scale production of liquid fuels in the period after world war II [53]. This included improving the performance of existing fixed

bed reactor systems and the development of the slurry bed reactor, fluidized bed reactor and circulating fluid-bed reactor. The types of FT reactors are shown in Figure 8.

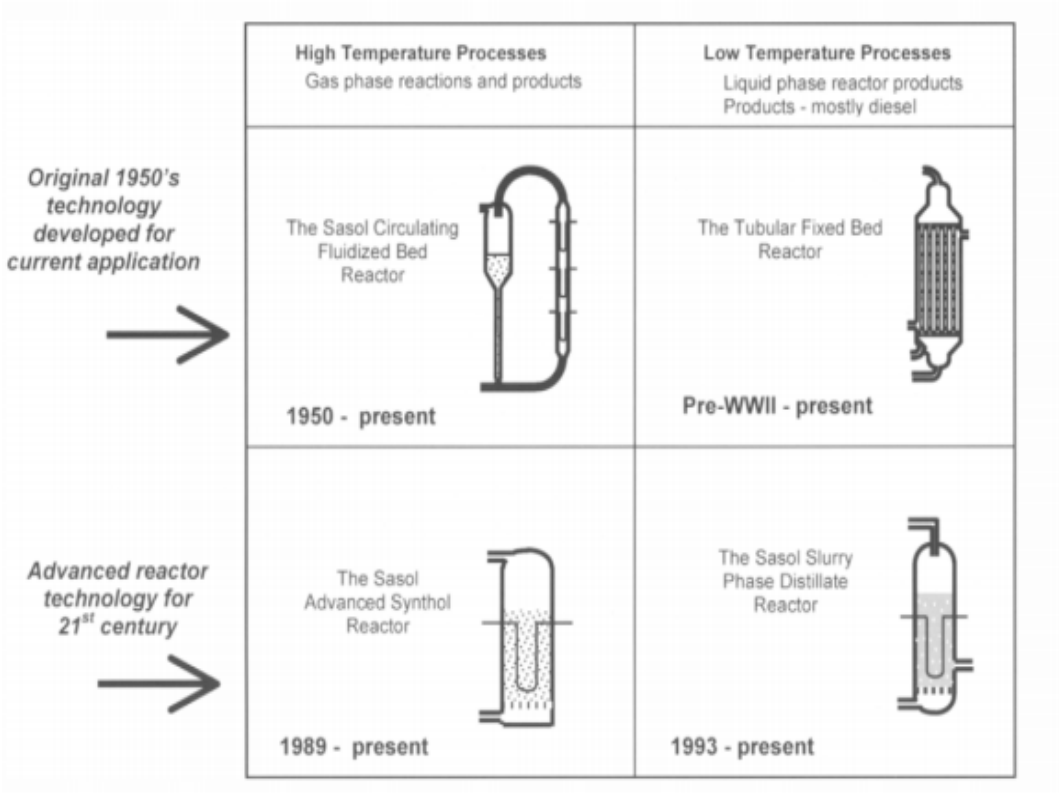

Figure 8: Types of FT reactor systems reprinted from [54].

Out of all the developed reactor technologies only three of have been commercialized including 1) Fluidized bed reactor (FB) both circulating and fixed, 2) Multi-tubular fixed bed (or packed bed reactor configuration (PB)), and 3) Slurry Bubble column reactor (SR). The three reactor bed configurations each have their own advantages

and drawbacks [55]. A comparison between the FT reactor configurations is summarized in Table 2.

Table 2: Comparison between the FT reactor systems reprinted from [56]

Feature	Fixed bed	Fluidized bed(circulating)	Slurry phase
Operation	simple	complex	intermediate
Temperature control	poor	good	good
Heat exchanger surface	$240m^2$ per $1000m^3$ feed	$15\text{-}30m^2$ per $2000m^3$ feed	$50m^2$ per $1000m^3$ feed
Max. reactor diameter	<80mm	large	large
Ch_4 formation	low	high	as fixed bed or lower
Flexibility	high	little	intermediate
Product	full range	low mol. Weight	full range
Space-time yield(C_{2+})	$>1000kg/m^3$ day	$4000\text{-}12000kg/m^3$ day	$1000kg/m^3$ day
Catalyst effectivity	lowest	highest	intermediate
Back mixing	little	intermediate	large
Minimum H_2/CO feed	as slurry or higher	highest	lowest
Construction			simplest

In a typical commercial-scale FT process, there are two modes of operation; High-Temperature Fischer Tropsch (HTFT) and Low-Temperature Fischer Tropsch (LTFT)[26]. The LTFT process is a three-phase process (gas-liquid-solid) and typically operates at temperatures ranging from 200 to 240 ^oC, and utilizes cobalt-based catalysts to produce heavy hydrocarbons such as Diesel and Wax [57, 58]. On the other hand, the HTFT process mainly involves (gas-solid) [35], which operates at temperatures from 320 to 350 ^oC, and utilizes a fused Iron based catalyst to produce lighter hydrocarbons such as olefins, oxygenates and gasoline [59]. FB reactors are categorized as HTFT, while SB reactors and PB reactors are categorized as LTFT. The main feature distinguishing between the LTFT and HTFT is that there is no liquid phase surrounding the catalyst

particles during operation[60]. The formation of liquid in HTFT fluidized bed reactors leads to agglomeration and hinders fluidization.

The hydrodynamics of FB reactors provide good temperature control (near isothermal operation) within the reactor bed. However, deposition of heavy wax on the catalyst may also cause the particles to agglomerate and thus obstruct fluidization [53]. To overcome the latter issue, fluidized bed reactors are operated at high temperatures typically 320 to 350 ^{o}C, to eliminate the presence of a liquid phase. However, operating at such high temperatures enhances the production of undesired methane. PB bed reactors have several advantages and are most often used as commercial FT reactors [35]. This is due to the simple operation, easy scale-up from a single tube to an industrial size multi-tubular reactor, and shutdown robustness of PB reactors compared to SB and FB reactors [10]. Also, the separation of the catalyst from the liquid product is not required. The liquid products in PB reactors simply trickle down through the reactor bed, and are separated from the exit gas using a knock out vessel [52]. This imposes significant reductions in the operational costs of the process. On the other hand, due to the pressure drop limitations in PB bed reactors, particles relatively larger than 1 mm are utilized. These requirements lead to mass transfer limitations that can negatively affect the product selectivity [61]. Therefore, to achieve high productivity within the reactor bed, very active catalysts need to be used, hence increasing the amount of heat released during the reaction. This would result in high temperature gradients within the reactor bed, and in some cases can lead to temperature runways due to the poor effective thermal conductivity of the PB reactors [53, 62]. For this reason, such type of reactors utilizes several hundred to around ten thousands

small diameter tubes (2 to 5 cm) to facilitate heat removal [35]. The short distance between the catalyst particles and the tube walls provides more efficient heat transfer from the catalytic bed to the cooling medium. Moreover, the operational temperature is typically low (210-225 ° C for a Co catalyst and 230-245 ° C for a Fe catalyst). For that reason, the single pass conversion is kept at 50% or lower to avoid temperature runways. Such type of limitations is not observed in SB reactors. These reactors operate like a Stirred Tank Reactor (STR) and utilize wax produced in situ in the process as a media for the reaction. This provides much better temperature control and uniformity due to elevated thermal capacity compared to the gas phase (GP), resulting in better product selectivity [33]. This allows the ability to operate at higher temperatures (230-250 ^{o}C) resulting in higher conversions compared to PB reactors [63]. The use of small catalyst particles around 100 μm minimizes the mass the transfer limitations and provides more efficient utilization of the catalyst active sites [64]. Another benefit is the reduction in compression costs as a result of significant reduction in pressure drop due to the extremely large hydraulic head of the SB reactor. Moreover, due to extremely low material costs, and state of art technology in the online catalyst removal process, the turnarounds and downtimes are reduced considerably. However, this technology poses several new challenges due to issues related to catalyst separation from liquid products, and much faster rates of catalyst attrition compared to PB reactor technology. Additionally, the catalyst particles in SB reactors are submerged in the liquid formed during the reaction and are therefore more susceptible to poisoning if the feedstock includes to sulfur. On the other hand, in PB

reactors the presence of sulfur in the feedstock, will affect only the top layers of the catalyst bed, and hence the reminder of the catalyst bed remains unaffected.

1.1.2.4. Opportunities for process intensification

The downsides of FT reactors discussed in the previous section can be solved or at least mitigated through process intensification. Process intensification aims at tackling issues in current FT technologies while maintaining its same economic viability. Various catalytic structures and reactor configurations have been proposed in the literature to overcome mass and heat transfer limitations associated with conventional FT reactors. Micro-structured reactors which consist of micrometer-sized tubes or channels are a promising alternative to conventional FT reactors [12, 64]. The small distance between the catalyst and the reactor wall in microstructured reactors provides good heat and mass transfer characteristics, which limits the formation of undesired methane. The ability of such reactor configurations to minimize heat transfer resistances allows the use of more active catalysts with much higher hydrocarbon productivities[13]. Another approach for process intensification during FT synthesis is the use of structured catalysts such as honeycomb catalysts. These catalysts are formed by coating a honeycomb monolith support with a thin layer of catalyst. In this type of reactors, the reactant mixture follows the Taylor flow regime, which provides high mass transfer coefficients combined with low-pressure drop [12]. The latter effect would result in small mass and heat transfer resistances. Moreover, studies on metallic monolith with wash-coated catalyst layers have shown to provide better thermal management, lower diffusional limitations and lower

pressure drops [65]. Moreover, High thermal conductivity catalytic structures consisting of microfibrous entrapped catalyst (MFEC) has been proposed [2] to facilitate heat removal from the reactor bed. Additionally, utilization of a hydrocarbon solvent, and running the reactor in near-critical and supercritical conditions (SCF-FT) of the solvent has also shown certain benefits in FT reaction. SCF solvent has demonstrated to have certain advantages in mitigating hot spot formation due to its unique characteristics including its liquid-like heat capacity and gas like diffusivity [66-68].

1.1.2.5. Introduction of a non-conventional supercritical reaction media

To overcome the limitations associated with PB reactors and the SB reactors, while combining the heat transfer benefits of SB reactors, and maintaining the ease of operation of PB reactor, operating FT under supercritical fluid (SCF) conditions was introduced [68, 69]. It has been suggested that the introduction of the supercritical solvent in the reaction media significantly changes both the transport and thermodynamic behaviour of the reactor bed [67, 69-74]. This phase manipulation is achieved by the introduction of a solvent while operating the reaction at the near-critical and supercritical condition to manipulate the physical properties of the reactor bed in such a way that its density and heat capacity behaves like liquid phase, while viscosity and diffusivity behave like that of gas phase[75]. Thus, the characteristics of SCF-FT reactor bed are generally supposed to be an intermediate between FT SB reactor and FT PB reactor. The primary advantages of such unique reactor technology is that it provides an opportunity to control both the heat

and the mass transfer limitations while facilitating an opportunity to control the hydrocarbon products distribution. In particular, the SCF-FT reactor bed facilitates:

1) In situ extraction of waxy hydrocarbons from catalyst pores due to improved solubility of reaction media [68, 76, 77].

2) Elimination of transport limitation promoting selectivity towards heavier hydrocarbons due to the low viscosity and high diffusivity of SCF fluids [77].

3) Desorption of primary products prior to undergoing secondary reactions resulting in a significant increase in α-olefin selectivity [76, 78-80].

Yan et al. reported that under identical temperature and pressure conditions and residence time (Co/SiO_2, T = 210 °C, P_{tot}= 4.5 MPa), higher CO conversion were achieved using SCF media (pentane) (84%) compared to GP operation (70%) [81]. Similar findings were reported by Irankhah and Haghtalab ($Co–Re/Al_2O_3$, T= 240 °C, P_{tot}= 5.5 MPa), where the conversion levels were 63% and 54% under SCF and GP conditions respectively. [82]. This suggests that utilizing SCF provides could improve the activity of the catalyst. Moreover, Yokota and Fujimoto conducted an experimental study using Co-SiO_2 catalyst at (T=240 °C, P_{tot} = 4.5 MPa). They reported that hydrocarbon cuts (C_{26}) were produced when operating in the liquid phase while operating using SCF (hexane), the carbon number went up to (C_{40}) [83]. This finding suggests that using SCF as a reaction media shifts the overall product distribution towards heavier weight hydrocarbon products. Mover, experimental investigations were conducted to study the role of SCF in improving the heat transfer characteristics in PB reactors. Studies conducted by Yokota

and Fujimoto have shown that the maximum temperature rise at 60% CO conversion for three reaction medias using Co–La/SiO_2 catalyst at (T= 240 °C, Ptot= 4.5 MPa) are as follows: liquid phase (10 °C), supercritical phase (13 °C), gas phase (18 °C)[83]. Huang and Roberts [16] also studied the temperature profiles under steady-state conditions along a fixed bed reactor operating using SCF media over Co–Pt/Al_2O_3 catalyst at (T= 250 °C, P_{tot}= 8 MPa) and GP media (T= 250 °C, P_{syngas}=2 MPa). They found that the maximum temperature deviation along the length of the reactor was approximately 5 °C under SCF operation and 15 °C under GP operation [80].

1.1.2.6. Utilizing a novel microfibrous Entrapped cobalt based catalytic structures

The microfibrous Entrapped cobalt based catalytic structures MFECC is produced by entrapping small cobalt particles in a porous metal sheet (copper) of interlocking microfibers [84]. The high thermal conductivity of this catalytic matrix provides significant improvement in temperature control compared to conventional PB reactors. This provides a longer catalyst lifetime and selectivity to desired longer chain hydrocarbon products. The improved heat characteristics provided using MFECC structures allows the use of smaller catalyst particles with diameters ranging from (10 to 100) μm to eliminate mass and heat transport resistances. This provides better utilization of the catalyst and thus higher productivity is achieved. Moreover. MFECC provides high void fraction which significantly reduces pressure drops compared to conventional PB reactors. Sheng et al conducted an experimental study to calculate the thermal parameters of MFECC structures compared to PB reactors (effective radial thermal conductivity and wall heat transfer

coefficient)[85]. They found that the effective radial thermal conductivity of MFECC was 56 times higher than that of PB diluted with fresh alumina, while the wall heat transfer coefficient was 10 times higher than that of the alumina PB. Another study was done by Kalluri et al to investigate the effect of the bed void on the transport resistances for MFEC structures and diluted PB [86]. They found that the dilution of the PB only improved radial dispersion to a small extent, However MFEC structures promoted radial dispersion which in turn led to more uniform radial concentration profiles and reduced flow disturbances, which was due to the high bed void of MFEC structures.

1.1.2.7. Modeling Fischer Tropsch reactor systems

It is essential to study the performance of conventional and non-conventional FT technologies under a wide range of operational conditions, especially in industrial size reactors or so-called large-scale reactors [64]. The latter being the most important to investigate the potential and feasibility of novel reactor technologies in industrial applications. This requires considering the high level of details to study the interplay between momentum, heat and mass phenomena [87]. Computational fluid dynamic (CFD) modeling is a tool with high potential to accurately describe the fluid hydrodynamics inside FT reactors. The formulation of reliable mathematical models for fixed-bed FT systems requires considering the high level of details the phenomena occurring in FT processes including; momentum transfer, heat, and mass diffusional resistances, heat and mass convection transport in the fluid phase, heat conduction between the fluid phase and the solid phase, pressure drop and chemical reactions. Also, considering the high

dependency of the Fischer Tropsch reaction rate and product selectively on the reactor operating conditions and thermal parameters using reliable kinetic models which capture the complexity of the FT reaction mechanism/pathway is of high importance. Solving a generalized mathematical model for reactor systems which couples all reaction kinetics and the transport phenomena (heat, mass, momentum) occurring between the different phases in the reactor bed is computationally very complex. Therefore, mathematical models are generally developed based on simplified correlations and assumptions that would result in less complex numerical solutions, but still, include a sufficient representation of the essential phenomena/mechanisms involved.

In the literature, various studies have been dedicated towards model development of PB reactors, in which the primary objective was to enable understanding of reactor performance under a set of operational conditions not easily achievable on an experimental scale. Majority of these models were developed under the assumption of Pseudo-homogeneous phase to evaluate axial profiles of temperature, product distribution and pressure drop profiles [64, 88-95], with some being more advanced to include diffusional limitations for particle scale assessment of the reactor profile [35, 55, 61, 96-98].

In 1979, Atwood and Bennett developed the first mathematical model for a fixed bed reactor using a simple kinetic model for an Iron based catalyst. The developed model was one-dimensional plug flow and the bulk heat and mass transfer resistances were considered by calculating the wall heat transfer coefficient at the wall [28]. They studied the effect of Reynolds numbers and tube diameter on the reactor temperature at a fixed conversion.

In 1980, Bub and Baerns proposed a two-dimensional pseudo-homogenous model for a fixed bed reactor using an empirical kinetic model for an Iron-based catalyst [99]. The intraparticle diffusion limitations were neglected. They studied the effect of the reaction conditions on the product selectivity.

In 1999, Jess and Hedden developed a two-dimensional pseudo-homogenous model for a single-tube in a Multitubular reactor bed. However, they considered the radial dispersion in the heat balance equations. The main objective of their work was to study the effect of nitrogen on the thermal performance of the reactor bed.

In 2003, Wang et al developed a one-dimensional heterogeneous model for a fixed bed reactor. They incorporated a detailed mechanistic model for an Iron-based catalyst and accounted for intraparticle diffusion limitations. The model was used to investigate the effect of tube diameter on the selectivity of C_{5+} hydrocarbons and to study the effect of recycling on the thermal performance of the reactor bed[100].

In 2005, Marvest et al presented a two-dimensional fixed bed reactor model for an Iron bifunctional catalyst. They studied the effect of the cooling temperature, H_2/CO ratio, and tube diameter on the performance of the reactor bed[101].

In 2009, Jess and Kern developed a two-dimensional pseudo-homogeneous model for a Multitubular fixed bed reactor, using simple kinetics for iron and cobalt catalysts. The intraparticle diffusion limitations and radial heat transfer effects were considered. They provided a comparison to study the effects of the reaction conditions on the performance of the reactor bed for booth iron and cobalt catalysts [102].

In 2011, Sharma et al proposed a 2-dimensional pseudo-homogeneous fixed bed reactor model. The intraparticle diffusion resistances were neglected. They employed a simple rate law to study the effect of the reactor operating conditions on CO conversion and product selectively for various catalyst structures [103].

In 2012, Brunner et al proposed a one-dimensional pseudo-homogeneous fixed bed reactor model for applicable to both cobalt and iron catalysts. A simple kinetic rate expression was used. They accounted for the heat transfer resistances by calculating and incorporating the radial thermal conductivity. The model was sued to investigate the effect of the effective diffusivity, Prandtl number and friction factor on the reactor performance parameters [104].

In 2013, Mamonov et al developed a one-dimensional heterogeneous model for a fixed bed reactor. They considered the diffusional limitations and heat transfer resistances. The model was used to study the effect of gas velocity and tube diameter on the thermal stability of the reactor bed [91].

In 2014, Kaiser and Jess modeled a two-dimensional pseudo-homogeneous Multitubular fixed bed reactor for both Iron and cobalt. The mass transfer limitations were considered. The model was used to optimize the parameters (tube diameter, superficial velocity, cooling temperature, and H_2/CO ratio0 that would result in better catalyst performance [105].

In 2015, Mozza et al proposed a pseudo-homogeneous one-dimensional mathematical model over a cobalt-based catalyst. The effect of used Nitrogen-rich syngas was

investigated. Also, the performance of the reactor was studied at different operating conditions (temperature, pressure, gas velocity) [106].

In 2016, Ghouri et al presented a one-dimensional pseudo-homogeneous model for a fixed bed reactor, in which a detailed kinetic model for a cobalt catalyst was used. The mass diffusion resistances were calculated to obtain temperature and concertation profiles and concentration inside the catalyst particle [93].

In 2017, Stamenic et al proposed a one-dimensional heterogeneous model for a fixed bed reactor. The mass transfer limitations were considered and a detailed kinetic model for a cobalt catalyst was employed. The model was used to study the effects of process conditions on CO conversion and hydrocarbon selectively (Methane and C_{5+}) [55].

In 2018, Chaliwalla et al developed a two-dimensional model for a fixed bed reactor model using conventional cobalt catalyst and a novel Microfibrous Entrapped cobalt based catalytic structure. A simple kinetic model was used and the intraparticle diffusion limitations were neglected. The model was used to investigate the thermal performance of the conventional and non-conventional reactor systems at larger tube diameter [84].

This work aims at extending the modeling efforts that have been done to model FT reactor systems. The scope of this work will mainly focus on modeling non-conventional FT systems and provide a comparison with a conventional FT system (Multitubular/PB reactor model) in terms of thermal performance. More details will be presented in the following sections.

2. RESEARCH MOTIVATION AND OBJECTIVES

The GTL process will remain as an attractive pathway toward the production of clean value-added chemicals and liquid hydrocarbons through Fischer Tropsch synthesis. To conduct the FT process, three reactor technologies are commercially employed; fluidized bed reactor 2) Multi-tubular fixed bed 3) Slurry Bubble column reactor. Each of these reactors exhibits its own advantages and drawbacks. However, Multitubular fixed bed/PB reactors have gained more interest from the research and industrial community, since they provide higher reaction rates, resulting in higher volumetric productivity. However, the high exothermicity of the FT process and the poor thermal conductivity of PB reactors limits its scalability to higher tube diameters (>5 cm). Using large tube diameters would result in local overheating of the catalytic particles, which shifts the product selectivity towards lower hydrocarbon cuts mainly methane. Over the years, advanced technologies have been applied to the PB reactors to overcome the limitations/shortcomings associated with them. Out of these is the employment of a unique reaction media SCF with gas-like transport properties and liquid-like heat capacity and solubility characteristics. Utilizing SCF as a reaction media provides better heat management, longer catalyst lifetimes, and selectivity control of the hydrocarbon product distribution. Also, using metal catalytic structures (MFECC), with enhanced heat transfer properties in the FT process, has proven to aid in eliminating hotpots that typically occur in PB reactors. However, the implementation of the aforementioned technologies is still at the laboratory scale. There are several aspects that need to be addressed before the commercialization of non-

conventional FT technologies. Most importantly is the scale-up to industrial size reactors to study the hydrodynamics and reactor performance under conditions used in industry and cannot be experimentally achieved. This can be done by applying CFD models to represent the fluid behavior inside the reactor.

The motivation of this work is to closely understand the improved heat transfer characteristics achieved in PB reactors upon the utilization of non-conventional SCF reaction media and a novel MFECC catalyst through CFD modeling. There are several factors which complicate the modeling of PB reactors including; 1) the variation of parameters with the spatial domain, 2) nonlinear dependence of the reaction rate on temperature and pressure, 3) a large number of species produced during the reaction, and 4) the different phases involved in the reaction (gas-liquid-solid) [107]. Therefore, in this work, 2-dimensional transport correlations for mass, heat, and momentum are coupled with reliable kinetic models to accurately predict the temperature distribution and conversion levels within the reactor bed.

The main goals of this thesis will be achieved by completing the following tasks:

1. Develop a generalized 2-dimensional pseudo-homogenous model in COMSOL® Multiphysics, capable of predicting the performance and the dynamic behavior of FT reactors under a wide range of operational conditions for three systems (SCF-FT, MFECC-GP-FT, and PB-FT).

2. Utilize a detailed kinetic model developed by (Todic et al. [38]) to predict the methane selectivity and C_{5+} hydrocarbon selectivity in MFECC-GP-FT and PB-FT.
3. Demonstrate the ability of SCF-FT and MFECC-GP-FT in mitigating hotspot formation and the challenges associated with temperature control in the GP-FT reactor bed.
4. Use the base case scenarios to study the effect of the gas hourly space velocity (GHSV) on the radial temperature and CO conversion.
5. Study the effect of scaling up the reactor tube diameter from the base case scenario to a 4-inch diameter on the thermal behavior, CO conversion, and hydrocarbon productivity.

3. RESEARCH METHODOLOGY

Guidelines on modeling fixed bed reactor systems have been extensively documented in the literature [1-3]. These were carefully followed to develop a reliable model that could be applicable under a wider range of operating conditions. The fixed-bed reactor was assembled in 2-D axisymmetric space via COMSOL Multiphysics v5.3 using the finite.The model geometry comprised of three zones pertaining to pre-packing, catalytic bed, and post-packing respectively as shown in Figure 9. The model was developed for three FT systems; non-conventional MFECC bed under GP-FT conditions, conventional PB under GP-FT conditions and non-conventional PB in SCF media. For model validation purposes, the reactor dimensions in the CFD model were specified based on the geometry of the reactor used to conduct the FT experiments. 2-D correlations were used in this modeling study for momentum, heat and mass transfer to account for the variation of concentration and temperature in the radial and axial directions. This is because, for larger tube diameters (scaling-up) [4], higher radial temperature gradients are expected. Since the main goal of this modeling work is to study the effect of heat generation on the reactor bed performance including conversion and hydrocarbon product selectivity at larger tube diameters (up to 0.1016 m), 2D modeling approach was chosen [5].

The fixed bed reactor developed in this work was modeled as a pseudo-homogeneous model. This assumption indicates that the interfacial mass and heat resistances occurring between the solid phase and the fluid phase are neglected (the

catalyst surface is exposed to bulk fluid conditions). This implies that the catalyst effectiveness factor (the ratio of the overall reaction rate in the pellet to the surface reaction rate for a specific component) is equal to 1.

The fluid flow, in this case, was assumed to be a single-phase flow, however, the presence of the liquid was considered by calculating the liquid physical properties (heat capacity, thermal conductivity, viscosity, diffusivity, density permeability) of the hydrocarbon cuts which exist in the liquid and gas phase.

Modeling and simulation of the FT reactor bed require a simultaneous solution of momentum, mass, and heat balance equations in the three domains specified earlier; pre-packing, catalytic bed, and post-packing. The entire operation is considered to be at steady state. The reactants CO and H_2 enter the reactor to the pre-packing zone and exit the reactor from the post-packing region which is inert non-catalytic regions. It is assumed that the reaction only takes place in the catalytic bed region over 15% Co/Al_2O_3 catalyst particles of identical sphericity ($\emptyset$=1). The model bed was built to represent the reactor system used in the experimental setup, for model validation purposes. For the GP-FT reaction, 160 μm particle diameter was used representing the diluted catalyst bed of average particle size 149–177 μm as reported by Sheng et al [6]. The solid matrix for the MFECC reactor bed consisted of copper metal fibers, loaded with a catalyst (7.4vol% copper fibers, 62.6vol% void and 30vol% (15% Co/Al_2O_3)). The PB under GP operation was diluted to the same catalyst density as the MFECC bed with fresh alumina (30vol% (15% Co/Al_2O_3), 36vol% void and 34vol% Al_2O_3). For the PB under SCF operation, the particle size of 200 μm diameter was used representing the catalyst bed diluted with silica quartz (SiO_2) (10%

(15% Co/Al_2O_3), 35.25% voids, 44.2% SiO_2). Additional assumptions and more details are stated in particular parts of the model development section. Solutions were obtained by using the Direct MUMPS solver (MUltifrontal Massively Parallel sparse direct Solver) on a Dell Server R820 with 2x4 Intel® Xeon® E5-4650 @ 2.70 GHz octa-core. An extremely fine mesh was used and the solution time was typically around 30mins.

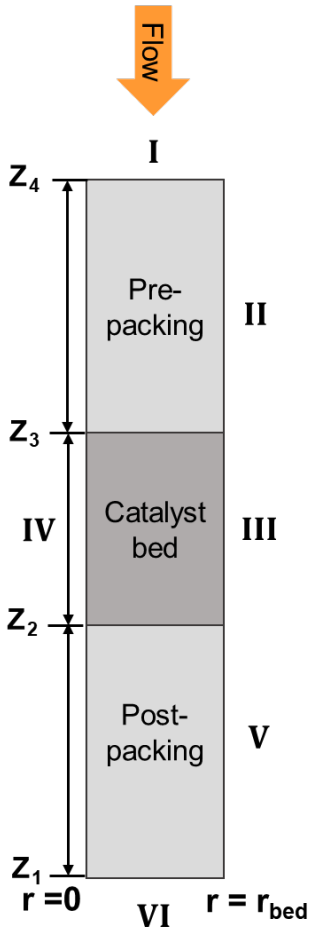

Figure 9: Axisymmetric cut section of the 2D FT reactor bed model cylindrical geometry

3.1. Model development under GP-FT conditions (PB and MFECC reactor beds)

3.1.1. Momentum transport expressions

In order to model fluid flow in porous media and the free flow domains, a built-in module in COMSOL® Multiphysics called “Brinkman Equation” was adopted (Eq 9). The Brinkman physics is used to compute the fluid velocity and pressure field in single-phase flow in porous media in the laminar flow regime. This mathematical model extends Darcy’s law to account for dissipation in kinetic energy due to shear stress, similar to Naiver stokes equation [108]. This physics comprises of two main terms; the Forchheimer drag term and the convective term. The convective terms take into account the effect of inertial and viscous forces on the fluid flow through the porous medium. The Forchheimer drag term accounts for the inertial drag effects that occur in fast flows (Reynold number (Re) greater than unity) [109]. Considering slow flow regimes where Re is less than unity, the Forchheimer drag contributions are neglected. The 2D single-phase fluid flow through the PB is described in terms of the velocity (**u)** and pressure fields (**p**), which are computed via solving the momentum equation and continuity equation (Eq 10) simultaneously. The changes in volumetric gas flow rates of the reacting species during the FT reaction results in variations in the fluid density, therefore a compressible flow formulation of the continuity equation is used. When a compressible flow is modelled using the Brinkman equation, the Mach number must be below 0.3. This condition is fulfilled in this case study.

$$\frac{1}{\epsilon_{\text{bed}}}\rho_f(\mathbf{u}.\boldsymbol{\nabla})\mathbf{u}\frac{1}{\epsilon_{\text{bed}}} = \boldsymbol{\nabla}\cdot\left[-\text{p}\mathbf{I} + \mu_\text{f}\frac{1}{\epsilon_{\text{bed}}}(\boldsymbol{\nabla}\mathbf{u} + (\boldsymbol{\nabla}\mathbf{u})^\text{T}) - \frac{2}{3}\mu_\text{f}\frac{1}{\epsilon_{\text{bed}}}(\boldsymbol{\nabla}\cdot\mathbf{u})\mathbf{I}\right] - \left(\frac{\mu_\text{f}}{\kappa_{\text{bed}}} + \beta_f|\mathbf{u}|\right)\mathbf{u} \quad (9)$$

$$\boldsymbol{\nabla}(\rho_f\mathbf{u}) = 0 \quad (10)$$

where, μ_f is the dynamic viscosity of the fluid, ϵ_{bed} is the porosity, ρ_f is the density of the fluid, κ_{bed} is the permeability of the porous medium and β_f is the Forchheimer drag coefficient.

The porosity of the MFECC fixed-bed was chosen as 0.626 while 0.36 was chosen for the PB per the catalyst specifications reported by Sheng et al [85, 110]. The bed void fraction is assumed to be constant throughout the entire catalyst bed.

The permeability of the porous medium was calculated using the modified Ergun equation[111]:

$$\frac{1}{\kappa_{\text{bed}}} = \frac{150(1-\epsilon_{\text{bed}})^2}{d_p^2{\epsilon_{\text{bed}}}^2} + \frac{1.75\rho_f\mathbf{u}(1-\epsilon_{\text{bed}})}{d_p\mu_\text{f}{\epsilon_{\text{bed}}}^3} \quad (11)$$

where d_p is the particle diameter.

3.1.2. Mass transport expressions

Mass conservation equations for the pseudo homogenous reaction (assuming catalyst effectiveness as unity) is defined for each component of the reaction mixture pertaining to the following FT reactions

$$nCO + (2n + 1)H_2 \rightarrow C_nH_{(2n+2)} + nH_2O \quad \text{(Synthesis of paraffin)} \tag{12}$$

$$nCO + 2nH_2 \rightarrow C_nH_{2n} + nH_2O \quad \text{(Synthesis of olefins)} \tag{13}$$

Components considered in the system are N_2, CO, H_2, H_2O, CH4, CH_o and CH_p. N_2 was set as the mass constraint component since it's a non-reacting species. The hydrocarbon components CH_o and CH_p are a summation of olefins and paraffin products respectively for C_1,C_2,C_3…C_{15} components. The C_{15}-C_{22} hydrocarbons are lumped into one component represented by a paraffinic compound $C_{19}H_{40}$, while the higher weight hydrocarbons C_{22+} are represented by the paraffinic component $C_{22}H_{40}$. It is important to note that this study considers a cobalt-based catalyst where the rate of water-gas shift reaction is assumed to be negligible. Therefore, selectivity calculations of CO_2 have not been considered in this modeling study.

The local mass balance for species i (N_2, CO, H_2, H_2O, CH4, CH_o and CH_p) was described by (Eq 14) using a built-in physics module "Transport of concentrated species" which accounts for mass transport through convection and diffusion in the axial and radial directions The equation provided in COMSOL® Multiphysics for transport mechanism is as follows:

$$\nabla j_i + \rho_f(\mathbf{u} \cdot \nabla)w_i = R_i \tag{14}$$

Where w_i is the mass fraction of species i, j_i is the mass flux relative to the mass averaged velocity of species i, R_i is the reaction rate representing production or consumption of species i.

The diffusion model selected in this case was the Maxwell Stefan diffusion model, where the relative mass flux vector is calculated using X.

$$j_i = -\rho_f w_i \sum D_{ik} d_k \tag{15}$$

where D_{ik} represents the binary diffusivity, d_k is the diffusional driving force acting on species k defined as follows:

$$d_k = \nabla x_k + \frac{1}{p}[(x_k - w_k)\nabla p] \tag{16}$$

The mole fraction x_k is given by:

$$x_k = \frac{w_k}{MW_k} MW_n \tag{17}$$

The mean molar mass MW_n is defined as:

$$\frac{1}{MW_n} = (\sum(\frac{w_i}{MW_i})^{-1} \tag{18}$$

The binary diffusivities D_{ik} for the Maxwell Stefan diffusion model are estimated using Fickian diffusivities with an empirical correlation proposed by Fuller et al [112].

$$D_{ik} = \frac{\sqrt{\frac{1}{MW_i} + \frac{1}{MW_k}}}{p(v_{c,i}^{\frac{1}{3}} + v_{c,k}^{\frac{1}{3}})^2} \times 10^{-7} \tag{19}$$

where, MW_n represents the mean molar mass and v_c represents the molar volume for species i and k. The molar volume of the representative paraffin and olefin components

CH_o and CH_p respectively are calculated as a molar weight average sum using the molar volumes of the individual hydrocarbon species based on the ASF product distribution, whereas the molar volumes of H_2O, CO H_2 , N_2 and CH_4 used in this model are: 12.7,18.9, 7.07 , 17.9 and 37.9 $\frac{cm^3}{mol}$ respectively.

3.1.3. Heat transport expressions

Energy balance within the 2-D reactor domain was considered to account for the transport of heat through convection, conduction, and thermal dispersion. Radiative heat transport was neglected in this case. Balance equations were solved using the simplified "Heat transfer in porous media physics" (Eq 20):

$$\rho_f C_p \mathbf{u}.\nabla T - \nabla(q) = Q \tag{20}$$

$$q = -k_{eff}\nabla T \tag{21}$$

$$Q = (-\Delta H_{rxn})R_{CO} \tag{22}$$

Where q is the conductive heat flux, T is the temperature inside the reactor bed, k_{eff} is the effective thermal conductivity, Q is the heat source or sink, R_{CO} is the rate of consumption of carbon monoxide and ΔH_{rxn} is the heat of the reaction per mole of CO consumed.

The reaction enthalpy $(-\Delta H_{rxn})$ is an important parameter that determines the amount of heat released during the FT reaction. Previous modeling studies reported values of $(-\Delta H_{rxn})$ ranging from 150 to 165 kJ/mol of CO consumed to represent the FT reaction enthalpy [35, 64, 84, 93, 110]. Its value mainly depends on the hydrocarbon product selectivity. The $-\Delta H_{rxn}$ value used in this study was between 152-160 kJ/mol of CO.

The effective thermal conductivity of the bed was calculated using a volume-based average model to account for both the solid matrix and the fluid properties

$$k_{eff} = \epsilon_{bed} k_s + (1 - \epsilon_{bed}) k_f \quad (23)$$

Where k_s is the solid thermal conductivity and k_f is the fluid thermal conductivity

The solid phase thermal conductivity k_s was found using the volume-average of the thermal conductivities of the inert packing and the catalyst as per reactor packing specifications reported by Sheng et al [85, 110].

$$k_s = \theta_s(\theta_{cat} k_{cat} + \theta_{inert\_material} k_{inert\_material}) \quad (24)$$

Where θ_s the volume fraction of the bed occupied by the solid phase defined as $(1 - \epsilon_{bed})$, θ_{cat} is the volume fraction of the catalyst, $\theta_{inert\_material}$ is the volume fraction of the inert packing (PB) or Metal copper fibers (MFECC) fixed-bed.

The heat capacity within the reactor bed was defined in a similar manner to the effective thermal conductivity of the bed

$$\mathrm{C}_p = \epsilon_{bed} \mathrm{C}_{p_s} + (1 - \epsilon_{bed}) \mathrm{C}_{p_f} \quad (25)$$

$$\mathrm{C}_{p_s} = \theta_s(\theta_{cat} \mathrm{C}_{p_{cat}} + \theta_{inert\_material} \mathrm{C}_{p_{inert\_material}}) \quad (26)$$

3.1.4. Kinetics

The rate of CO disappearance is calculated using the Yates and Satterfield (YS) kinetic model, which has been commonly used to previous modeling studies [35, 55, 61, 97, 113-115]:

$$-R_{CO}{}^{\mathrm{YS}} = \frac{k.P_{H_2}P_{CO}}{(1+a.P_{CO})^2} \quad (27)$$

$$k = \mathrm{A_k} \exp\left(-\frac{\mathrm{E_k}}{\mathrm{RT}}\right) \quad (28)$$

$$a = \mathrm{A_a} \exp\left(-\frac{\mathrm{E}_a}{\mathrm{RT}}\right) \quad (29)$$

where P_{CO}, and P_{H_2} are the partial pressures of CO and H_2, k and a are the kinetic rate constants, A_k and A_a are the pre-exponential factors and $\mathrm{E_k}$ and E_a are the activation energies for CO consumption.

Numerical values of the kinetic parameters (Eq 27) by Stamenic et al where they estimated the kinetic parameters using experimental data with 0.48%Re 25%Co/Al_2O_3 catalyst, which is summarized in Table 3 [55, 61]. This catalyst is more active than the catalyst used by Yates and Satterfield, thus is more representative of Co catalysts used in industrial applications nowadays [61].

Table 3: Values of the parameters of YS model

Model	Parameter	Value	Unit
YS	$\log(A_k)$	8.18	$mol/g_{cat}/h/MPa^2$
	E_k	72.69	kJ/mol
	$\log(A_a)$	-0.19	1/MPa
	E_a	-10.77	kJ/mol

The product selectivity for CH_4 and C_{2+} hydrocarbons is calculated using Ma et al kinetics [116] and a detailed kinetic model of Todic et al, respectively [38]. The Ma kinetic model for CH_4 formation was proven to provide a good prediction of CH_4 selectivity [55], while the detailed kinetic model developed based on the carbide mechanism showed a good prediction of the hydrocarbon product distribution [38].

The rate of formation of CH_4 by the following expression [116]:

$$R_{CH_4}{}^{Ma} = \frac{k_M {P_{CO}}^{a_M} {P_{H_2}}^{b_M}}{1+m_M \frac{P_{H_2O}}{P_{H_2}}} \tag{30}$$

$$k_M = A_M \exp\left(-\frac{E_M}{RT}\right) \tag{31}$$

where k_M is the rate constant, m_M is the water effect coefficient, a_M is the reaction order of CO, b_M is the reaction order of H_2, A_M is the pre-exponential factor and E_M is the activation energy for CH_4 formation.

An important feature of (Eq 30) is that it predicts an increase of the CH_4 formation with temperature, the partial pressure of H_2 and H_2/CO ratio and it captures the inhibiting effect of water. Studies show that the inhibiting effect of water on CH_4 selectivity is well established in the literature [112, 117-120].

The rate of formation of the C_{2+} hydrocarbons from the detailed kinetic model by Todic et al [38] is given as follows:

$$R_{C_2H_4}^{\text{Prod}} = k_{6E,0}\, e^{2c} \sqrt{K_7 P_{H_2}}\, \alpha_1 \alpha_2 [S] \tag{32}$$

$$R_{C_nH_{2n+2}}^{\text{Prod}} = k_5 {K_7}^{0.5} {P_{H_2}}^{1.5} \alpha_1 \alpha_2 \prod_{i=3}^{n} \alpha_i \, [S] \quad n \geq 2 \tag{33}$$

$$R_{C_nH_{2n}}^{\text{Prod}} = k_{6,0}\, e^{cn} \sqrt{K_7 P_{H_2}}\, \alpha_1 \alpha_2 \prod_{i=3}^{n} \alpha_i \, [S] \quad n \geq 3 \tag{34}$$

where the k's represent the kinetic rate constants, K's represent the equilibrium constants, α_n are the chain growth probabilities and $[S]$ is the fraction of vacant sites.

The chain growth probabilities dependant on the carbon number are calculated using the following expressions:

$$\alpha_1 = \frac{k_1 P_{co}}{k_{5m} P_{H_2} + k_1 P_{co}} \tag{35}$$

$$\alpha_2 = \frac{k_1 P_{co}}{k_5 P_{H_2} + k_{6,0}\, e^{2c} + k_1 P_{co}} \tag{36}$$

$$\alpha_n = \frac{k_1 P_{co}}{k_5 P_{H_2} + k_{6,0}\, e^{cn} + k_1 P_{co}} \quad n > 2 \tag{37}$$

The fraction of vacant sites is calculated as following

$$[S] = 1/\left\{1 + \sqrt{K_7 P_{H_2}} + \sqrt{K_7 P_{H_2}}\left(1 + \frac{1}{K_4} + \frac{1}{P_{H_2} K_3 K_4} + \frac{1}{K_2 K_3 K_4}\frac{P_{H_2O}}{P_{H_2}}\right)(\alpha_1 + \alpha_1\alpha_2 + \alpha_1\alpha_2 \sum_{i=3}^{n} \prod_{j=3}^{i} \alpha_j\right\} \quad (38)$$

The kinetic parameters in detailed kinetic model and the Ma kinetic model were estimated by Todic et al and Stamenic et al [38, 55] using experimental data with 0.48%Re 25% Co/Al_2O_3 catalyst and are summarized in Tables 4 and 5.

Table 4: Values of the parameters of Ma et al model

Model	Parameter	Value	Unit
Ma et al	$\log(A_M)$	12.20	$mol/g_{cat}/h/MPa^{aM+bM}$
	E_M	139.98	kJ/mol
	a_M	-0.99	-
	b_M	1.28	-
	m_M	0.58	-

Table 5: Values of the parameters of the detailed kinetic model

Parameter	Value	Unit	Parameter	Value	Unit
$\mathbf{A_1}$	1.83E10	mol/g_{cat}/h/MPa	A_6	7.47E8	mol/g_{cat}/h
$\mathbf{E_1}$	100.4	kJ/mol	E_6^0	97.2	kJ/mol
$\mathbf{A_2}$	5.08	-	A_7	1E-03	MPa^{-1}
$\mathbf{\Delta H_2}$	8.68	kJ/mol	ΔH_7	-25.0	kJ/mol
$\mathbf{A_3}$	2.44	MPa^{-1}	A_{5M}	8.43E5	mol/g_{cat}/h/MPa
$\mathbf{\Delta H_3}$	9.44	kJ/mol	E_{5M}	63	kJ/mol
$\mathbf{A_4}$	2.90	-	A_{6E}	7.03E8	mol/g_{cat}/h
$\mathbf{\Delta H_2}$	7.90	kJ/mol	E_{6E}^0	108.8	kJ/mol
$\mathbf{A_5}$	4.49E5	mol/g_{cat}/h/MPa	ΔE	1.12	kJ/mol/CH_2
$\mathbf{E_5}$	72.4	kJ/mol			

In this work, a hybrid kinetic model adopted from Stamenic et al [55] and Bukur et al [97] was used in defining the reaction rates for CO, H_2, H_2O, CH_p (n-paraffin) and CH_o (1-olefins). This was done by coupling the YS kinetics for CO consumption, Ma et al kinetics for CH_4 formation and the detailed kinetic model of Todic et al for C_{2+} hydrocarbon formation. A normalization procedure was used to attain atomic closures due to the different approaches used to derive the kinetic models adopted in this modeling study. This was done as following:

The rate of consumption of CO excluding methane from the detailed kinetic model (rate of C_{2+} formation from Todic et al model) can be calculated based on the reaction stoichiometry as:

$$(-R_{CO})_{C_{2+}}^{Prod} = \sum_{n=2}^{n} n(R_{C_nH_{2n+2}}{}^{\text{Prod}} + R_{C_nH_{2n}}{}^{\text{Prod}}) \quad (39)$$

The rate of CO consumption excluding methane from the YS model (rate of C_{2+} formation from YS model) is calculated as:

$$(-R_{CO})_{C_{2+}}^{YS} = \left(-R_{CO}{}^{\text{YS}}\right) - (R_{CH_4}{}^{Ma}) \quad (40)$$

The normalized rates of formation of C_{2+} hydrocarbons are obtained as follows:

$$R_{C_nH_{2n+2}} = R_{C_nH_{2n+2}}{}^{\text{Prod}} \times \frac{(-R_{CO})_{C_{2+}}^{Prod}}{(-R_{CO})_{C_{2+}}^{YS}} \quad n \geq 2 \quad (41)$$

$$R_{C_nH_{2n}} = R_{C_nH_{2n}}{}^{\text{Prod}} \times \frac{(-R_{CO})_{C_{2+}}^{Prod}}{(-R_{CO})_{C_{2+}}^{YS}} \quad n \geq 3 \quad (42)$$

From the stoichiometry, the H_2 formation rate is calculated using the individual product formation rates of the hydrocarbon species as:

$$-R_{H_2} = 3R_{CH_4}{}^{Ma} + \sum_{n=2}^{n}[(2n+1)R_{C_nH_{2n+2}} + 2nR_{C_nH_{2n}}] \quad (43)$$

The rate of H_2O formation is equal to the rate of CO consumption based on the reaction stoichiometry:

$$R_{H_{2O}} = -R_{CO}{}^{YS} \quad (44)$$

3.1.5. Physical properties

3.1.5.1. Physical properties of the reacting species (Fluid domain)

The physical properties for the gaseous species (CO, H_2, N_2, H_2O, hydrocarbons C1-C8), and the liquid species and heavy waxes (hydrocarbons C_9-C_{22+}), corresponding to 1-olefins and n-paraffin involved in the system are calculated using correlations from different databases on Knovel. The physical properties of the fluid mixture are calculated at each nodal point in the reactor system as a function of the local temperature and composition.

The pure component molar heat capacity for gaseous species is calculated using a seven-parameter equation as a function of the fluid temperature:

$$Cp_i = A + BT + CT^2 + CT^3 + CT^4 + CT^5 + CT^6 \quad (\frac{J}{mol.K}) \quad (45)$$

The molar heat capacity of the liquid components and heavy waxes:

$$Cp_i = A + BT + CT^2 + CT^3 + CT^4 \quad (\frac{J}{mol.K}) \quad (46)$$

The fluid mixture heat capacity was calculated using a mass-averaged correlation of the pure component heat capacities:

$$Cp_f = \sum_i^n w_i \, Cp_i \tag{47}$$

The pure component viscosity for the gaseous species is calculated using a four parameter equation as a function of the fluid temperature:

$$\mu_i = 10^{-7}(A + BT + CT^2 + CT^3 + CT^4) \quad (Pa.s) \tag{48}$$

The viscosity of the liquid components and heavy waxes:

$$\mu_i = 10^{-3}(A + \frac{B}{T} + CT + CT^2) \quad (Pa.s) \tag{49}$$

The mixture viscosity was calculated using Wilkes mixing rule as reported by poling et al [121]:

$$\mu_f = \sum_i^n \frac{x_i \mu_i}{\sum_j x_i \emptyset_{ij}} \tag{50}$$

where $\emptyset_{ij}$ is a dimensionless energy parameter defined as follows:

$$\Phi_{ij} = \frac{1}{\sqrt{8}}\left(1 + \frac{M_i}{M_j}\right)^{-\frac{1}{2}}\left[1 + \left(\frac{\mu_i}{\mu_j}\right)^{\frac{1}{2}}\left(\frac{M_j}{M_i}\right)^{\frac{1}{4}}\right]^2 \tag{51}$$

The pure component thermal conductivity for the gaseous species and the liquid species and heavy waxes is calculated using a four parameter equation as a function of the fluid temperature:

$$k_i = A + BT + CT^2 + DT^3 \quad (\frac{\mathrm{W}}{\mathrm{m.K}}) \tag{52}$$

The mixture thermal conductivity was calculated using a method analogous to Wilke's mixing rule.

$$k_f = \sum_i^n \frac{x_i k_i}{\sum_j x_i \emptyset_{ij}} \tag{53}$$

The constants in (Eq 45-52) were adopted from Yaws handbook [122, 123] and are shown in Appendix A.

The density of the fluid mixture (ρ_f) was calculated from the Brinkman equation using a molar average sum of the individual species.

$$\rho_f = \sum_i^n x_i \rho_i \tag{54}$$

The density of the gas at the inlet was calculated using the ideal gas law as follows:

$$\rho_{f,Inlet} = \frac{\text{P}\times\text{R}}{T_{inlet} \times MW_n} \tag{55}$$

where T_{inlet} represents the temperature at the inlet of the reactor.

3.1.5.2. Physical properties of the solid structure (solid domain)

The thermal conductivity and heat capacity of the solid particles making up the reactor bed packing are assumed to be constant and were obtained from different databases on Knovel.

Table 6: Thermal conductivity of the solid domain

Material	Thermal conductivity (W/m.K)
Silica (SiO_2)	0.32
Alumina (Al_2O_3)	19.13
Cobalt (Co)	78.56
Cupper (Cu)	380

Table 7: Heat capacity of the solid domain

Material	Thermal conductivity (J/kg/K)
Silica (SiO_2)	300
Alumina (Al_2O_3)	992.1
Cobalt (Co)	460
Cupper (Cu)	3900

3.1.6. Boundary conditions

The transport expressions mentioned in the previous section are solved with appropriate boundary conditions pertaining to:

1) Inlet boundary conditions at $z = z_4$:

1.1) Inlet mass flow (Boundary I, Figure 9):

$$\dot{m} = \dot{m}_o \tag{56}$$

Where $\dot{m}_o$ is the standard mass flow rate at the reactor inlet.

The standard mass flow rate is specified as the volumetric flow rate of a gas at standard density. The standard density ρ_s is calculated by dividing the average molar mass MW_n by the standard volume V_m(the volume of one mole of an ideal gas at standard temperature (273.15 K) and pressure (1 bar)).

$$\rho_s = \frac{MW_n}{V_m} \tag{57}$$

$$\dot{m}_o = V_m \times \rho_s \tag{58}$$

1.2) Inlet composition (Boundary I, Figure 9):

$$x_{N_2} = \dot{x}_{N_2}, x_{CO} = \dot{x}_{CO} \ , x_{H_2} = \dot{x}_{H_2} \tag{59}$$

where $\dot{x}_{CO}$, $\dot{x}_{H_2}$ and $\dot{x}_{N_2}$ are the inlet mole fractions of CO, H_2, and N_2 respectively.

The inlet mole fractions of the reactive gases (CO and H_2) are calculated based on the syngas ratio (H_2/CO) which was (2:1) in this case, while N_2 mole fraction was taken

as (2%). Since the reaction takes place only in the catalytic bed zone (Figure 9), the mole fractions of the hydrocarbon species at the inlet were taken as zero.

$$\dot{x}_{N_2} = 0.02 \tag{60}$$

$$\dot{x}_{CO} = \frac{1}{\text{syngas ratio}+1} \times (1 - \dot{x}_{N_2}) \tag{61}$$

$$\dot{x}_{H_2} = \frac{\text{syngas ratio}}{\text{syngas ratio}+1} \times (1 - \dot{x}_{N_2}) \tag{62}$$

1.3) Inlet temperature (Boundary I, Figure 9): (63)

$$T = T_0 \tag{64}$$

where T_0 is the inlet temperature of the reactor (this was varied based on the temperature conditions used in the experimental studies)

2) Wall boundary conditions at $r = r_{bed}$:

2.1) No slip at the wall (Boundary II, III, V Figure 9):

The no-slip condition assumes that the fluid velocity relative to the wall velocity is zero. For a stationary wall as in this case study that implies that $U = 0$.

2.2) No flux at the wall (Boundary II, III, V Figure 9):

At the wall boundary, no mass flows in and out of the system, thus the total mass flux at the wall is zero.

$$-\mathbf{n}.\mathbf{N_i} = 0 \tag{65}$$

2.3) External cooling (heat transfer between the reactor and a constant temperature cooling medium) (Boundary III Figure 9):

$$-\mathbf{n}.\mathbf{q} = U_{overall}(\mathrm{T_{ext}} - \mathrm{T}) \quad (66)$$

where $\mathrm{T_{ext}}$ is the temperature of the coolant which is assumed to be equal to the wall temperature $\mathrm{T_{wall}}$, and $U_{overall}$ is the overall heat transfer coefficient.

The overall heat transfer coefficient represents the overall heat transmittance from the core of the reactor bed to the vicinity of the wall and is defined using the following correlation suggested by Mamonov et al[91].

$$U_{overall} = \left(\frac{d_t}{8\lambda_{er}} + \frac{1}{\alpha_{w,int}} + \frac{d_w}{\lambda_w} + \frac{1}{\alpha_{w,ext}}\right) \quad (67)$$

where d_t is the inner tube diameter, λ_{er} is the effective radial heat coefficient of the catalyst bed, $\alpha_{w,int}$ is the radial heat transfer coefficient near the wall, d_w is the wall thickness, λ_w is the thermal conductivity of the wall, $\alpha_{w,ext}$ is the heat transfer coefficient from the tube wall to the cooling liquid. Values for λ_w and $\alpha_{w,ext}$ were taken from Mamonov et al[91]

2.2.1) Radial Heat Transfer Coefficient at the Wall:

The effective radial heat transfer coefficient at the wall $\mathrm{h_{wall}}$ is one of the main parameters that determine the rate of heat transfer in PB. This parameter quantifies the increase in heat transfer resistance at the wall of the PB reactor, due to the changes in the bed thermal conductivity during the FT reaction and the presence of a viscous boundary layer in the vicinity of the wall [124]. A number of correlations to properly estimate the $\mathrm{h_{wall}}$ value has been proposed in the literature [125-133]. Specchia and Baldi proposed a two-parameter correlation which has shown to satisfactorily predict the $\mathrm{h_{wall}}$ value in PB reactors with different particle geometries[35]. This was used in the present work.

$$h_{wall} = h_{wall,o} + h_{wall,g} \quad (68)$$

$$h_{wall,o} = \frac{k_f}{d_p}\left(2\epsilon_{bed} + \frac{1-\epsilon_{bed}}{\frac{k_f}{k_s}\times\gamma_w+\varphi_w}\right) \quad (69)$$

$$h_{wall,g} = \frac{k_f}{d_p} \times 0.0835 \times Re^{0.91} \quad (70)$$

where Re represents the Reynold numbers, $h_{wall,o}$ represents the stagnant/conductive contribution while $h_{wall,g}$ represents the convective contribution

The heat transfer model for the conductive/stagnant contribution at the wall (Eq 69) accounts for the heat conduction to the fluid in the void space and heat conduction from the particle-wall contact points through the solid phase. The dimensionless parameters γ_w and φ_w in (Eq 69) are dependent on the geometry of the contact surface between the particle and the wall. For spherical particles the parameters are defined as follows[128]:

$$\gamma_w = \frac{1}{3}, \varphi_w = 0.0024 \times \left(\frac{d_t}{d_p}\right)^{1.58} \quad (71)$$

The convective contribution to the radial heat transfer coefficient at the wall (Eq 70) takes into account the effect of the radial mixing of the fluid in the void space on the h_{wall} value. This model was shown to provide satisfactory results over a wide range of Reynolds numbers ($10 \leq Re \leq 1200$).

2.2.2) Effective Radial Thermal Conductivity:

The second parameter affecting the heat transfer in PB is the radial effective thermal conductivity λ_{rad}. A two parameter correlation that adequately predicts the effective radial heat transfer coefficient in PB was taken from Specchia and Baldi[128].

$$\lambda_{\mathrm{rad}} = \lambda_{\mathrm{rad,o}} + \lambda_{\mathrm{rad,g}} \tag{72}$$

$$\lambda_{\mathrm{rad,o}} = \left(\epsilon_{bed} + \frac{\beta(1-\epsilon_{bed})}{\varphi + \frac{k_f}{k_s} \times \gamma} \right) k_f \tag{73}$$

$$\lambda_{\mathrm{rad,g}} = \frac{\mathrm{Re_{pa}Pr}}{8.65\left(1+19.4\times\frac{{d_p}^2}{d_t}\right)} k_f \tag{74}$$

where Pr represents the Prandtl number, β, γ, and φ represent the ratios between characteristic lengths and the particle diameter (the particles are assumed to be spheres), $\lambda_{\mathrm{rad,o}}$ represents the static/conduction contribution while $\lambda_{\mathrm{rad,g}}$ represents the convective contribution.

$\lambda_{\mathrm{rad,o}}$ takes into account the heat transfer due to conduction from the fluid phase to the solid phase, while $\lambda_{\mathrm{rad,g}}$ takes into account the convective contribution of the radial mixing and thus depends on the hydrodynamics of the system and the fluid physical properties.

Kunii and Smith reported that for spherical particles $\beta = 1$ for almost all packed beds, $\gamma = \frac{2}{3}$ and $\varphi = 0.22(\epsilon_{bed})^2$ based on fitting of experimental data for $\lambda_{\mathrm{rad,o}}$ [134].

3) Outlet Boundary conditions at $z = z_1$:

3.1) Outlet pressure (Boundary IV Figure 9):

$$\mathbf{n}^{\mathrm{T}}\left[-\mathrm{p}\mathbf{I} + \mu_{\mathrm{f}}\frac{1}{\epsilon_{\mathrm{bed}}}(\boldsymbol{\nabla}\mathbf{u} + (\boldsymbol{\nabla}\mathbf{u})^{\mathrm{T}}) - \frac{2}{3}\mu_{\mathrm{f}}\frac{1}{\epsilon_{\mathrm{bed}}}(\boldsymbol{\nabla}\cdot\mathbf{u})\mathbf{I}\right]\mathbf{n} = -\mathrm{p_e} \tag{75}$$

This boundary condition specifies the normal stress which is equal to the pressure along the outlet boundary. At this boundary, the outlet pressure is adjusted in order to suppress backflow.

3.2) Outflow boundary (Boundary IV Figure 9):

This condition states that heat transfer occurring at the outlet is only by convection and the temperature gradient in the normal direction is zero

$$-\mathbf{n}.\mathbf{q} = 0 \tag{76}$$

Also at the outflow boundary, it is assumed that the mass transport of the species is dominantly by convection (diffusive flux is zero).

$$-\mathbf{n}.\rho_f w_i \sum D_{ik} d_k = 0 \tag{77}$$

3.1.7. Reactor performance calculations

The FT reactor performance was quantifiably analyzed in terms of CO conversion (X_{CO}), CH_4 selectively (S_{CH_4}) and C_{5+} selectively ($S_{C_{5+}}$), which are calculated as follows:

$$X_{CO}\% = \frac{F_{CO,in} - F_{CO,out}}{F_{CO,in}} \times 100 \tag{78}$$

where $F_{CO,in}$ and $F_{CO,out}$ are the molar flow rates of CO at the inlet and the outlet of the reactor respectively.

The local methane selectively is calculated at every point in the reactor as follows:

$$S_{CH_4,l}\% = \frac{R_{CH_4}{}^{Ma}}{(-R_{CO}{}^{YS})} \times 100 \tag{79}$$

However, the average methane selectivity in the reactor bed was calculated by volume integration of (Eq 79) as follows:

$$S_{CH_4}\% = \frac{\int_0^V R_{CH_4}{}^{Ma}\, dV}{\int_0^V -R_{CO}{}^{YS} dV} \times 100 \tag{80}$$

It is important to note that $R_{CH_4}{}^{Ma}$ is unbounded, therefore, at high temperatures, its value can exceed the rate of consumption of CO, results in methane selectively greater than 100% which is physically impossible. Therefore, a constraint was imposed in the model calculations $R_{CH_4}{}^{Ma} = R_{CO}{}^{\mathrm{YS}}$ when ($R_{CH_4}{}^{Ma} > -R_{CO}{}^{\mathrm{YS}}$).

The selectively of the C_{5+} hydrocarbons is calculated as follows:

$$S_{C_{5+}}\% = 100 - S_{CH_4} - S_{C_2} - S_{C_3} - S_{C_4} \quad (81)$$

where S_{C_i} is the selectively of the carbon species from C_2-C_4, which was calculated similarly to (Eq 80)

3.1.8. Model development under SCF-FT conditions

To model the hydrodynamics of the fixed bed reactor bed under SCF conditions similar approach to the previous section was followed in terms of momentum, mass and heat transfer balance equations. However, the following changes have been implemented to highlight the unique characteristics of SCF in terms of the physicochemical properties of the fluid under supercritical conditions.

1) In the momentum transport expressions the bed porosity was calculated using a predictive mean voidage correlation by Benyahia and O'Neill [135]:

$$\epsilon_{\mathrm{bed}} = 0.1504 + \frac{0.2024}{\emptyset_p} + \frac{1.0814}{(\frac{d_t}{D_p}+0.1226)^2} \quad (82)$$

The calculated porosity assuming perfect spherical particles with 200 μm was found to be 0.352, which is close to values reported in the literature [85, 110, 136].

2) In the mass transport expressions, the mass conservation equations were defined using a simplified FT reaction stoichiometric equation:

$$\mathrm{CO} + 2\mathrm{H_2} \rightarrow -[(\mathrm{CH_2})_\mathrm{n}] - +\mathrm{H_2O} \quad (83)$$

where $-(CH_2)_n -$ is the methylene group polymerizing into a different hydrocarbon chain. Stoichiometric coefficient (ν_i) of -2, -1, +1, +1 are used for H_2, CO, H_2O and $-(CH_2)_n -$ respectively, while the supercritical fluid hexane (C_6H_{14}) was set as the mass constraint component.

3) The molar volume of hexane used to calculate the binary diffusivities D_{ik} for the Maxwell Stefan diffusion model (Eq 19) was 131.63 $\frac{\mathrm{cm}^3}{\mathrm{mol}}$, while the molar volume of the representative $-(CH_2)n -$ monomer was calculated as a molar weight average sum using the molar volumes of the individual hydrocarbon species based on the Anderson-Schulz-Flory (ASF) product distribution. The hydrocarbon species lumped in the $-(CH_2)n -$ representative component is (C_1, C_2-C_4, C_5-C_{15} and wax represented as CH_4, C_3H_8, $C_{10}H_{22}$, and $C_{22}H_{46}$, respectively). To calculate the product distribution, the chain growth probability (α) was set as 0.83 based on experimental analysis.

4) In the heat transfer expressions, the solid phase thermal conductivity and heat capacity of the reactor bed were calculated using a volume-average correlation of the inert packing and the catalyst as per reactor packing specifications used in the SCF experiments.

5) The kinetics of the SCF model of operation differ from that under GP conditions. In this case, the CO disappearance rate per unit mass of catalyst is calculated using a fugacity-based model by Elbashir and Roberts [69, 137]:

$$(-R_{CO}) = \frac{K f_{CO}^{\frac{1}{2}} f_{H_2}^{\frac{1}{2}}}{\left(1+K_1 f_{H_2}^{\frac{1}{2}}+K_2 f_{CO}^{\frac{1}{2}}+K_3 f_{CO}\right)^2} \quad (84)$$

where f_{co} and f_{H_2} are the fugacity's of CO and H_2 respectively; *K*, K_1, K_2, K_3 are kinetic constants.

Numerical values of the kinetic rate constant *k* and the equilibrium constants K_i in (Eq 84) were estimated by Mogalicherla et al. [67] from experimental data with 15% Co/Al_2O_3 catalyst. The temperature dependence of the kinetic parameters is given below:

$$k(T) = 4 \times 10^{-4}. \exp\left[-124979(\frac{1}{T} - \frac{1}{513}\right] \quad \frac{mol}{g_{cat}.min.bar} \quad (85)$$

$$(K_1(T) = 0.169. \exp\left[6025.98(\frac{1}{T} - \frac{1}{513})\right] \quad \frac{1}{bar^{0.5}} \quad (86)$$

$$K_2(T) = 0.2. \exp\left[-17981.71(\frac{1}{T} - \frac{1}{513})\right] \quad \frac{1}{bar^{0.5}} \quad (87)$$

$$K_3(T) = 1.5 \times 10^{-4}. \exp\left[11911(\frac{1}{T} - \frac{1}{513})\right] \quad \frac{1}{bar^{0.5}} \quad (88)$$

The fugacity of CO (f_{co}) and H_2 ($f_i$was estimated by coupling the Modified Soave-Redlich-Kwong EOS (MSRK) along with appropriate mixing rules proposed by Yermakova and Anikeev [138]. The ability of the MSRK EOS to predict the phase behavior of the SCF-FT reaction mixture was well demonstrated in the literature [138-

140], which was the primary reason for particularly selecting the MSRK EOS for this analysis.

Modified Soave Redlich Kwong Equation of State:

$$P = \frac{RT}{V_m - b_m} - \frac{a_m(T)}{V_m(V_m + b_m)} \tag{89}$$

$$a_m = \sum_{j=1}^{n}\sum_{i=1}^{n} x_i\, x_j a_{ij} \text{ and } b_m = \sum_{j=1}^{n}\sum_{i=1}^{n} x_i\, x_j b_{ij} \tag{90}$$

$$a_{ii} = \frac{\alpha_i(T)0.42748R^2{T_{ci}}^2}{P_{ci}} \tag{91}$$

$$b_{ii} = \frac{0.08664RT_{ci}}{P_{ci}} \tag{92}$$

$$a_{ij} = (1 - k_{ij})\sqrt{a_{ii}a_{jj}} \tag{93}$$

$$b_{ij} = (1 - c_{ij})\frac{(b_{ii} + b_{jj})}{2} \tag{94}$$

$$\alpha_i(T) = [1 + m_i\left(1 - \sqrt{\frac{T}{T_{ci}}}\right)]^2 \tag{95}$$

$$m_i = 0.48 + 1.574\omega_i - 0.176{\omega_i}^2 \tag{96}$$

$$\gamma_i = 2\sum_{j=1}^{n} x_i a_{ij} \text{ and } \beta_i = 2\sum_{j=1}^{n} x_j b_{ij} - b_m \tag{97}$$

$$Z = \frac{PV_m}{RT}\ ; A = \frac{a_m P}{(RT)^2}\ ; B = \frac{b_m P}{(RT)} \tag{98}$$

$$Z^3 - Z^2 - Z(B^2 - B + A) - AB = 0 \tag{99}$$

$$\ln f_i = \ln\left[\frac{x_i RT}{V_m - b_m}\right] + \frac{\beta_i}{V_m - b_m} + \frac{\gamma_i\,\beta_i}{RT{b_m}^2}\left[\ln\frac{(V_m + b_m)}{V_m} - \frac{b_m}{V_m + b_m}\right] + \frac{\gamma_i}{RTb_m}\ln(\frac{V_m + b_m}{V_m}) \tag{100}$$

The critical temperature (T_{ci}) and pressure (P_{ci}) of the hydrocarbon species considered in the SCF-FT reaction are summarized in Tables 8 and 9.

Table 8: Critical pressure of the hydrocarbon species in the SCF-FT reaction

Specie	Critical pressure (bar)
C_{22}	10
C_2C_4	42.48
C_5C_{15}	21.1
C_6H_{14}	30.25
CH_4	45.99
CO	34.99
H_2	13.13
H_2O	220.55

Table 9: Critical temperature of the hydrocarbon species in the SCF-FT reaction

Specie	Critical Temperature (K)
C_{22}	369.8
C_2C_4	617.7
C_5C_{15}	507.6
C_6H_{14}	190.6
CH_4	132.9
CO	33.19

Table 9 continued

Specie	Critical Temperature (K)
H_2	647.1
H_2O	369.8

6) Physical properties

The physical properties of n-hexane (density, viscosity, heat capacity, thermal conductivity) at supercritical conditions P = 80 bar and T > 508 K were obtained from the National Institute of standards and technology (NIST) chemistry webbook [141]. The physical properties were obtained as raw data and were fitted to obtain temperature dependent correlations that would be used in the reactor bed code as shown in Figures 10, 11, 12 and 13.

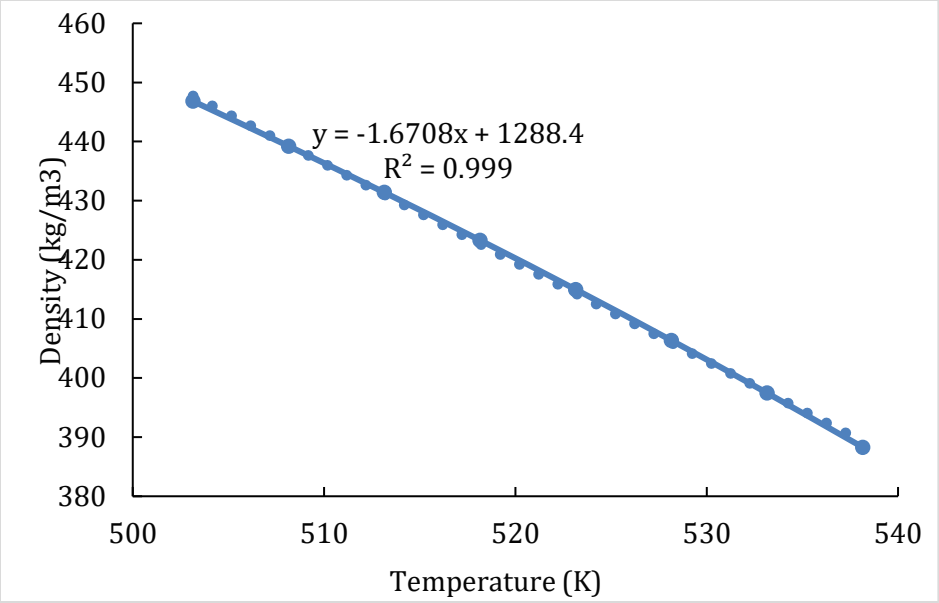

Figure 10: Density of hexane at supercritical conditions P = 80 bar and T > 508 K as a function of temperature

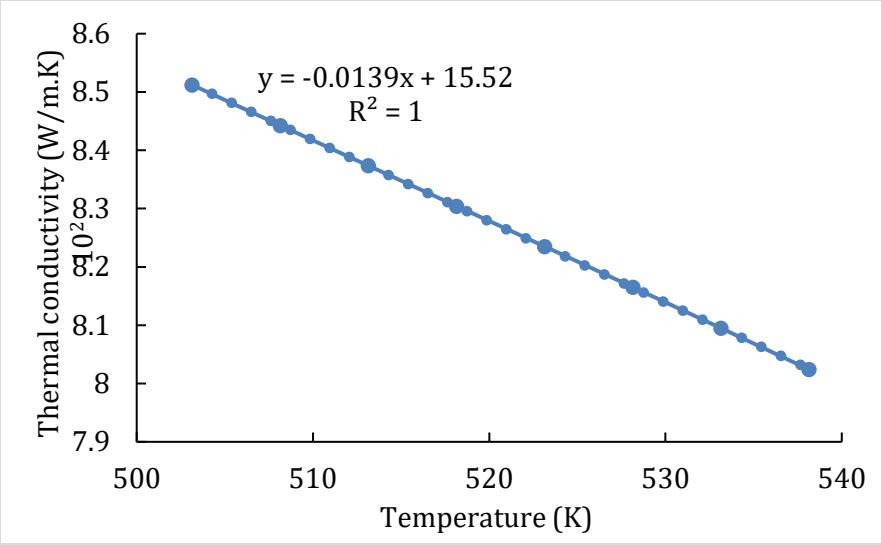

Figure 11: Thermal conductivity of hexane at supercritical conditions P = 80 bar and T > 508 K as a function of temperature

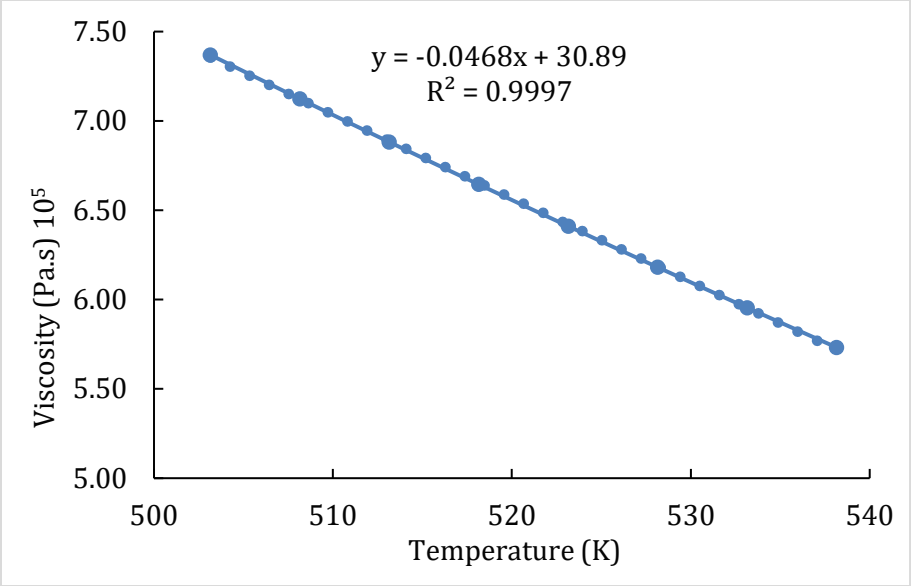

Figure 12: Viscosity of hexane at supercritical conditions P = 80 bar and T > 508 K as a function of temperature

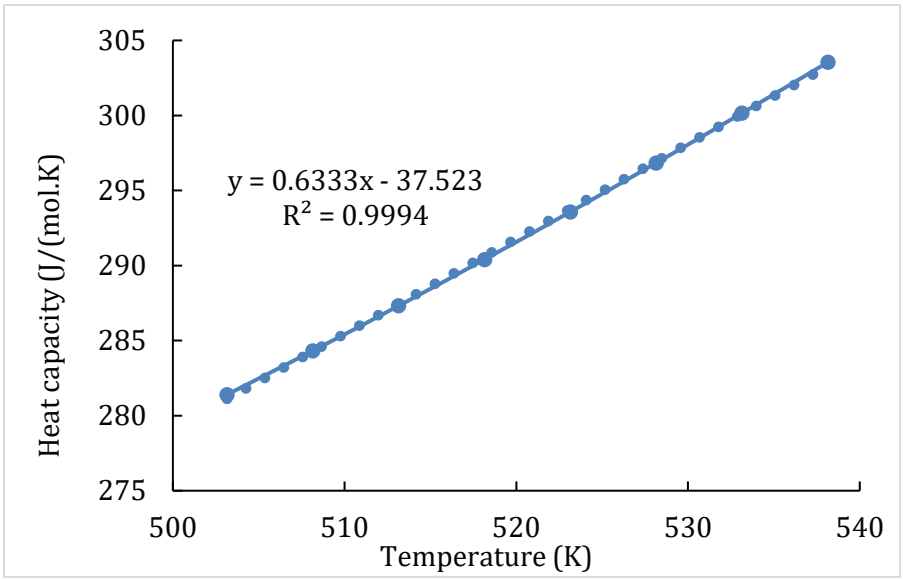

Figure 13: Heat capacity at supercritical conditions P = 80 bar and T > 508 K as a function of temperature

7) The inlet boundary condition used in the Brinkman's equation (mass flow rate) was calculated at the reactor inlet conditions and not at standard conditions. This is due to the fact that at standard conditions, hexane is at liquid conditions, while at the reactor inlet, hexane is at supercritical conditions. The steps to calculate the total mass flow rate (hexane+syngas) at the inlet of the reactor are done as follows:

The total mass flow rate at the inlet (Boundary I, Figure 9) is defined as:

$$\dot{m} = \dot{m}_{hexane} + \dot{m}_{syngas} \tag{101}$$

where $\dot{m}_{hexane}$ and $\dot{m}_{syngas}$ are the mass flow rates of hexane and syngas respectively.

The number of moles of syngas (n_{syngas}) entering the reactor system was calculated using the ideal gas law as follows:

$$\mathrm{n_{syngas}} = \frac{\mathrm{P_{syngas} \times Q_{syngas,stp}}}{\mathrm{R \times T_s}} \tag{102}$$

where P_{syngas} is the partial pressure of syngas (20 bar) and $\mathrm{Q_{syngas,stp}}$ is the volumetric flow rate of syngas at STP conditions, R is the universal gas constant and T_s is the standard temperature (273.15 K).

The number of moles of supercritical solvent hexane (n_{hexane}) entering the reactor system are calculated using the solvent to syngas ratio (3:1).

$$n_{hexane} = 3 \times n_{syngas} \tag{103}$$

The mass flow rate for syngas and hexane was found as follows:

$$m_{hexane} = MW_{hexane} \times n_{hexane} \tag{104}$$

$$m_{syngas} = MW_{syngas} \times n_{syngas} \tag{105}$$

The molecular weight of the syngas was calculated using a molar average sum of CO and H_2:

$$MW_{syngas} = \dot{x}_{CO} MW_{CO} + \dot{x}_{H_2} MW_{H_2} \quad (106)$$

1) The external cooling heat transfer boundary condition (Boundary III Figure 9) is used when the reactor tubes are jacketed in which heat is supplied/removed by a constant flow of thermic fluid. (Eq 67) represents a jacketed heat transfer equation that was used for thermal profile comparisons and for scale-up studies. However, for model validation studies, the Fourier's law of heat conduction was used as the experimental data obtained from the high pressure FT rig utilized a furnace programmed to set the skin temperature at a constant value of specified temperature.

Fourier's law of heat conduction:

$$q = -k_{stainless} \nabla T \quad (107)$$

where, $k_{stainless}$ represents the thermal conductivity of stainless steel.

2) The kinetic model (Elbashir and Roberts) used in this study is derived to only predict the amount of CO consumed during the FT reaction. To predict the methane and C5+ selectivity, detailed kinetic models that predict the product distribution of the hydrocarbon products in FT is required. Therefore, the selectivity of methane and C_{5+} hydrocarbons have not been calculated in this case.

4. RESULTS AND DISCUSSION

4.1. Comparison of model prediction with experimental data for GP-FT operation (PB and MFECC reactor beds)

4.1.1. Model validation for GP-FT operation (PB and MFECC reactor beds)

The developed model was validated with experimental data reported by Sheng et al[85, 110] to test the model robustness under different experimental conditions. Two different experiments were carried out to compare between the PB and MFECC bed operating under GP conditions. The experiment was conducted in a stainless steel tubular reactor with a wall thickness 0.079" and 0.59" ID. The total height of the reactor bed was 18" pertaining to; 8" pre-packing zone, 4" effective zone (catalytic bed), 6" post-packing zone. The MFECC bed consisted of 7.4vol% copper fibers, 62.6vol% porosity and 30vol% (15% Co/Al_2O_3). The PB was diluted to the same catalyst density as the MFECC bed with fresh alumina of different particle sizes. The overall bed space in the PB comprised of 30vol% (15% Co/Al_2O_3), 36vol% % porosity and 34% fresh alumina. The average particle size of the catalyst particles in the reactor bed was 149–177 μm.

The experimental results were obtained by varying the inlet temperature over a range from 498.15-528.15 K at 20 bar pressure and H_2/CO ratio of 2:1 at a constant gas hourly space velocity (GHSV) 5000 1/hr. In all simulation runs, the parameters (inlet temperature, pressure, gas velocity, and H_2/CO ratio) were similar to those used in the experimental study. 160 μm particle diameter was used in the simulation to represent the average particle size 149–177 μm used in the experiments as reported by Sheng et al[110]. It should be noted that the kinetic parameters used in this modeling study, were estimated

using 0.48%Re 25% Co/Al_2O_3 [38, 55]. Since, the experiments were conducted using 15% Co/Al_2O_3, while using the same parameters in the kinetic model, the kinetic rates were tuned down. This was done since the intrinsic kinetics follows the same mechanism however the activity of the catalyst with higher metal loading is expected to be higher.

Four sets of results were used to validate the model with the experimental study including; CO conversion, maximum temperature deviation from the centerline to the reactor wall (T_{max}-T_{wall}), CH_4 selectivity and C_{5+} selectivity. The simulation results for the MFECC bed has shown good agreement with the experimental predictions for CO conversion, (T_{max}-T_{wall}), CH_4 selectivity and C_{5+} selectivity as shown in Figures 14,15,16 and 17. For the PB case, the CO conversions from the modeling results are consistently in good agreement with the experimentally obtained PB performance under all conditions as shown in Figure 18. Moreover, the (T_{max}-T_{wall}), CH_4 selectivity and C_{5+} selectivity results have shown good agreement with the experimental results from 498.15-518.15 K as displayed in Figures 19, 20 and 21. However, at 528.15 K the deviation between the modeling and the experimental predictions becomes high. This deviation in model predictions from experimental data could be attributed to the sensitivity of the kinetic parameters that are generated using a ruthenium promoted catalyst of different loading reported by Stamenic et al and Todic et al[38, 55]. The lower CH_4 selectivity predicted from the model at a high operating temperature (528.15 K) can be due to the fact that methane formation could possibly follow multiple reaction routes on FT sites[142, 143]; 1) termination of the chain growth, 2) through intermediates participating in chain propagation and 3) due to hydrogenation of surface carbon. The latter methane formation

pathway does not follow the polymerization/chain growth route for FT synthesis. However, the kinetic model used in this modeling study to predict the methane selectivity has not considered the secondary pathway for methane formation, thus under predicts the methane selectivity relative to the experimental data. Consequently, the selectivity of C_{5+} products at 528.15 K is overpredicted by the model when compared to experimental data.

Further analysis of the modeling and experimental results as shown in Figures 15 and 19 reveals that the deviation of the reactor wall temperature from the centerline temperature for the PB is higher and increases at a faster rate than the MFECC bed under all temperature conditions (498.15-528.15 K). However, it can be noted that when the inlet temperature reaches 528.15 K, a drastic increase of the centerline temperature inside the PB occurs. This rapid ignition of the PB temperature leads to the formation of a hotspot and a rapid decrease in the catalyst activity. Such effect is not observed in the MFECC bed due to the high thermal conductivity of the copper fibers which aided in eliminating the formation of hotspots even at a high operating temperature (528.15 K).

A close comparison between the PB and MFECC in terms of CO conversion levels indicates that the MFECC bed provides lower conversions compared to the PB case for the same reactor temperature. However, the rapid increase in reactor temperature in the PB, leading to hot spot formation shifts the product selectivity toward lower weight hydrocarbon products. This effect can be observed in Figure16, 17, 20 and 21 where the CH_4 selectivity is higher while the C_{5+} selectivity is lower for the PB compared to the MFECC bed under all temperature conditions. Thus, the high conversion levels achieved in the PB reactors goes mostly toward the formation of methane. The results discussed

above demonstrate that the developed model is valid and applicable to quantitatively compare the performance of the PB and MFECC bed in terms of thermal profiles and hydrocarbon product selectivity.

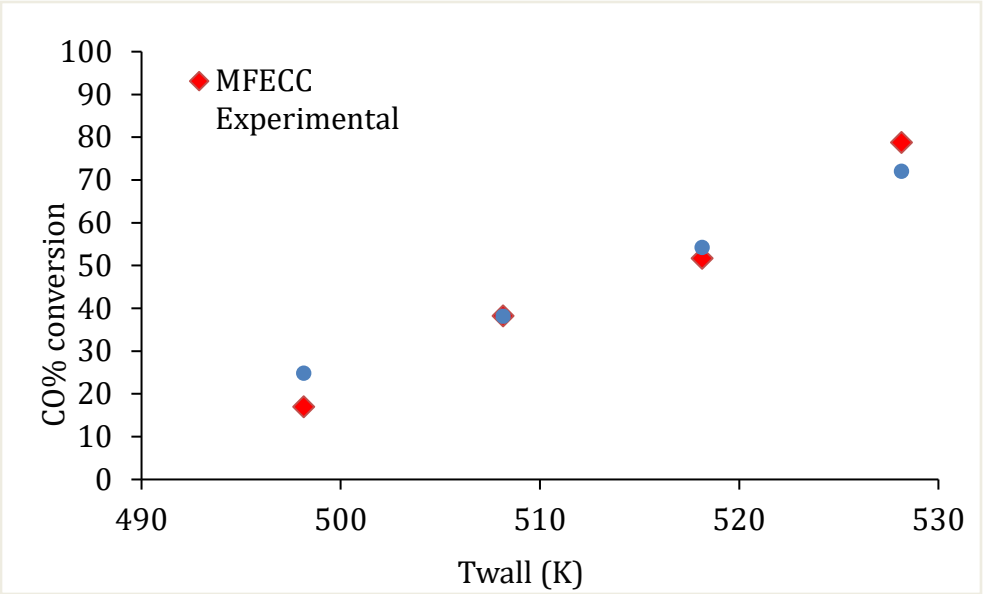

Figure 14: CO% conversion from the model and experimental results for MFECC reactor with respect to wall temperature at 2 MPa pressure for H_2:CO ratio of 2:1 and 5000 hr-1 GHSV

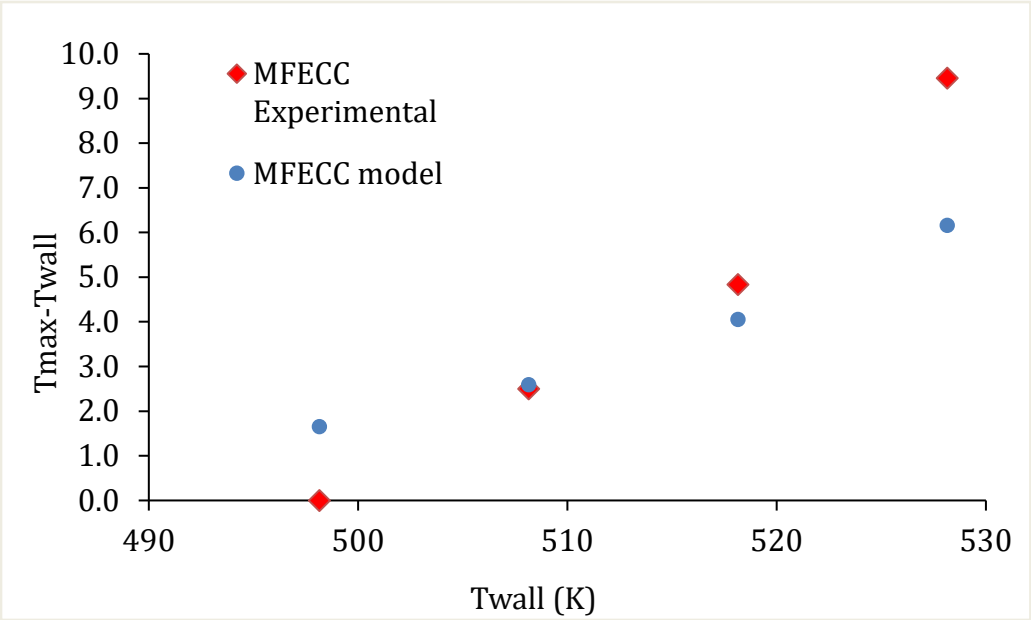

Figure 15: T_{max}-T_{wall} from the model and experimental results for MFECC reactor with respect to wall temperature at 2 MPa pressure for H_2:CO ratio of 2:1 and 5000 hr-1 GHSV

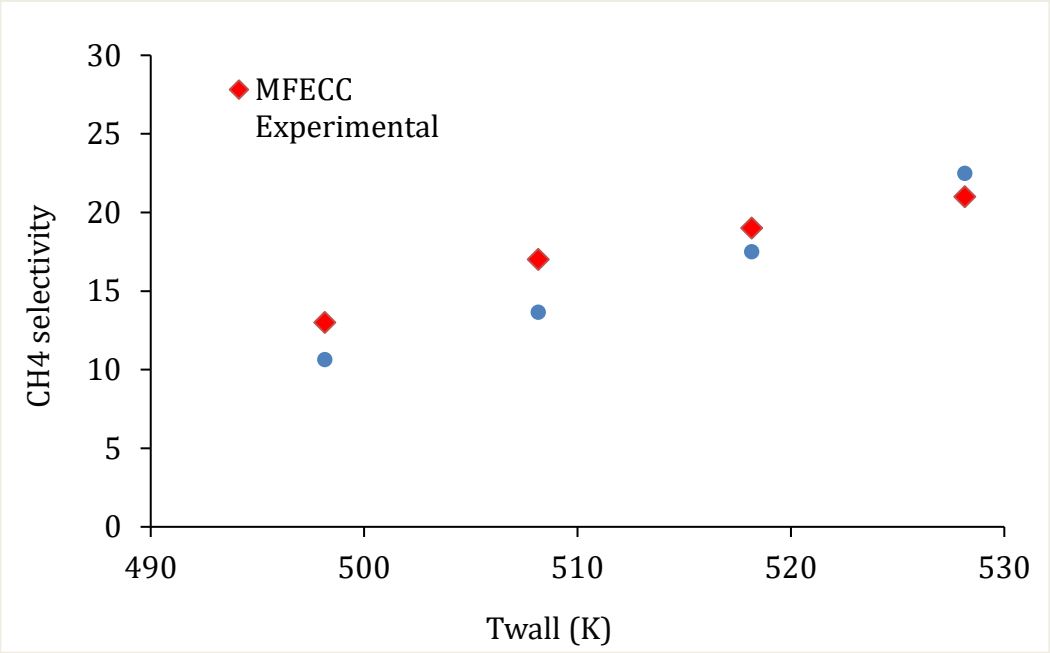

Figure 16: CH_4 selectivity from the model and experimental results for MFECC reactor with respect to wall temperature at 2 MPa pressure for H_2:CO ratio of 2:1 and 5000 hr-1 GHSV

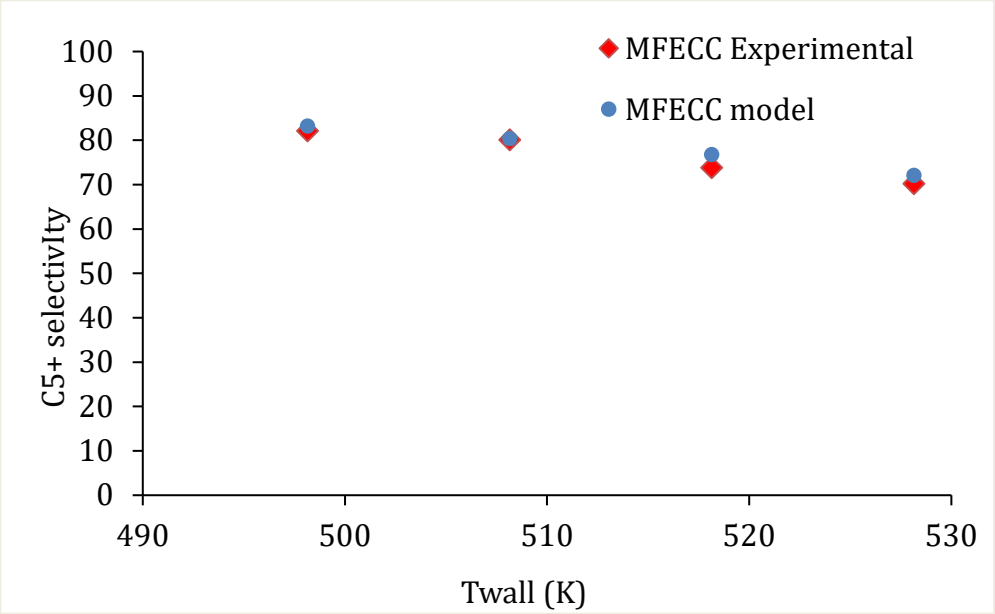

Figure 17: C_{5+} selectivity from the model and experimental results for MFECC reactor with respect to wall temperature at 2 MPa pressure for H_2:CO ratio of 2:1 and 5000 hr-1 GHSV

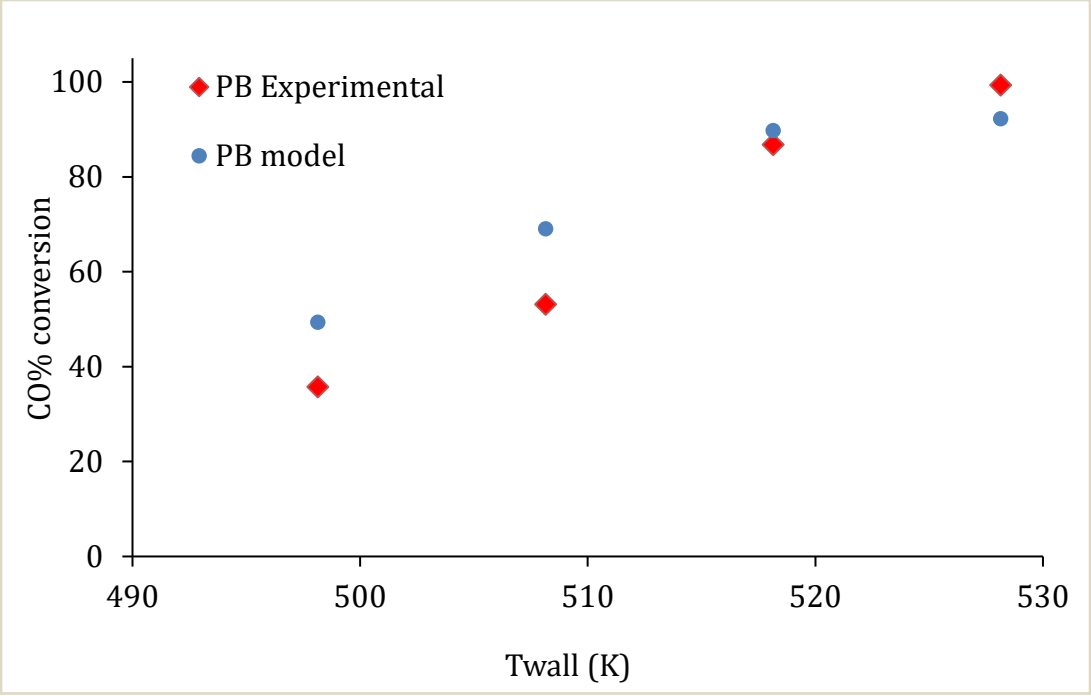

Figure 18: CO% conversion from the model and experimental results for PB reactor with respect to wall temperature at 2 MPa pressure for H_2:CO ratio of 2:1 and 5000 hr^{-1} GHSV

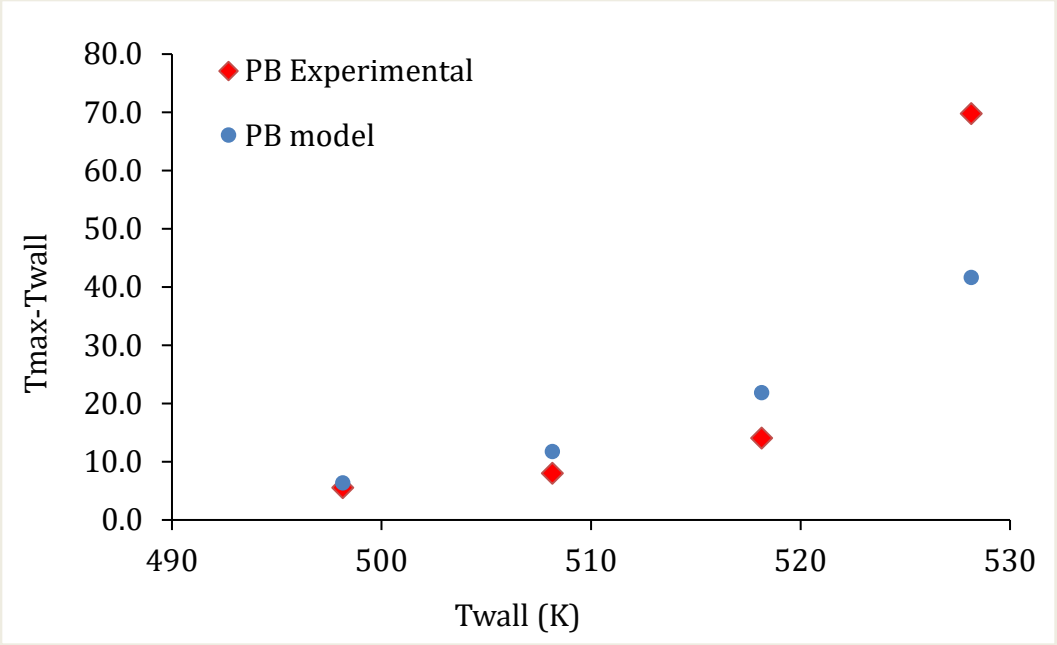

Figure 19: T_{max}-T_{wall} from the model and experimental results for PB reactor with respect to wall temperature at 2 MPa pressure for H_2:CO ratio of 2:1 and 5000 hr^{-1} GHSV

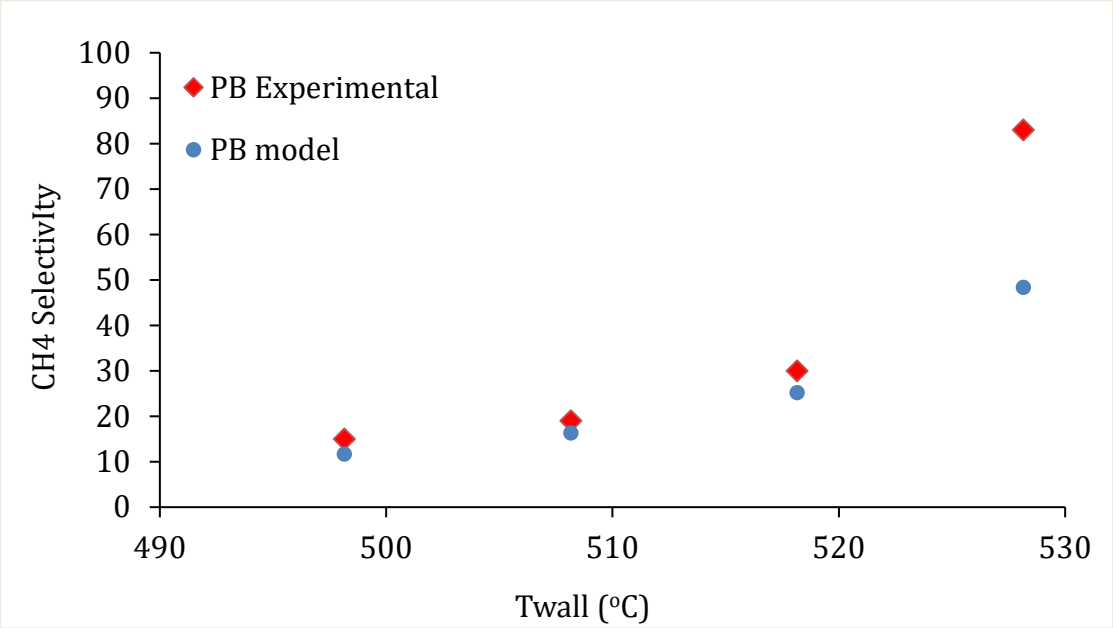

Figure 20: CH_4 selectivity from the model and experimental results for PB reactor with respect to wall temperature at 2 MPa pressure for H_2:CO ratio of 2:1 and 5000 hr-1 GHSV

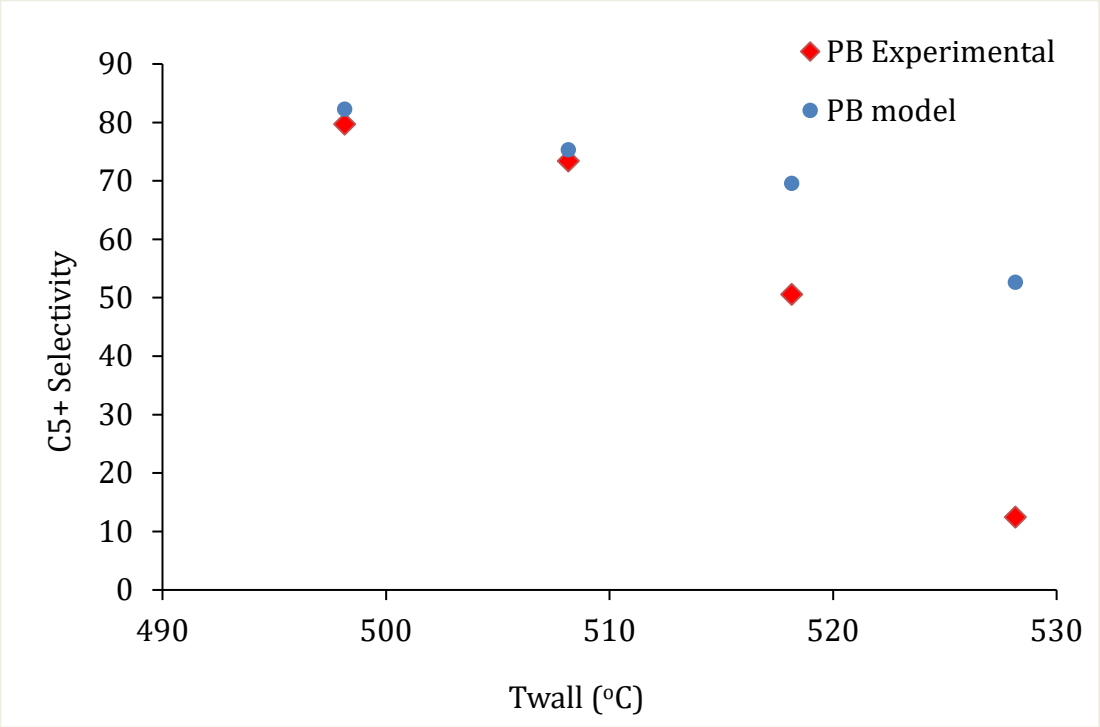

Figure 21: C_{5+} selectivity from the model and experimental results for PB reactor with respect to wall temperature at 2 MPa pressure for H_2:CO ratio of 2:1 and 5000 hr-1 GHSV

4.1.2. Comparison of thermal profiles for GP-FT operation (PB and MFECC reactor beds)

The validated 2-D model for the PB and MFECC bed was used to compare the thermal profiles of the two reactor beds using different inlet conditions; inlet temperature and GHSV. First, a side by side comparison of the thermal profiles of the PB and MFECC bed was done to study the radial and axial temperatures of both reactor beds at 528.15 K, 20 bar pressure, H_2/CO ratio of 2:1 and a constant GHSV 5000 hr^{-1}. Figure 22 shows the temperature profile predicted by the 2-D reactor model for both the PB and MFECC bed.

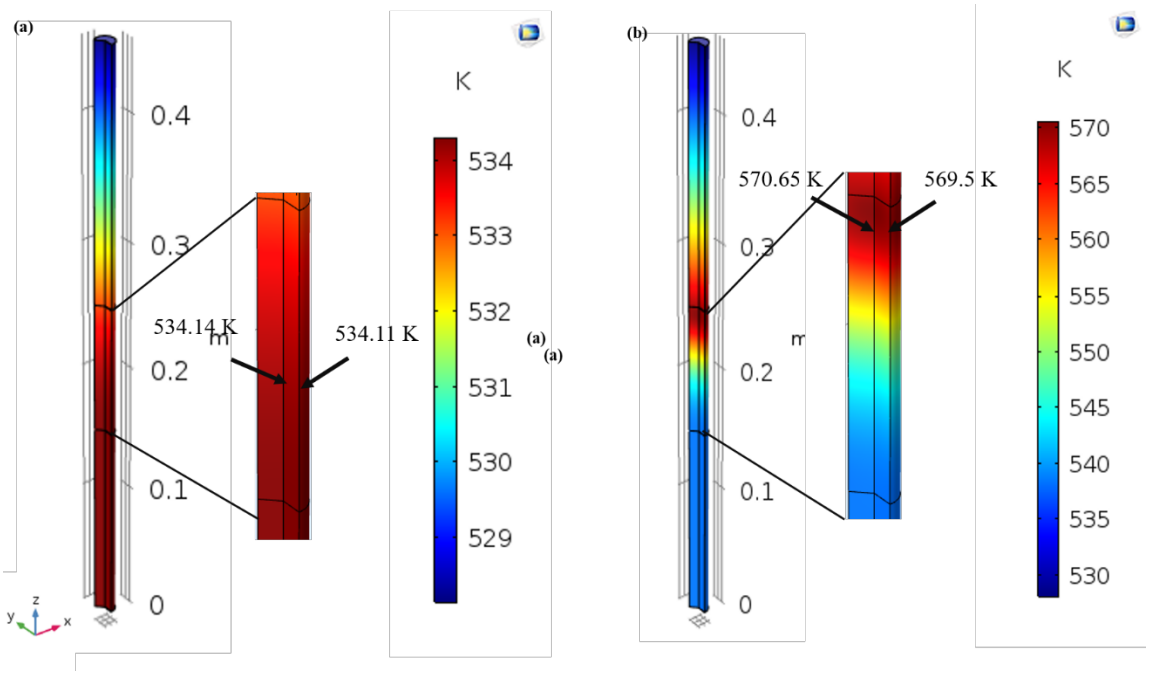

Figure 22: (a) Hot spot in MFECC bed and (b) Hotspot in PB under GP condtions for 0.59" ID (0.015 m) at 528.15 K, 20 bar pressure, H_2/CO 2:1 and 5000 hr^{-1} GHSV

As can be seen from Figure 22 (b), a hotspot is predicted in the PB at the centerline of the reactor and close to the reactor inlet. A similar finding was reported by Giovanni et al[64] for a 2-D pseudo homogenous mode of a milli-scale fixed FT bed reactor using Co-based catalyst. The axial temperature deviation for the PB reactor as predicted from the model is around 43K and the radial temperature gradient is around 1.15 K. As discussed previously, the temperature deviation predicted from the model for the PB case at 528.15K is under predicted. Therefore, the axial temperature gradient from the experiments conducted by Sheng et al was even higher around 70K. The occurrence of maximum temperature at the reactor inlet is due to the high partial pressure of the reactants at that location, which results in higher reaction rates, therefore, heat generation is significantly higher. Moreover, under typical FT conditions, the inlet of the reactor is a region where the liquid is absent since PB reactors typically operate under trickle bed behavior (the liquid produced during FT trickles down the bed). The latter has negative implications on the heat transfer process inside the PB reactor. In the lower part of the reactor, the temperature decreases steadily due to the lower reaction rates in that zone, reducing the amount of heat generated during the reaction. Moreover, the effect of liquid formation at the lower part of the reactor is more prominent (trickle bed behavior), which positively affects the rate of heat transfer within the reactor bed.

The MFECC bed provided better temperature control and a uniform temperature profile was maintained as can be seen in Figure 22(b). The maximum axial temperature deviation in the MFECC bed was only 10K and the radial temperature gradient was 0.013 K. This reduction in hot spot formation in the MFECC bed is solely the result of the high

thermal conductivity of the MFECC material. Sheng et al experimentally determined the thermal parameters of the MFECC bed and PB (effective radial thermal conductivity and wall heat transfer coefficient)[85]. The study reported that the radial effective thermal conductivity of MFECC was 56 times higher than that of alumina PB in a stagnant gas, while the inside wall heat transfer coefficient was 10 times higher.

As mentioned previously, the hydrocarbon product distribution in the FT reaction strongly depends on the temperature inside the reactor bed. The hotspot formed in the PB at 528.15 K resulted in around 100% CO conversion as per experimental results, where most of the conversion goes toward methane formation as it is favorable at high-temperature conditions (shifting the product selectivity toward lower weight hydrocarbons). Based on the modeling results shown in Figures 16 and 17, the values of CH_4 and C_{5+} selectivity in the PB at 528.15K was 48.4% and 52.68% respectively. However, as mentioned previously, these values were unpredicted by the model at 528.15 K, and a higher CH_4 selectively and thus lower C_{5+} selectivity are expected at such temperature condition. The experimental values of CH_4 and C_{5+} selectivity in the PB at 528.15K was 83% and 12.44% respectively. For the MFECC, the uniform temperature distribution resulted in higher selectivity toward higher weight hydrocarbon products and lower CH_4 selectivity. As can be seen from Figures 20 and 21 the model predictions for CH_4 and C_{5+} selectivity in the MFECC bed at 528.15 K was 22.48% and 72.2% respectively. The latter findings imply that the MFECC bed provides safe operation under high operational temperatures to achieve high conversions per tube pass in conventional Multitubular fixed bed reactors/PB without the risk of selectivity loss.

4.1.3. Effect of varying the gas hourly space velocity for GP-FT operation (PB and MFECC reactor beds)

The impact of varying the inlet gas flow rate/GHSV on the heat generation and removal for the MFECC bed and PB was investigated. The simulations were carried out by varying the GHSV while keeping the other process parameters constant (518.15 K, 20 bar pressure, H_2/CO 2:1). Figure 23 shows the effect of varying the GHSV on the reactor thermal behavior in terms of maximum temperature rise at the centerline of the reactor. For the PB bed, increasing the GHSV from 5000 to 10000 hr^{-1} results in less efficient heat removal and the maximum temperature at the centerline of the reactor increases from 566 to 628 K. This results in hotspot formation and temperature runways, as can be seen from Figure 22. This is due to the poor thermal conductivity of the PB reactor. For the MFECC bed, the maximum temperature at the centerline of the reactor remains almost constant under all GHSV conditions at 534.5 K. Therefore, operating at higher velocities induce very small changes in the thermal behavior of the MFECC bed. The observations in the thermal behavior of both the PB and MFECC discussed above can be supported by a modeling study conducted by Sheng et al, who conducted a microscale heat transfer comparison between a PB and an MFECC bed in a stagnant gas and flowing nitrogen gas[144]. They reported that 97.2% of the total heat flux transferred within the MFECC bed was found to be transported by the continuous metal fibers. This demonstrates that the continuous metal fibers were the primary conduction path for the heat transfer inside the MFECC bed. Therefore, it is expected that changing the GHSV would not have a significant effect on the thermal profile inside the MFECC bed. Moreover, they reported

the temperature distribution inside the PB and MFECC bed at two different gas velocities (0.2 m/s and 0.05 m/s), and they found the temperature of the flowing nitrogen gas at higher gas velocity decreased significantly in PB, while in the MFECC bed it did not change much. This finding indicates that increasing the gas velocity inside the MFECC provides stable temperature profiles and efficient heat transfer between the solid/fluid interfaces. On the other hand, increasing the gas velocity in the PB reactor provides inadequate heat transfer rates between the solid and the fluid interface which could possibly be the main reason in the formation of local hotspots on catalyst particles inside PB reactors. This indicates that operating at high gas velocities would have a detrimental effect on heat removal/management inside the PB reactor.

Similarly, Figure 24 shows the effect of varying the GHSV on CO conversion. It can be noted the CO conversion for the PB case decreases from 93.45-83% as the GHSV increases from 5000-10000 hr^{-1}. This finding was expected since lower residence times are associated with higher gas velocities. Although the shortening of the residence time results in lower CO conversions, however, the total amount of syngas converted into hydrocarbons is higher for higher gas velocities. Therefore, more heat generation per mole of CO consumed is expected at higher GHSV values, which also explains the ascending trend of the centerline temperature with increasing GHSV. A similar trend is observed in case of the MFECC bed, were the CO conversion decreases from 71.95-50.6% as the GHSV increases from 5000-1000 hr^{-1}. However, a steeper decrease in CO conversions with increasing GHSV was noted in the for the MFECC bed. This is mainly due to the high-temperature rise/deviation in the PB reactor, which was much more prominent than

in the MFECC as the GHSV was increased. This effect contributes to higher CO conversions, thus resulting in a slower decreasing rate of CO conversion. It should be noted that although increasing the GHSV might have negative implications from heat management and CO conversion stand point of view, however the total hydrocarbons productivity per catalyst mass is higher as the GHSV increases. The ability MFECC bed to provide near isothermal operation hence selectivity control even when the gas velocity is increased, raises the opportunity to achieve higher hydrocarbon productivity per catalyst mass, thus increasing the catalyst utilization.

The performance of the PB and MFECC bed at different GHSV values was evaluated in terms of the hydrocarbon product selectivity. As mentioned previously, the CO conversions were higher inside the PB compared to the MFECC under all GHSV conditions. Thus, the total mass productivity of the hydrocarbons (total amount of hydrocarbons produced) is expected to be higher inside the PB reactor for the same inlet gas velocity, due to the higher CO conversions associated with the PB reactor. However, the productivity of the desired products specifically, selectivity toward C_{5+} was significantly lower than the MFECC as shown in Figure 25. Most importantly, Figure 26 indicates that the selectivity of the most undesired product methane was significantly high in the PB reactor because of the relatively high-temperature gradients inside the reactor bed. The CH_4 and C_{5+} selectivity for the PB was 42.2% and 54.4% respectively at 5000 hr^{-1} GHSV. However, the CH_4 selectivity in the PB reactor goes up to 100% at 10000 hr^{-1} GHSV, resulting in 0% production of the C_{5+} hydrocarbons. Therefore, the total productivity of the desired hydrocarbons per catalyst mass is higher when using an

MFECC bed. As mentioned previously in the introduction section, the single pass conversion in Multitubular/PB is kept at 50% or lower to avoid temperature runways. The results discussed above, prove the potential of MFECC bed in minimizing this drawback associated with PB reactors. The high thermal conductivity of the MFECC bed provided efficient temperature control within the reactor bed, which offers a better opportunity to minimize the selectivity of methane while maximizing the selectivity toward C_{5+} products even at high CO conversions. This is one of the main requirements in industrial applications of FT reactors.

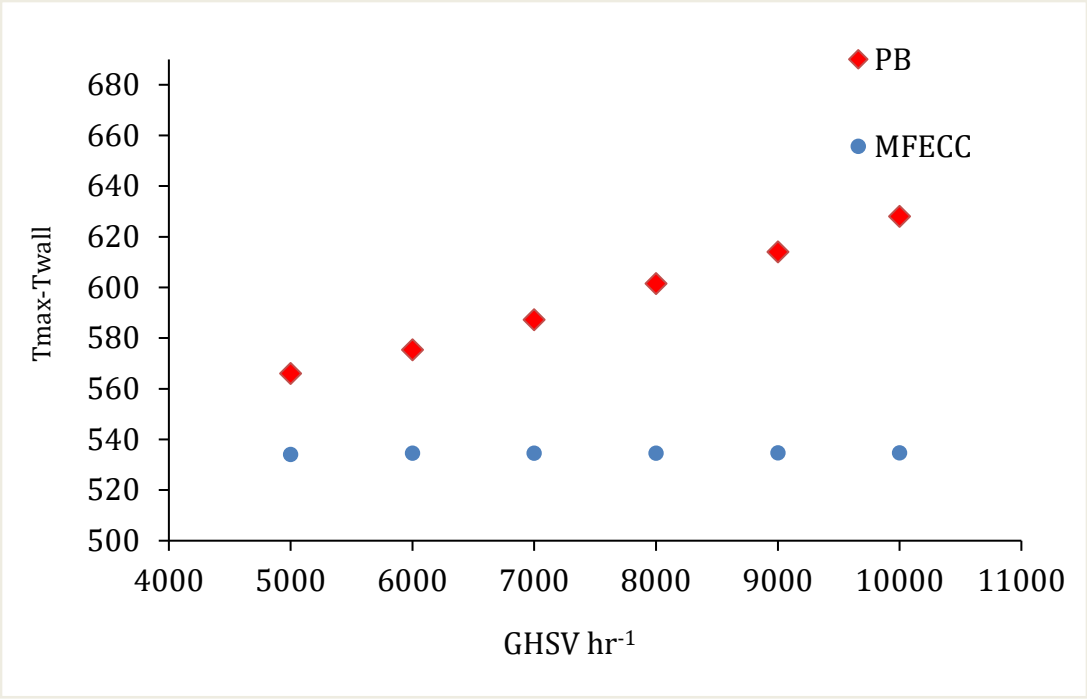

Figure 23: T_{wall}-T_{max} conversion versus GHSV for PB and MFECC bed at 528.15 K, 2 MPa pressure , H_2:CO ratio 2:1

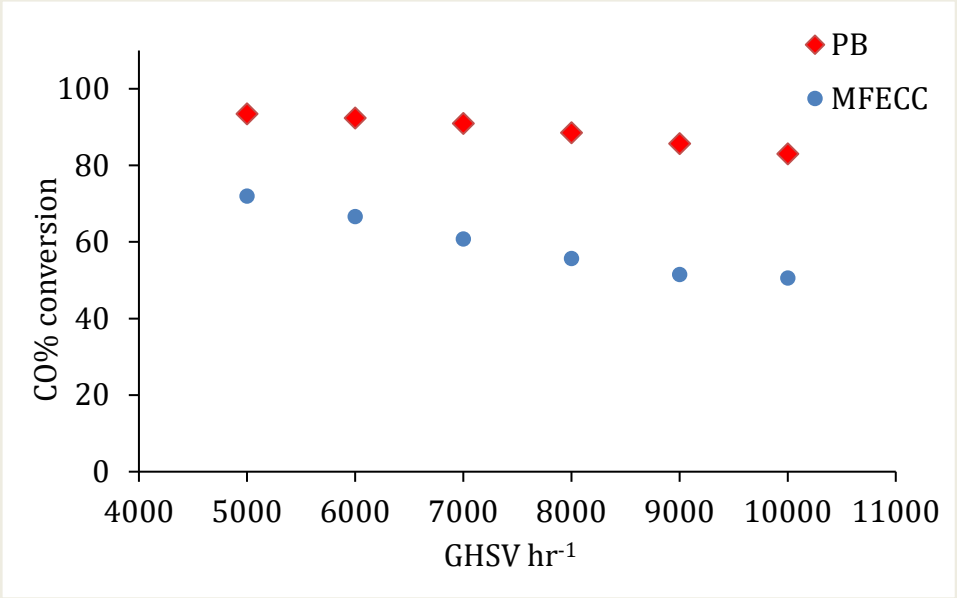

Figure 24: CO% conversion versus GHSV for PB and MFECC bed at 528.15 K, 2 MPa pressure , H_2:CO ratio 2:1

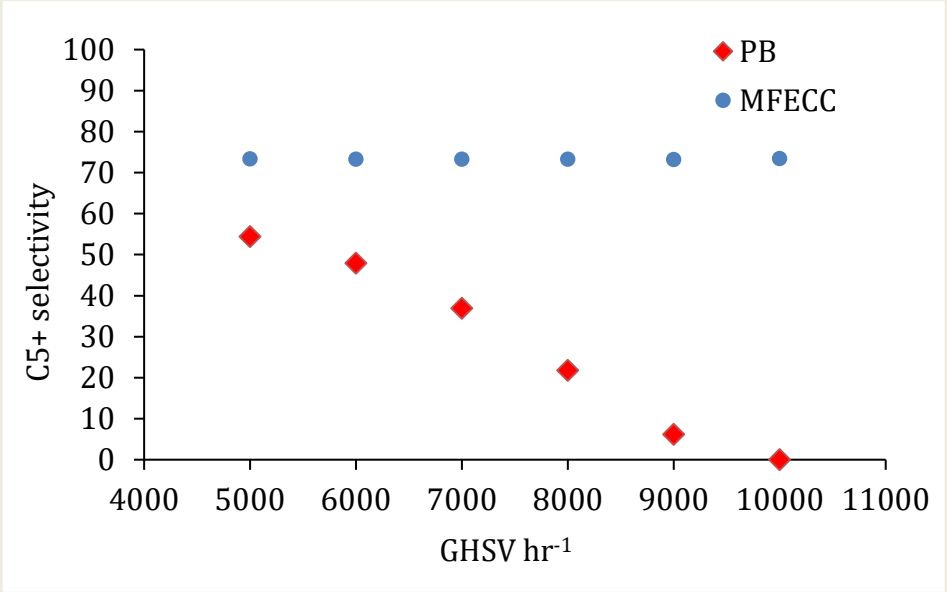

Figure 25: C_{5+} selectivity conversion versus GHSV for PB and MFECC bed at 528.15 K, 2 MPa pressure , H_2:CO ratio 2:1

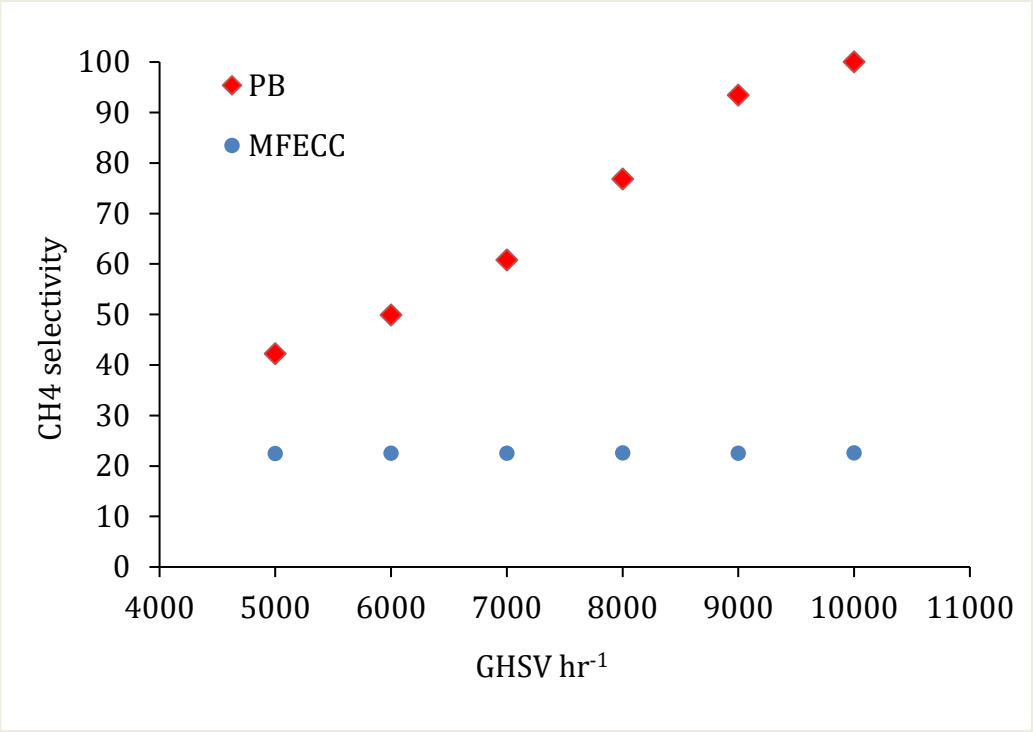

Figure 26: CH_4 selectivity versus GHSV for PB and MFECC bed at 528.15 K, 2 MPa pressure , H_2:CO ratio 2:1

4.1.4. Effect of reactor tube size (scaling up) on temperature distribution for GP-FT operation (PB and MFECC reactor beds)

As mentioned previously, FT is a highly exothermic reaction, thus efficient heat removal is one of the main considerations while designing commercial scale FT reactors[52]. Therefore, the range of tube diameters used in industrial sized PB reactors is 2-5 cm. larger tube sizes provide poor heat management and are more likely to suffer from temperature. This promotes the formation of methane and lowers the selectivity of the desired hydrocarbon products. For industrial applications, it is important to set up the FT in a way that would provide high production of higher weight hydrocarbons (C_{5+}), with low methane selectivity and good temperature control within the reactor bed. The results discussed in the previous sections indicate that the latter can be achieved upon utilization of the novel MFECC structures of high thermal conductivity that allows uniformity in temperature distribution across reactor bed at larger tube diameters.

A number of simulations were performed to study the effect of scaling up the reactor tube diameter up to 4 inch on the thermal behavior of both the PB and MFECC bed. A comparison between the base case model (0.59" ID) and the scaled up model (4" ID) at 20 bar pressure and H_2/CO ratio of (2:1) was done at different inlet temperatures 498.15- 528.15 K. Since changing the tube diameter affects the gas velocity/GHSV, which has a prominent effect on the mass and heat transport properties, the inlet gas flow rate of the was adjusted to maintain a constant GHSV value of 5000 hr^{-1} to provide a fair

comparison between the base case and the scaled up case. Figure 27 shows the maximum temperature rise inside the PB reactor at various inlet temperatures. If all the process parameters are kept constant, increasing the tube diameter from 0.59" to 4" while maintaining constant GHSV (5000 hr^{-1}) results in extreme temperature runways at all inlet temperature conditions, were the hotspot was beyond 200 K. This drastic change in the maximum temperature rise is around 40-50% higher than the base case scenario at 0.59". The extremely high-temperature gradients are mainly due to high radial heat transport resistances at larger tube sizes. As a result of the high temperatures inside the PB reactors, the CO conversion levels at 4" were beyond 90% at all inlet temperatures as shown in Figure 28. The reason behind this is that using larger tube diameters accompanied by the use of higher inlet gas flow rates, enables higher reactor productivity, thus higher CO conversion levels. However, the selectivity toward methane associated with such high-temperature gradients goes up to 100% at all temperature conditions, consequently leading to 0% selectivity toward the desired C_{5+} hydrocarbons as demonstrated in Figure 29.

On the other hand, the MFECC bed provided better temperature control relative to the PB reactor under the same operating conditions when the tube diameter is scaled up to 4 inch. The maximum temperature deviation from the base case (0.59", 498.15- 528.15 K, GHSV 5000 hr^{-1}, H_2/CO 2:1, P_{tot} 20 bar) was below 4K at all inlet temperature conditions as shown in Figure 30. This is due to the high radial effective thermal conductivity of the MFECC bed, which was able to facilitate heat removal even at higher radial resistances in larger tubes. Moreover, when the tube diameter is increased from 0.59" to 4" while keeping

a constant GHSV, the CO conversion goes up by more than 9% for all the simulated temperature conditions as can be seen from Figure 31. The latter indicates a noticeable increase in hydrocarbon productivity per tube is achieved for larger tube diameters. An interesting observation is that for 4" diameter, the CH_4 selectivity only increases by less than 1.4% while the C_{5+} decreases by less than 1.3% compared to the base case scenario as shown in Figure 32. The higher CO conversion accompanied with selectivity control at 4" diameter achieved using the MFECC bed, indicates that higher C_{5+} productivity is obtained relative to the base case.

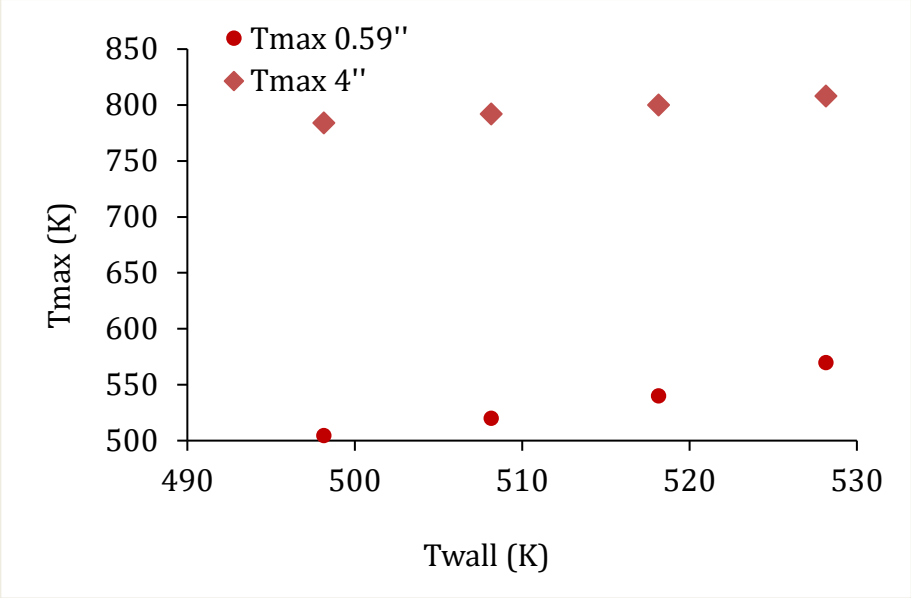

Figure 27: Maximum temperature rise in PB 4" ID (0.1016 m) with base case of 0.59 inch ID (0.0149 m) at 5000 GHSV, H_2/CO 2:1, Ptot = 20 bar

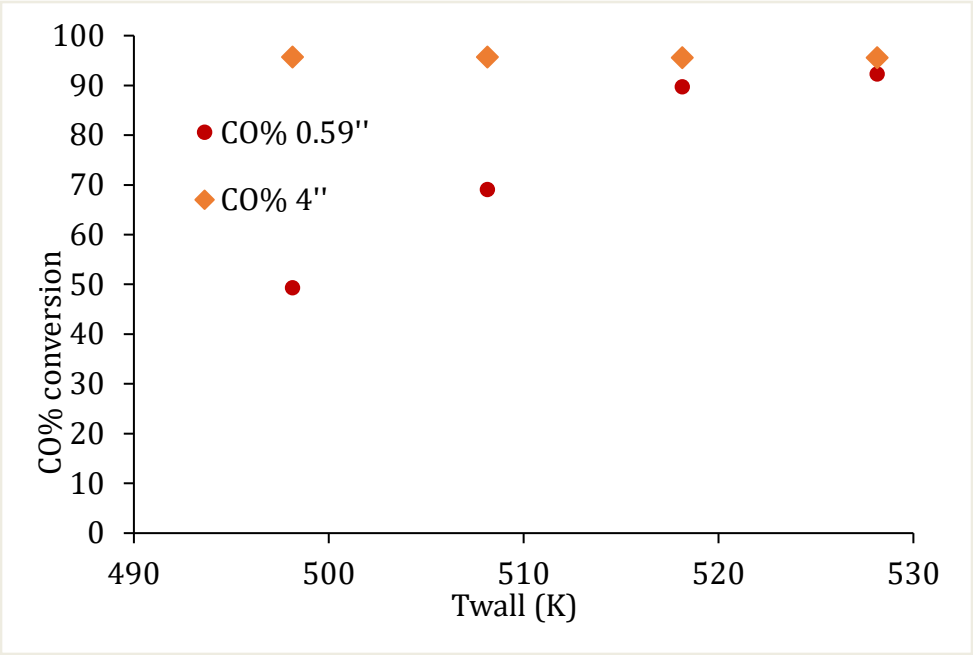

Figure 28: CO% conversion in PB 4” ID (0.1016 m) with base case of 0.59 inch ID (0.0149 m) at 5000 GHSV, H_2/CO 2:1, Ptot = 20 bar

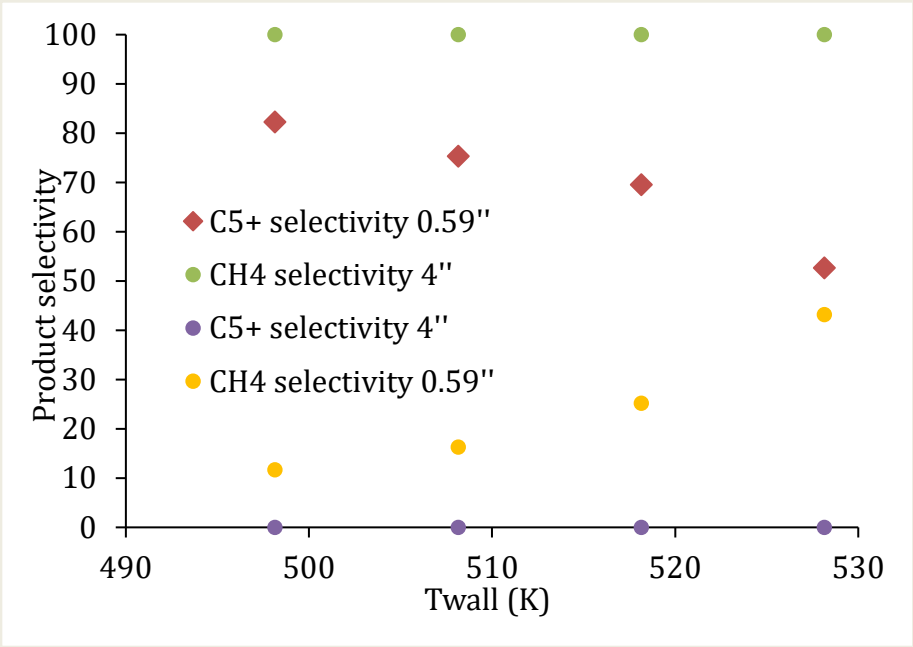

Figure 29: CH_4 and C_{5+} selectivity in PB 4" ID (0.1016 m) with base case of 0.59 inch ID (0.0149 m) at 5000 GHSV, H_2/CO 2:1 , Ptot = 20 bar

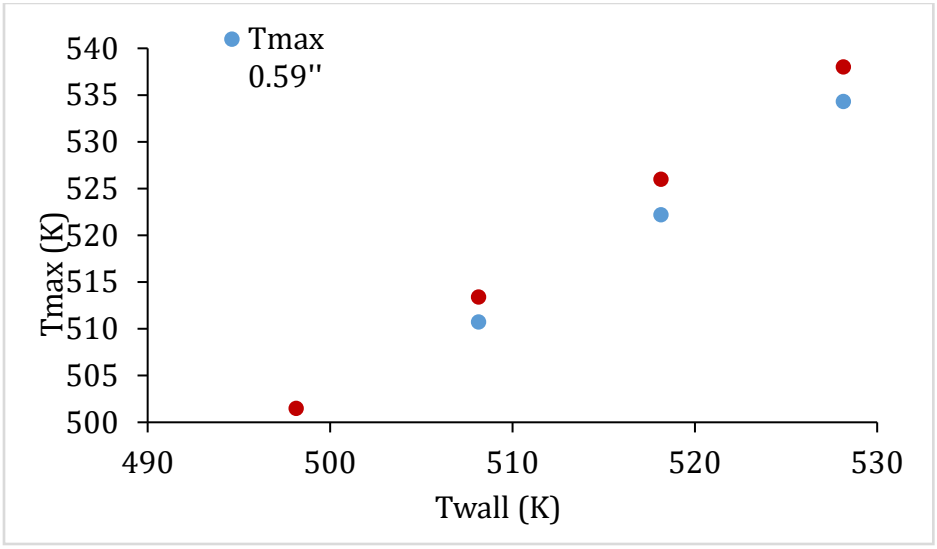

Figure 30: Maximum temperature rise in MFECC 4" ID (0.1016 m) with base case of 0.59 inch ID (0.0149 m) at 5000 GHSV, H_2/CO 2:1, Ptot = 20 bar

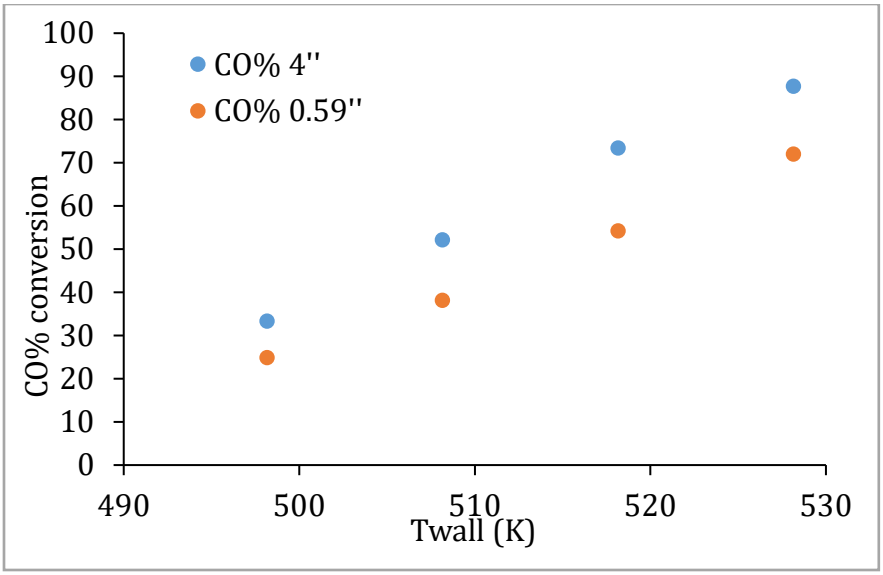

Figure 31: CO% conversion in MFECC 4" ID (0.1016 m) with base case of 0.59 inch ID (0.0149 m) at 5000 GHSV, H_2/CO 2:1, Ptot = 20 bar

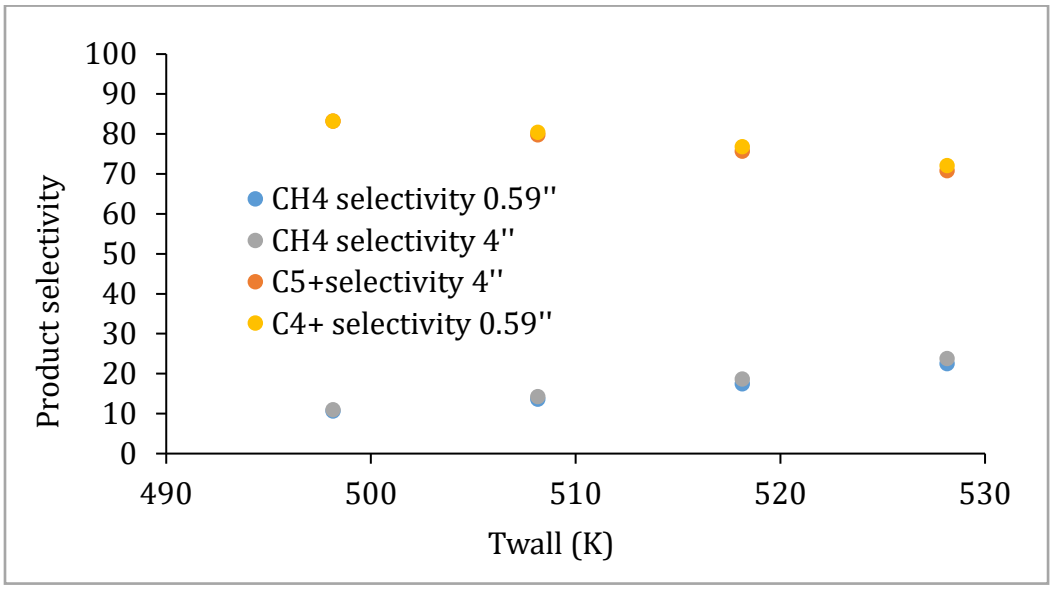

Figure 32: CH_4 and C_{5+} selectivity in MFECC 4" ID (0.1016 m) with base case of 0.59 inch ID (0.0149 m) at 5000 GHSV, H_2/CO 2:1 , Ptot = 20 bar

4.2. Comparison of model prediction with experimental data for SCF-FT[1]

4.2.1. Model validation for PB reactor (SCF-FT and GP-FT operation)

The developed model for the SCF-FT case was validated with experimental data conducted using a high pressure bench scale reactor at Texas A&M University Qatar lab. The overall capacity of the bench scale unit is about 1 L per day of GTL products. The reactor consisted of a single tube with a wall thickness 0.079" mm and 0.688" ID. The total height of the reactor bed was 16" pertaining to; 7.31'" pre-packing zone, 1.377" effective zone (catalytic bed), 7.31" post-packing zone. Two independent experimental campaigns were conducted for SCF-FT mode of operation in which 15% Co/ 0.5%Ru/Al_2O_3 catalyst was used. For each SCF-FT campaign, the reaction was carried out at 80 bar total pressure with 20 bar syngas partial pressure, 2:1 H_2:CO molar feed ratio and, 6 3:1 solvent to syngas molar feed ratio. The reactor was loaded with 1g 6 0.5% Ru promoted 15% Co/ γ -Al_2O_3 supported catalyst, and the bed was diluted with 10g quartz silica to maintain homogeneous distribution of the catalyst in active bed volume of 3.5 cm 8 height. The experimental data was obtained at different inlet and wall temperatures in the range of 9 503-518 K at a constant total pressure of 80 bar. Hexane was used as supercritical solvent with a constant solvent/syngas ratio of 3:1, while the syngas ratio (H2/CO) was also kept constant at 2:1.

[1] Reprinted with permission from "Experimental verification of 2-dimensional computational fluid dynamics modeling of supercritical fluids Fischer Tropsch reactor bed" by Aya E. Abusrafa, et al, 2019. Catalysis Today, Copyright [2019] by Elsevier

The modeling results were validated in terms of CO conversion and the simulation results from this work indicate that the developed model is robust and is capable of predicting the trends in SCF-FT mode of operation as shown in Figure 33. To provide a fair comparison between the GP-FT and SCF-FT performance, the PB model operating under GP-FT conditions was simulated under similar specifications similar to those used in the SCF-FT model including; reactor packing, catalyst loading, reactor dimensions. Further analysis of these results also indicated that the hotspot formation tendency swiftly increases (bed ignition) as the reactor temperature is increased. As can be noted from the maximum temperature (ΔT_{max}) data in Figure 34, the temperature rise for the SCF-FT reactor bed is order of magnitude lower than the temperature of the GP-FT reactor bed operated at same reactor temperature of 518 K. However, at low temperature conditions (498-508 K) of the GP-FT case, the hotspot formation is not evident, and is of the same order of magnitude to that of the SCF-FT case. A close comparison between the conversion levels at these conditions (498-518 K) for both the beds indicate that the SCF-FT provides much lower conversions compared to the GP-FT case for the same reactor temperature. As recognized earlier in a previous publication [84], the rapid bed ignition in the GP-FT increases conversion to almost 100%, however it leads to significant rise in methane selectivity. As methane is one of the components that produces syngas from reforming reaction [16, 145, 146], conversion of syngas to methane is highly undesirable in FT reaction. Due to bed ignition which forms a hotspot, a hysterical change in the catalyst activity generally happens as is evident from considerable conversion loss reported in experimental study by Sheng et al.2013 [110]. These challenges limits GP-FT

processes to be operated at low syngas conversion levels of 50 to 70% (a typical of industrial setup [147]). This challenge of high methane selectivity at high conversion levels in conventional GP-FT reactor beds can, therefore, be mitigated by utilization of the non-conventional SCF-FT based reactor that offers significantly high thermal capacity resulting in temperature homogeneity in the reactor bed.

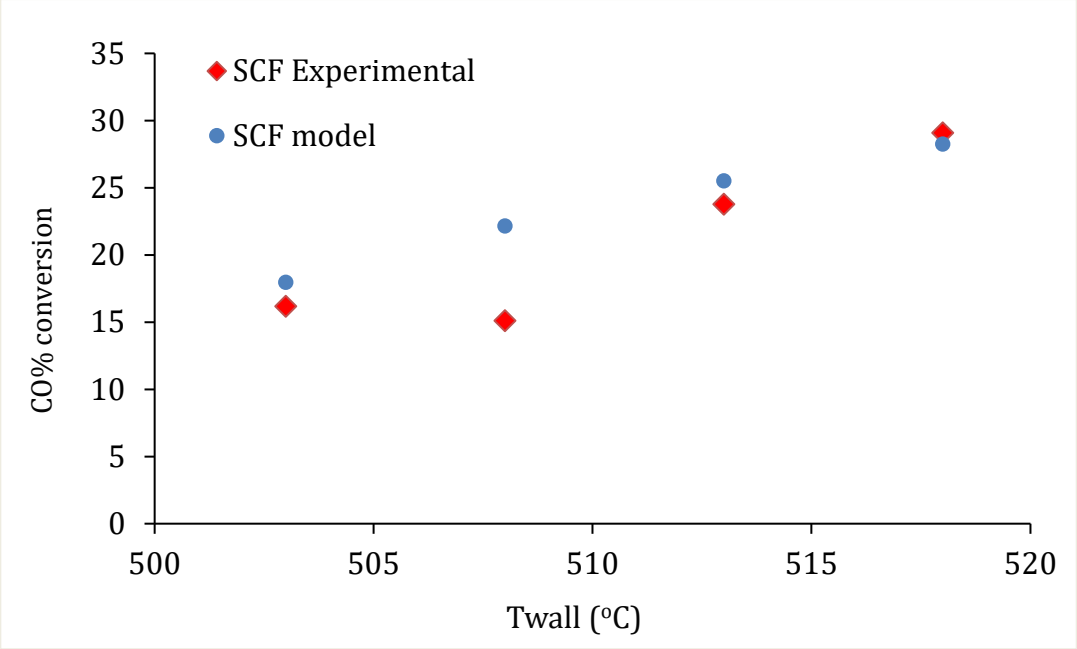

Figure 33: Validation results for SCF-FT bed model in a temperature range of 503-518 K, Solvent: Syngas=3:1, Syngas ratio=2:1, Ptot=80 bar, syngas flow= 138 mL/min (STP) and Solvent flow= 1.14 ml/min

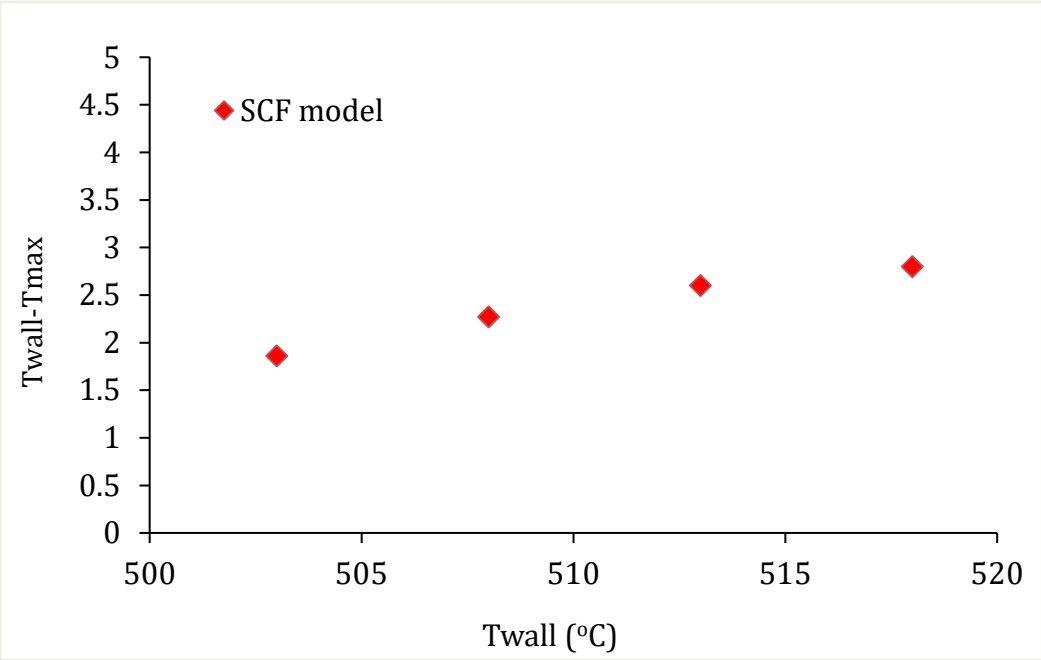

Figure 34: T_{max}-T_{wall} from the model for SCF-FT bed in a temperature range of 503-518 K, Solvent: Syngas=3:1, Syngas ratio=2:1, Ptot=80 bar, syngas flow= 138 mL/min (STP) and Solvent flow= 1.14 ml/min

4.2.2. Comparison of thermal profiles and reactor performance operated in SCF-FT and GP-FT runs

In this section, the validated 2-D reactor bed model was used to compare the thermal profiles of SCF-FT and the GP-FT reactor beds as a function of reactor temperature at constant GHSV of 500 hr^{-1}. The two reactor beds are compared in terms of their axial and radial profiles to better understand the heat transfer effects under different sets of operating conditions. It should be noted that the reported data is at reactor conditions of GHSV value, and not at STP condition. This is due to the fact that the calculation of GHSV at STP condition requires all the reactant species to be in the gaseous state, however at STP condition, n-hexane is at liquid condition, therefore all the reported GHSV values are at reactor condition to avoid any calculation errors due phase changes. More details on the calculations of GHSV are provided in Appendix B.

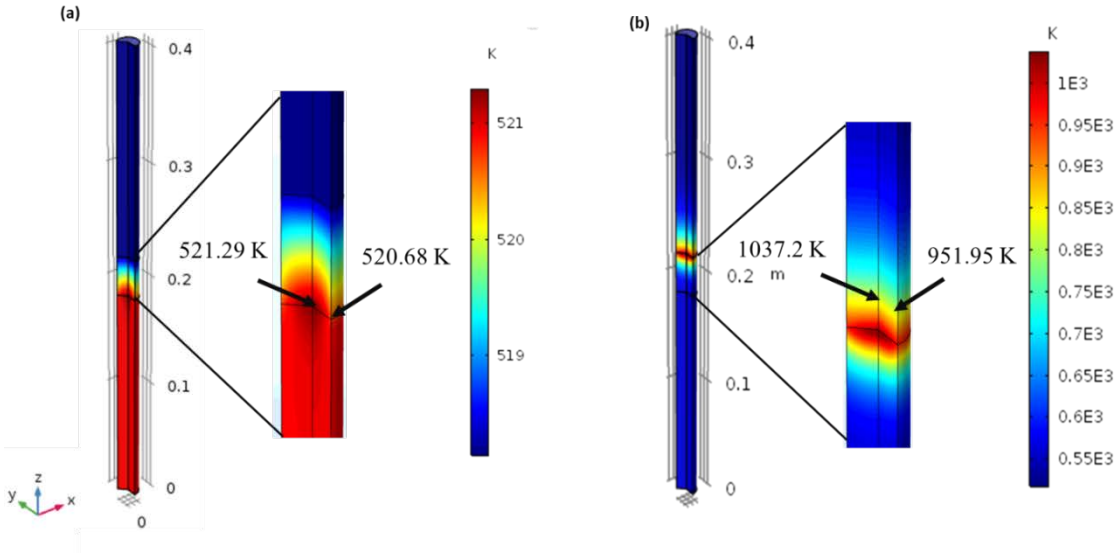

Figure 35:(a) Hot spot in SCF-FT and (b) Hotspot in GP-FT for 0.688" ID (0.0174 m), 500 GHSV calculated at reactor conditions, H_2/CO 2:1 , Solvent/syngas 3:1, Inlet temperature: 518.15 K. Ptot: 80 bar for SCF-FT, Ptot: 20 bar for GP-FT

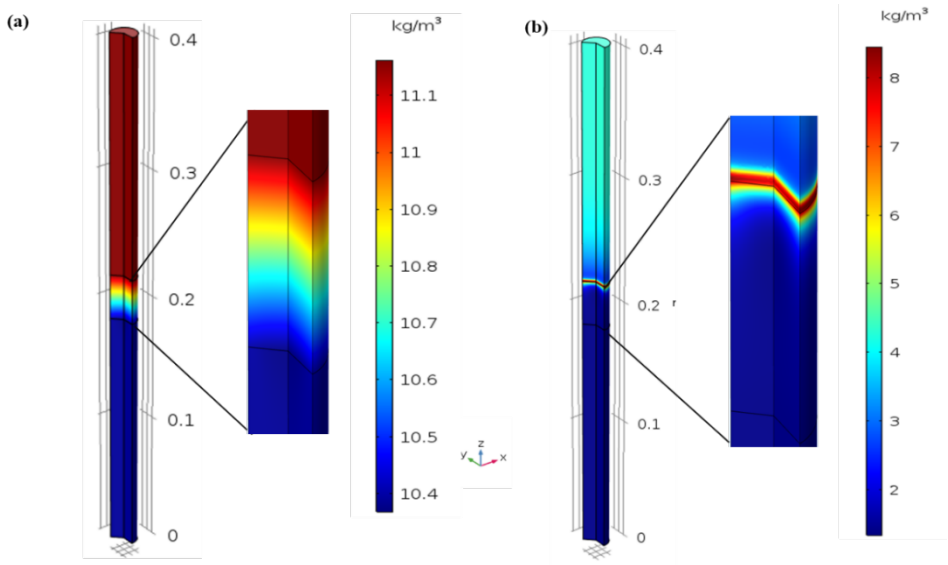

Figure 36:(a) CO mass concentration profile in SCF-FT and (b) CO mass concentration in GP-FT for 0.688" ID (0.0174 m), 500 GHSV calculated at reactor conditions, H_2/CO 2:1, Solvent/syngas 3:1, Inlet temperature: 518.15 K. Ptot: 80 bar for SCF-FT, Ptot: 20 bar for GP-FT

It has been observed in the previous literature studies [68, 76, 80, 81, 148, 149], that SCF-FT mode of operation suppresses both methane and carbon dioxide selectivity relative to the GP-FT due to its ability to maintain homogeneity in both; temperature, as well as syngas concentration across the reactor bed. From our 2-D modeling study, we observe a homogeneous distribution of both, temperature as well as syngas concentration in the SCF-FT reactor bed, which is not observed in the conventional GP-FT reactor bed as shown in Figure 35 and 36. In both simulations, the bed diameter was kept as 0.688" ID for GHSV of 500 h^{-1}, while the total pressure of the SCF-FT run is considered 80 bar

and the GP-FT run is 20 bar. It can be observed from Figure 35, there is a smooth temperature transition in the SCF-FT reactor as temperature progresses through the reaction zone, on the other hand an abrupt temperature transition is observed in the GP-FT reactor bed. Additionally, the maximum temperature rise in the case of SCF-FT run was found to be only around 3 K higher than the inlet temperature along the axial dimension, while the GP-FT reactor bed suffers from extreme temperature rise of approximately 500 K as it reaches the reaction zone. While comparing radial temperature gradients, almost 50K temperature rise was observed in GP-FT case in contrast to only 1 K rise in SCF-FT. Superior temperature homogeneity in case of SCF-FT in both axial and radial dimension, therefore, demonstrates the ability of supercritical media in facilitating effective heat removal compared to GP-FT case. It should be recognized that the CO conversions are functions of temperature, and due to abrupt increase in reactor temperatures, CO conversions as high as 100% could be achieved. However, most of the conversion goes toward methane formation as it is favorable at high temperature conditions [150]. Owing to controlled temperature rise, and uniformity in fluid density (Figure 36a) throughout the reaction zone, a moderate %CO conversion (~30%) is achieved in the SCF-FT runs while suppressing methane selectivity. On the other hand, the fluid density in the GP-FT reactor bed (Figure 36b) is shown to vary abruptly along the reaction zone due to hot spot formation as shown in Figure 35b. Similar results were reported in previous studies by Robert and his coworkers [70, 80, 151]. In their study on SCF-FT using different catalyst bed, it was shown that dense supercritical media facilitated axial thermal uniformity resulting in significant suppression in hot spot

formation. Similarly, Yan et al. 1998 [81] conducted a study on the SCF-FT reaction media to investigate the syngas concentration profile across reactor bed to identify the role of diffusional resistances on methane selectivity. They observed that diffusional resistances in the gas phase operation resulted in higher syngas ratio in catalyst pellet and consequently led to increase in methane selectivity.

Figures 37 and 38 depict the centerline temperature profiles and hot spots of the GP-FT and SCF-FT reactor beds simulated at reactor temperatures in the range of 508 K-528 K. It can be observed that the magnitude of the hot spot under all conditions stated above in case of GP-FT is almost 500 K higher than its inlet temperatures, while only a mild temperature rise of ~3-5 K is observed in SCF-FT. On a similar note, it is observed in Figure 39 that an increase in the GHSV leads to a decrease in % CO in SCF-FT, while an opposite trend is observed in case of GP-FT. It should be noted that the conversion achieved in SCF-FT runs is almost 10-30% to that of GP-FT. This is because of the fact that hotspot formation in GP-FT (shown in Figure 40) leads to high CO conversion and predominance of methane formation, which is undesirable for FT reaction.

Although supercritical media provides an exceptional reaction control compared to a conventional GP-FT reaction, extremely low yields are obtained from SCF-FT reaction discouraging its industrial implementation. This is due to the fact that almost 80-90 mass percent of the reaction media in SCF-FT reaction comprises of supercritical solvent. A separate techno-economic study conducted in a previous publication addresses this challenge [152]. In their study, an alternative solvent separation sequence in

downstream of the FT reactor utilizing relatively less energy for separation is reported thereby making SCF-FT a competitive option for producing GTL products.

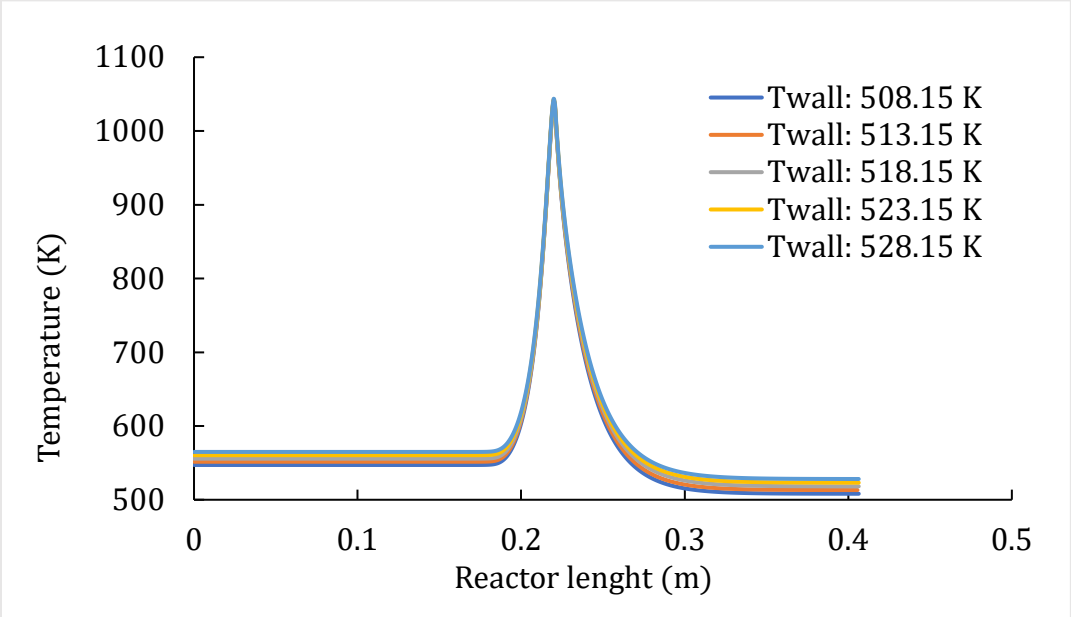

Figure 37: Centerline temperature in GP-FT, Ptot=20 bar, 0.688 inch ID (0.0174 m) at constant flow of 500 GHSV calculated at reactor conditions, H2/CO 2:1.

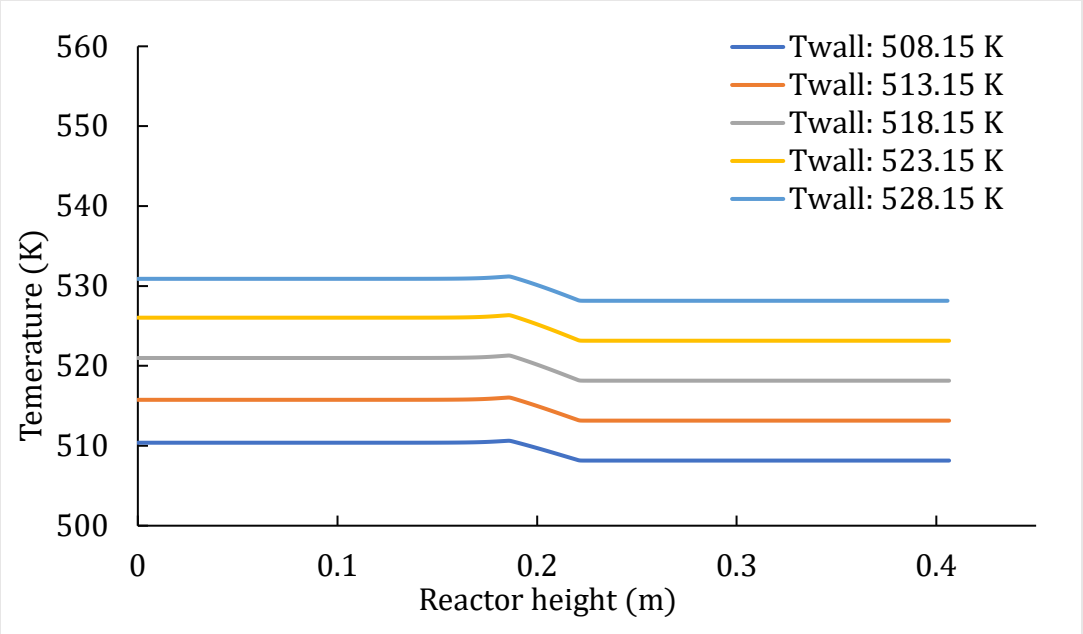

Figure 38: Centerline temperature in SCF-FT, Solvent/syngas 3:1, Ptot = 80 bar, 0.688 inch ID (0.0174 m) at constant flow of 500 GHSV calculated at reactor conditions, H2/CO 2:1.

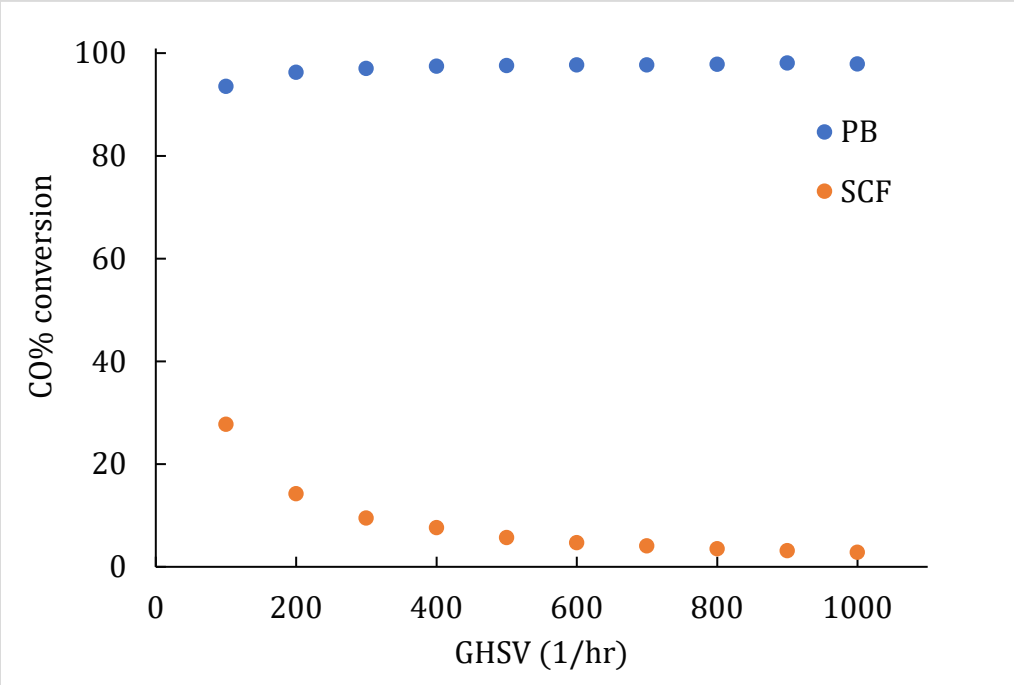

Figure 39: %CO conversion in SCF-FT and GP-FT versus GHSV for 0.688 inch ID (0.0174 m), GHSV range: 100-1000 GHSV calculated at reactor conditions, H2/CO= 2:1, Solvent/syngas 3:1, Inlet temperature 518.15 K

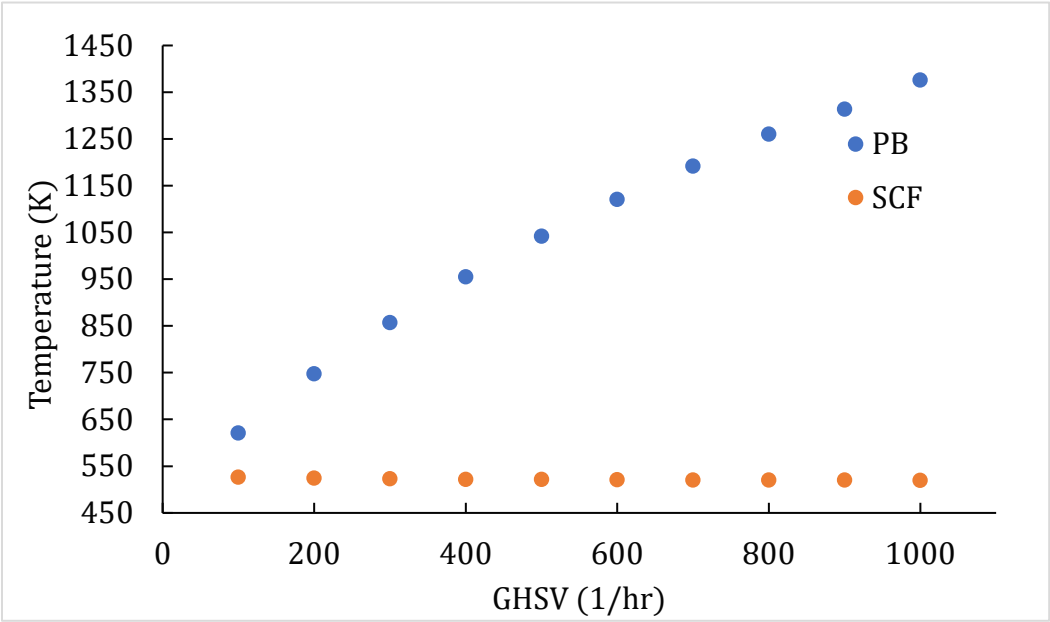

Figure 40: Maximum Temperature rise in SCF-FT and GP-FT versus GHSV for 0.688 inch ID (0.0174 m), GHSV range: 100-1000 GHSV calculated at reactor conditions, H2/CO= 2:1, Solvent/syngas 3:1, Inlet temperature 518.15 K, Ptot: 20 bar for GP-FT, Ptot: 80 bar for SCF-FT.

4.2.3. Application of SCF-FT for process intensification

In the previous section, a comparison between the centerline temperature profiles of the base case (of 0.688” ID) at variable operational temperatures in the range of 508-528 K was provided. In the present section, a number of simulations runs for both SCF-FT and GP-FT reactor beds were conducted, where the tube diameter was scaled up from 0.688 inch to 4 inch. As the procedure for reactor scale-up is computationally expensive [84], this study was limited only to a 4” diameter to establish an understanding of the role of SCF media in thermal management of large size reactor beds. For all the aforementioned cases, the effect of variation in GHSV and operational temperatures were recorded in terms of % CO conversion and the hotspot temperatures as shown in Figure 38 and Figure 39. For all the cases considered, the GHSV was varied in the range of 100-300 h^{-1}, while the operational temperatures were varied from 508-518 K. For the SCF-FT case of 4” ID, it was observed that only a slight increase in % CO conversion is achieved with increase in the reactor temperature (wall and inlet temperature). As 80-90 mass percent of the reaction mixture comprises of supercritical solvent n-hexane and due to strong homogeneity in fluid density, the effect of temperature rise on %CO conversion is not very pronounced. Additionally, the variation in GHSV from 100 to 300 h^{-1} results in decrease in % CO conversion (Figure 38a) and the maximum temperature rise in the reactor as shown in Figure 38b. It can be seen that the rate of increase in %CO conversion and maximum temperature rise in the reactor with respect to GHSV for a same reactor diameter also remained constant over all the three temperatures considered in this study. This indicates a linear relationship of residence time with the maximum temperature of

the reactor and the %CO conversion. Also, the increase in the tube diameter from 0.688” to 4” at constant GHSV does not result in a significant increase in the %CO conversion levels, which could be attributed to excellent concentration homogeneity obtained in SCF-FT reactor bed.

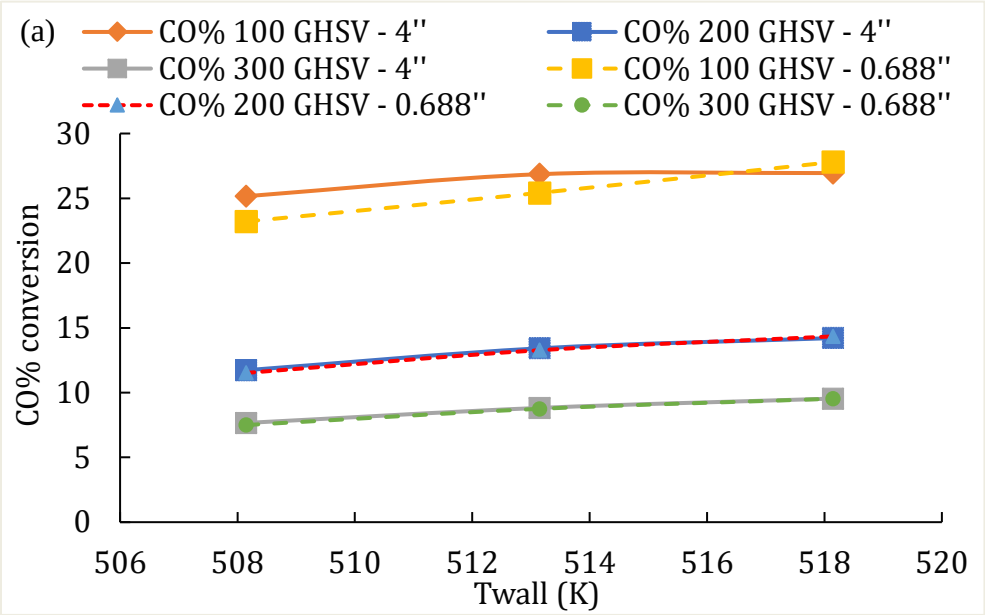

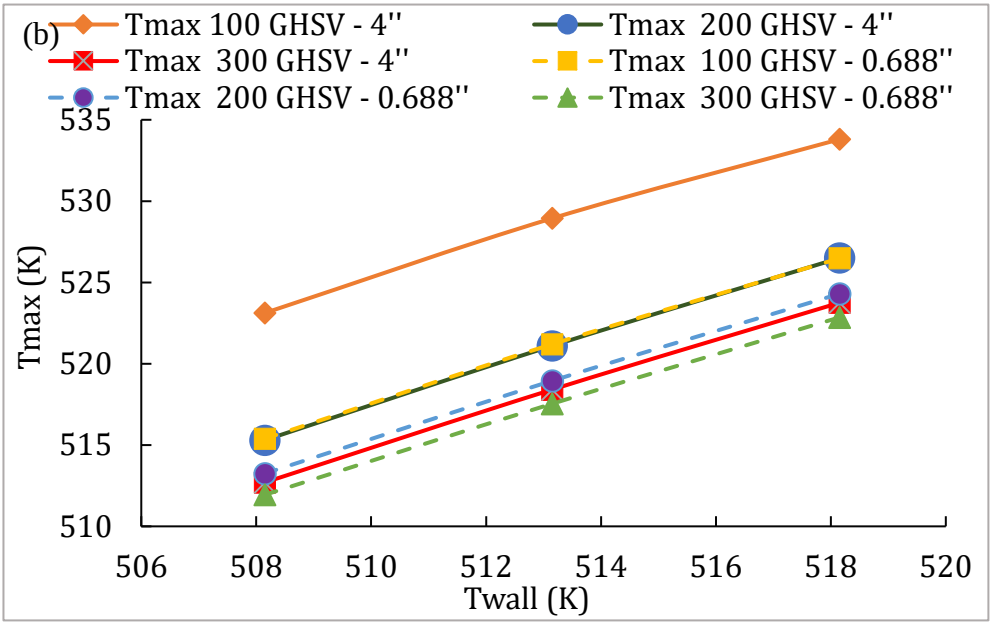

Figure 41: Comparison of (a) %CO conversion (b) Maximum temperature rise in SCF-FT 4" ID (0.1016 m) with base case of 0.688 inch ID (0.0174 m) at 100-300 GHSV calculated at reactor conditions, H_2/CO 2:1 , Solvent/syngas 3:1, Ptot = 80 bar

In contrast to the SCF-FT case, opposite trends were observed in GP-FT case as shown in Figure 39a and 39b. As discussed in the previous section, hot spot formation occurs in GP-FT case under all temperature conditions for the base case study of 0.688" ID (Figure 5). A similar observation could be made for 4" ID reactor as shown in Figure 39b, in that; for all the wall temperatures the hot spot temperature rise are beyond 500 K. As a consequence, to the hotspot formation, % CO conversion beyond 90% is achieved that mostly leads to higher methane selectivity. Due to this effect, any increase in the reactor temperature does not affect the % CO conversion to a greater extent compared to that of SCF-FT case. With increase in the GHSV (Figure 8 b), the maximum temperature achieved in the GP-FT case showed an increasing trend, however a decreasing trend is shown in case of SCF-FT. In addition to this, a comparison of hot spot formation between the SCF-FT and the GP-FT case at 4"ID reveals orders of magnitude difference between the hot spot formation tendencies (maximum 15 K temperature rise in SCF-FT Vs. 800 K in GP-FT). Hot spot formations of large magnitude in the GP-FT as demonstrated in this work indicates the inability of the current industrial infrastructure to operate FT reaction in larger diameter tubes despite their numerous benefits. SCF-FT process, on the other hand, provides an alternative solution in controlling hot spot formation for a larger diameter reactor which reduces temperature impact on hydrocarbon selectivity (reduction in methane selectivity) while at the same time opens a new perspective towards radial reactor scale-up.

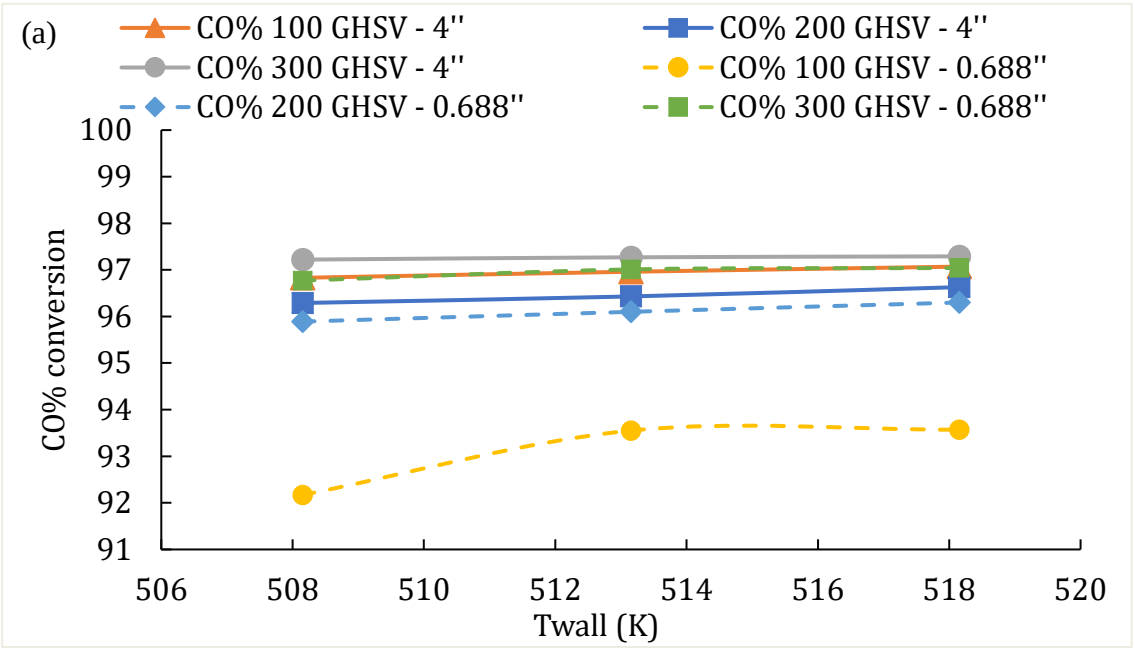

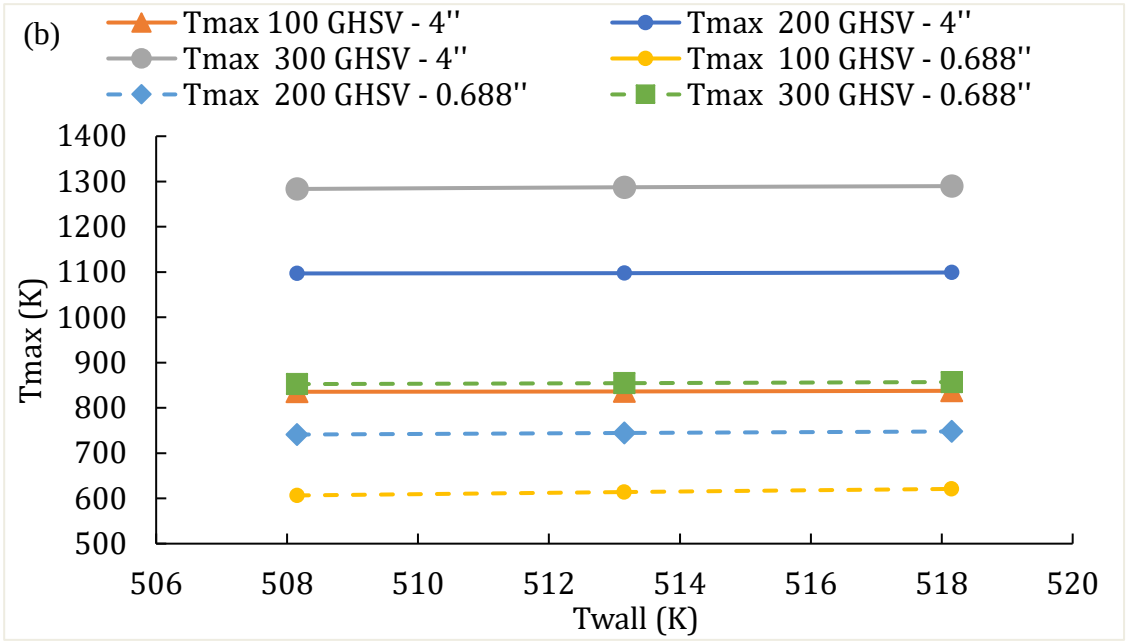

Figure 42: Comparison of (a) %CO conversion (b) Maximum temperature rise in SCF-FT 4" ID (0.1016 m) with base case of 0.688 inch ID (0.0174 m) at 100-300 GHSV calculated at reactor conditions, H2/CO 2:1 , Solvent/syngas 3:1, Ptot = 80 bar

5. CONCLUSIONS

The development of novel microfibrous entrapped cobalt catalyst structure (MFECC), made of high thermal conductive metals, and the usage of supercritical fluids (SCF), and has stemmed from extensive research to improve the limitations associated with FT reactor technologies. From the beginning of Fischer Tropsch discovery until today different reactor technologies have been proposed, however, Multitubular/packed bed (PB) reactors are most often employed in commercial applications. Due to the highly exothermic nature of FT synthesis, poor heat removal is considered as one of the main drawbacks associated with using PB reactors, which limits its scalability to higher tube diameters (>5 cm).

While utilizing SCF as a reaction media provides better heat management, longer catalyst lifetimes, and selectivity control of the hydrocarbon product distribution. While, using MFECC structures, with enhanced heat transfer properties in the FT process, has proven to aid in eliminating hotpots that typically occur in PB reactors. However, the implementation of the aforementioned technologies has been investigated at laboratory scale. However, before the commercialization of non-conventional FT technologies, performance analysis under conditions that might not be achievable at an experimental level is necessary. Most importantly is the radial scale-up to industrial size reactors to study the hydrodynamics and reactor performance under wide range of conditions. Therefore, a 2-D Computational Fluid Dynamics (CFD) model of an FT reactor was developed in COMSOL® Multiphysics v5.3a for three systems; non-conventional

MFECC bed under GP-FT conditions, conventional PB under gas phase conditions (GP-FT) and non-conventional PB in SCF-FT media. The possibility of scaling-up the reactor diameter above the typical industrial diameter > 1.5 inch (up to 4" ID) was studied as an initial step towards the process intensification of the FT technology.

First, the model validity of the MFECC bed and PB was tested with experimental data from Auburn University. The simulation results for both the MFECC bed and PB was found to be in good agreement with the experimental predictions for CO conversion, maximum temperature deviation from the wall temperature, CH_4 selectivity, and C_{5+} selectivity. A comparison of the thermal profiles was done at 528.15 K, 20 bar pressure, H_2/CO ratio of 2:1 and a constant GHSV 5000 hr^{-1}. The axial temperature deviation for the PB reactor as predicted from the model is around 43K and the radial temperature gradient is around 1.15 K. On the other hand, the maximum axial temperature deviation in the MFECC bed was only 10K and the radial temperature gradient was 0.013 K. The hotspot formed in the PB at 528.15 K resulted in around 92% CO conversion as per experimental results, 48.4% CH_4 selectivity and 52.68% C_{5+} selectivity. The MFECC was able to provide near isothermal operation (72% CO conversion) which resulted in higher selectivity toward higher weight hydrocarbon products C_{5+} (72.2%) and lower CH_4 selectivity (72.2%). Further analysis included studying the effect of the inlet gas flow rate/GHSV on the heat generation and removal for the MFECC bed and PB was investigated at 528.15 K, 20 bar pressure, H_2/CO ratio of 2:1 and a constant GHSV 5000 hr. It was found the increasing the GHSV results in higher temperate gradients in the PB reactors, while almost no effect was observed in the case of MFECC. The CH_4 selectivity

in the PB reactor went up to 100% at 10000 hr^{-1} GHSV, which resulted in 0% production of the C_{5+} hydrocarbons. On the hand other, the MFECC bed maintained a lower CH_4 selectivity (22.58%) and a higher C_{5+} selectivity (73.42%). Therefore, the MFECC bed was provided a higher total productivity of the desired hydrocarbons per catalyst mass compared to the PB.

A comparison between the base case model (0.59" ID) and the scaled up model (4" ID) revealed that the high radial effective thermal conductivity of the MFECC bed was able to provide efficient heat removal (near isothermal operation) even at higher radial distances in larger tubes. On contrast, the PB suffered from extremely temperatures runways which led to (100% CH_4 selectivity and 0% C_{5+} selectivity).

For the SCF-FT case, the model was validated by experimental data collected at Texas A&M University lab under a variety of FT reaction conditions and was further scaled-up to 4” ID for both SCF-FT and GP-FT reactor beds. The impact of reaction media in controlling the hot spot formation for 4” ID was investigated and correlated with the catalyst activity measured by the CO conversion over a wide range of GHSVs and wall temperatures. The simulation results showed that the SCF-FT demonstrate exceptional reduction in hotspot formation with a maximum radial bed temperature variation <15 K for a 4” ID reactor bed as opposed to 800 K in an equivalent GP-FT reactor bed. Thermal stability in the SCF-FT mode of operation supports previous experimental evidence that claimed improved catalyst stability, hydrocarbon selectivity and reactor control under scaled-up conditions. These results provide first confirmation for process intensification in which up to 16-fold reduction in the number of tubes required to achieve a targeted

compared to a conventional 1” ID reactor bed. Moreover, owing to more efficient temperature control, the productivity of the heavy hydrocarbon cuts could be achieved, thus increasing the probability of the plant. This could impose significant savings in capital and operating costs associated with existing FT reactor bed technologies warranting more investigations.

The development of a robust 2-D pseudo-homogenous model constitutes the first step toward the development of a more complex and comprehensive model. The suggestions listed below are recommended for future work:

- Extend the current model to the micro-scale level to account for the mass diffusion limitations within the catalyst pellet (accounting for the existence of concentration and temperature gradients within inside the catalyst).
- Utilize heterogeneous 3-Dimensional model correlations to account for the presence of the liquid phase during the FT reaction.
- Develop a transient model to observe the time-varying dynamic behavior during the FT reaction.
- To extend the modeling framework to a very important part within the GTL process which is the reforming section. This will mainly include a time-dependent study for the deactivation of the spherical catalyst particles in non-conventional dry reforming of methane (DRM) process. This study is very important to provide future insight to overcome the limitation associated with DRM technology.

REFERENCES

1. Khalilpour, R. and I. Karimi, *Evaluation of utilization alternatives for stranded natural gas.* Energy, 2012. **40**(1): p. 317-328.
2. Dong, L., et al., *GTL or LNG: which is the best way to monetize "stranded" natural gas?* Petroleum Science, 2008. **5**(4): p. 388-394.
3. Elbashir, N.O., et al., *Natural Gas Processing from Midstream to Downstream*2018: Wiley.
4. *IEA, World Energy Outlook. Are we entering a golden age of gas?* . International Energy Agency 2011.
5. EIA, *World energy demand and economic outlook EIA's handling of non-U.S. policies in the International Energy Outlook'*, 2016, Energy Information Administration: US.
6. Schulz, H., *Short history and present trends of Fischer–Tropsch synthesis.* Applied Catalysis A: General, 1999. **186**(1-2): p. 3-12.
7. Elbashir, N.O. and F.T. Eljack. *A Method to Design an Advanced Gas-to-Liquid Technology Reactor for Fischer-Tropsch Synthesis*. in *Proceedings of the 2nd Annual Gas Processing Symposium*. 2010. Elsevier.
8. Moazami, N., et al., *Parametric Study and Multiobjective Optimization of Fixed-Bed Fischer–Tropsch (FT) Reactor: The Improvement of FT Synthesis Product Formation and Synthetic Conversion.* Industrial & Engineering Chemistry Research, 2017. **56**(34): p. 9446-9466.
9. Méndez, C.I., J. Ancheyta, and F. Trejo, *Modeling of Catalytic Fixed-Bed Reactors for Fuels Production by Fischer–Tropsch Synthesis.* Energy & Fuels, 2017. **31**(12): p. 13011-13042.
10. Yang, J.H., et al., *Mass transfer limitations on fixed-bed reactor for Fischer–Tropsch synthesis.* Fuel Processing Technology, 2010. **91**(3): p. 285-289.
11. Shin, D.-Y., et al., *CFD modeling of a modular reactor for the Fischer–Tropsch synthesis: Effectiveness of a micro-scale cross-current cooling channel.* Fuel, 2015. **158**: p. 826-834.
12. Guettel, R., U. Kunz, and T. Turek, *Reactors for Fischer-Tropsch Synthesis.* Chemical Engineering & Technology, 2008. **31**(5): p. 746-754.
13. Todić, B., et al., *Opportunities for intensification of Fischer–Tropsch synthesis through reduced formation of methane over cobalt catalysts in microreactors.* Catalysis Science & Technology, 2015. **5**(3): p. 1400-1411.
14. Ross, J.R.H., et al., *The catalytic conversion of natural gas to useful products.* Catalysis Today, 1996. **30**(1): p. 193-199.
15. de Klerk, A., *Fischer–Tropsch refining: technology selection to match molecules.* Green Chemistry, 2008. **10**(12): p. 1249-1279.
16. Challiwala, M.S., et al., *A combined thermo-kinetic analysis of various methane reforming technologies: Comparison with dry reforming.* Journal of CO2 Utilization, 2017. **17**(Supplement C): p. 99-111.
17. Djaidja, A., et al., *Characterization and activity in dry reforming of methane on NiMg/Al and Ni/MgO catalysts.* Catalysis Today, 2006. **113**(3-4): p. 194-200.

18. Nagaoka, K., et al., *Carbon deposition during carbon dioxide reforming of methane—comparison between Pt/Al2O3 and Pt/ZrO2.* Journal of Catalysis, 2001. **197**(1): p. 34-42.
19. Masters, C., *The Fischer-Tropsch Reaction,* in *Advances in Organometallic Chemistry*, F.G.A. Stone and R. West, Editors. 1979, Academic Press. p. 61-103.
20. Storch, H.H., *The Fischer-Tropsch and Related Processes for Synthesis of Hydrocarbons by Hydrogenation of Carbon Monoxide**Published by permission of the Director, Bureau of Mines, U.S. Department of the Interior, Washington, D.C*, in *Advances in Catalysis*, W.G. Frankenburg, V.I. Komarewsky, and E.K. Rideal, Editors. 1948, Academic Press. p. 115-156.
21. Anderson, R.B., H. Kölbel, and M. Ralek, *The fischer-tropsch synthesis*. Vol. 16. 1984: Academic Press New York.
22. Satterfield, C.N., G.A. Huff Jr, and J.P. Longwell, *Product distribution from iron catalysts in Fischer-Tropsch slurry reactors.* Industrial & Engineering Chemistry Process Design and Development, 1982. **21**(3): p. 465-470.
23. Stranges, A.N., *A history of the fischer-tropsch synthesis in Germany 1926-45.* Studies in surface science and catalysis, 2007: p. 1-27.
24. Madon, R.J., S.C. Reyes, and E. Iglesia, *Primary and secondary reaction pathways in ruthenium-catalyzed hydrocarbon synthesis.* The Journal of Physical Chemistry, 1991. **95**(20): p. 7795-7804.
25. Dictor, R.A. and A.T. Bell, *An explanation for deviations of Fischer-Tropsch products from a Schulz-Flory distribution.* Industrial & Engineering Chemistry Process Design and Development, 1983. **22**(4): p. 678-681.
26. Dry, M.E., *The fischer–tropsch process: 1950–2000.* Catalysis Today, 2002. **71**(3-4): p. 227-241.
27. Luque, R., et al., *Design and development of catalysts for Biomass-To-Liquid-Fischer–Tropsch (BTL-FT) processes for biofuels production.* Energy & Environmental Science, 2012. **5**(1): p. 5186-5202.
28. Atwood, H.E. and C.O. Bennett, *Kinetics of the Fischer-Tropsch reaction over iron.* Industrial & Engineering Chemistry Process Design and Development, 1979. **18**(1): p. 163-170.
29. Wood, D.A., C. Nwaoha, and B.F. Towler, *Gas-to-liquids (GTL): A review of an industry offering several routes for monetizing natural gas.* Journal of Natural Gas Science and Engineering, 2012. **9**: p. 196-208.
30. Dry, M.E., *High quality diesel via the Fischer–Tropsch process–a review.* Journal of Chemical Technology and Biotechnology, 2002. **77**(1): p. 43-50.
31. Dry, M., T. Shingles, and L. Boshoff, *Rate of the Fischer-Tropsch reaction over iron catalysts.* Journal of Catalysis, 1972. **25**(1): p. 99-104.
32. Bartholomew, C.H. and R.J. Farrauto, *Fundamentals of industrial catalytic processes*2011: John Wiley & Sons.
33. Jager, B. and R. Espinoza, *Advances in low temperature Fischer-Tropsch synthesis.* Catalysis Today, 1995. **23**(1): p. 17-28.

34. Velasco, J.A., et al., *Gas to liquids: A technology for natural gas industrialization in Bolivia.* Journal of Natural Gas Science and Engineering, 2010. **2**(5): p. 222-228.
35. Todic, B., et al., *Effects of process and design parameters on heat management in fixed bed Fischer-Tropsch synthesis reactor.* Korean Journal of Chemical Engineering, 2018. **35**(4): p. 875-889.
36. Brady III, R.C. and R. Pettit, *Mechanism of the Fischer-Tropsch reaction. The chain propagation step.* Journal of the American Chemical Society, 1981. **103**(5): p. 1287-1289.
37. Anderson, R., R. Friedel, and H. Storch, *Fischer-Tropsch Reaction Mechanism Involving Stepwise Growth of Carbon Chain.* The Journal of Chemical Physics, 1951. **19**(3): p. 313-319.
38. Todic, B., et al., *Kinetic Model of Fischer–Tropsch Synthesis in a Slurry Reactor on Co–Re/Al2O3 Catalyst.* Industrial & Engineering Chemistry Research, 2013. **52**(2): p. 669-679.
39. Saeidi, S., et al., *Recent advances in reactors for low-temperature Fischer-Tropsch synthesis: process intensification perspective*, in *Reviews in Chemical Engineering*2015. p. 209.
40. Kuipers, E.W., I.H. Vinkenburg, and H. Oosterbeek, *Chain Length Dependence of α-Olefin Readsorption in Fischer-Tropsch Synthesis.* Journal of Catalysis, 1995. **152**(1): p. 137-146.
41. Van Der Laan, G.P. and A.A.C.M. Beenackers, *Kinetics and Selectivity of the Fischer–Tropsch Synthesis: A Literature Review.* Catalysis Reviews, 1999. **41**(3-4): p. 255-318.
42. Iglesia, E., et al., *Selectivity Control and Catalyst Design in the Fischer-Tropsch Synthesis: Sites, Pellets, and Reactors*, in *Advances in Catalysis*, D.D. Eley, H. Pines, and P.B. Weisz, Editors. 1993, Academic Press. p. 221-302.
43. Iglesia, E., S.C. Reyes, and R.J. Madon, *Transport-enhanced α-olefin readsorption pathways in Ru-catalyzed hydrocarbon synthesis.* Journal of Catalysis, 1991. **129**(1): p. 238-256.
44. Schulz, H. and M. Claeys, *Kinetic modelling of Fischer–Tropsch product distributions.* Applied Catalysis A: General, 1999. **186**(1): p. 91-107.
45. van der Laan, G.P. and A.A.C.M. Beenackers, *Hydrocarbon Selectivity Model for the Gas−Solid Fischer−Tropsch Synthesis on Precipitated Iron Catalysts.* Industrial & Engineering Chemistry Research, 1999. **38**(4): p. 1277-1290.
46. Nowicki, L., S. Ledakowicz, and D. B. Bukur, *Hydrocarbon selectivity model for the slurry phase Fischer–Tropsch synthesis on precipitated iron catalysts.* Chemical Engineering Science, 2001. **56**(3): p. 1175-1180.
47. Zimmerman, W., D. Bukur, and S. Ledakowicz, *Kinetic model of fischer-tropsch synthesis selectivity in the slurry phase.* Chemical Engineering Science, 1992. **47**(9): p. 2707-2712.
48. Todić, B.S., *Kinetic modeling and oprimization of fixed-bed reactor for Fischer-Tropsch synthesis*, 2015, Универзитет у Београду, Технолошко-металуршки факултет.

49. Zhang, Q., J. Kang, and Y. Wang, *Development of Novel Catalysts for Fischer–Tropsch Synthesis: Tuning the Product Selectivity.* ChemCatChem, 2010. **2**(9): p. 1030-1058.
50. Perego, C., R. Bortolo, and R. Zennaro, *Gas to liquids technologies for natural gas reserves valorization: The Eni experience.* Catalysis Today, 2009. **142**(1): p. 9-16.
51. Anderson, J.R. and M. Boudart, *Catalysis*. 1 ed. Catalysis. Vol. 2. 1981: Springer-Verlag Berlin Heidelberg.
52. Dry, M.E., *Practical and theoretical aspects of the catalytic Fischer-Tropsch process.* Applied Catalysis A: General, 1996. **138**(2): p. 319-344.
53. Sie, S.T. and R. Krishna, *Fundamentals and selection of advanced Fischer–Tropsch reactors.* Applied Catalysis A: General, 1999. **186**(1): p. 55-70.
54. Saeidi, S., et al., *Recent advances in reactors for low-temperature Fischer-Tropsch synthesis: process intensification perspective.* Reviews in Chemical Engineering, 2015. **31**(3): p. 209-238.
55. Stamenić, M., et al., *Multiscale and Multiphase Model of Fixed Bed Reactors for Fischer–Tropsch Synthesis: Intensification Possibilities Study.* Industrial & Engineering Chemistry Research, 2017. **56**(36): p. 9964-9979.
56. VANVUUREEN, D., *Fischer-Tropsch synthesis in slurry reactors: summary and analysis of the state of the art.* 1982.
57. Espinoza, R., et al., *Low temperature Fischer–Tropsch synthesis from a Sasol perspective.* Applied Catalysis A: General, 1999. **186**(1-2): p. 13-26.
58. Wender, I., *Reactions of synthesis gas.* Fuel Processing Technology, 1996. **48**(3): p. 189-297.
59. Steynberg, A., et al., *High temperature Fischer–Tropsch synthesis in commercial practice.* Applied Catalysis A: General, 1999. **186**(1-2): p. 41-54.
60. Steynberg, A., *Introduction to fischer-tropsch technology*, in *Studies in Surface Science and Catalysis*2004, Elsevier. p. 1-63.
61. Mandić, M., et al., *Effects of Catalyst Activity, Particle Size and Shape, and Process Conditions on Catalyst Effectiveness and Methane Selectivity for Fischer–Tropsch Reaction: A Modeling Study.* Industrial & Engineering Chemistry Research, 2017. **56**(10): p. 2733-2745.
62. Botes, F.G., J.W. Niemantsverdriet, and J. van de Loosdrecht, *A comparison of cobalt and iron based slurry phase Fischer–Tropsch synthesis.* Catalysis Today, 2013. **215**: p. 112-120.
63. Maretto, C. and R. Krishna, *Modelling of a bubble column slurry reactor for Fischer–Tropsch synthesis.* Catalysis today, 1999. **52**(2-3): p. 279-289.
64. Chabot, G., et al., *A mathematical modeling of catalytic milli-fixed bed reactor for Fischer–Tropsch synthesis: Influence of tube diameter on Fischer Tropsch selectivity and thermal behavior.* Chemical Engineering Science, 2015. **127**: p. 72-83.
65. Visconti, C.G., et al., *An experimental investigation of Fischer–Tropsch synthesis over washcoated metallic structured supports.* Applied Catalysis A: General, 2009. **370**(1-2): p. 93-101.

66. Abbaslou, R.M.M., J.S.S. Mohammadzadeh, and A.K. Dalai, *Review on Fischer–Tropsch synthesis in supercritical media.* Fuel Processing Technology, 2009. **90**(7-8): p. 849-856.
67. Mogalicherla, A.K. and N.O. Elbashir, *Development of a kinetic model for supercritical fluids fischer-tropsch synthesis.* Energy and Fuels, 2011. **25**(3): p. 878-889.
68. Yokota, K., Y. Hanakata, and K. Fujimoto, *Supercritical phase Fischer-Tropsch synthesis.* Chemical Engineering Science, 1990. **45**(8): p. 2743-2749.
69. Elbashir, N.O., et al., *Advancement of Fischer-Tropsch synthesis via utilization of supercritical fluid reaction media.* AIChE Journal, 2010. **56**(4): p. 997-1015.
70. Elbashir, N.O., et al., *Impact of cobalt-based catalyst characteristics on the performance of conventional gas-phase and supercritical-phase Fischer-Tropsch synthesis.* Applied Catalysis A: General, 2005. **285**(1-2): p. 169-180.
71. Elbashir, N.O. and C.B. Roberts, *Catalyst in Near-Critical and Supercritical Hexane Media.* 2005: p. 505-521.
72. Elbashir, N.O. and C.B. Roberts, *Enhanced incorporation of α-olefins in the Fischer-Tropsch synthesis chain-growth process over an alumina-supported cobalt catalyst in near-critical and supercritical hexane media.* Industrial & Engineering Chemistry Research, 2005. **44**(3): p. 505-521.
73. Kasht, A., et al., *Product Analysis of Supercritical Fischer-Tropsch Synthesis: Utilizing a Unique On-Line and Off-Line Gas Chromatographs Setup in a Bench-Scale Reactor Unit.* American Journal of Analytical Chemistry, 2015. **6**(8): p. 659.
74. Mogalicherla, A.K., E.E. Elmalik, and N.O. Elbashir, *Enhancement in the intraparticle diffusion in the supercritical phase fischer-tropsch synthesis.* Chemical Engineering and Processing: Process Intensification, 2012. **62**: p. 59-68.
75. Elbashir, N.O., B. Bao, and M.M. El-Halwagi. *An approach to the design of advanced Fischer-Tropsch reactor for operation in near-critical and supercritical phase media*. in *Proceedings of the 1st Annual Gas Processing Symposium*. 2009. Elsevier.
76. Jacobs, G., et al., *Fischer–Tropsch synthesis: supercritical conversion using a Co/Al2O3 catalyst in a fixed bed reactor☆.* Fuel, 2003. **82**(10): p. 1251-1260.
77. Bochniak, D.J. and B. Subramaniam, *Fischer-tropsch synthesis in near-critical n-hexane: Pressure-tuning effects.* AIChE Journal, 1998. **44**(8): p. 1889-1896.
78. Bukur, D.B., et al., *Effect of process conditions on olefin selectivity during conventional and supercritical Fischer− Tropsch synthesis.* Industrial & Engineering Chemistry Research, 1997. **36**(7): p. 2580-2587.
79. Lang, X., A. Akgerman, and D.B. Bukur, *Steady state Fischer-Tropsch synthesis in supercritical propane.* Industrial & Engineering Chemistry Research, 1995. **34**(1): p. 72-77.
80. Huang, X. and C.B. Roberts, *Selective Fischer–Tropsch synthesis over an Al2O3 supported cobalt catalyst in supercritical hexane.* Fuel Processing Technology, 2003. **83**(1-3): p. 81-99.

81. Yan, S., et al., *Supercritical-phase process for selective synthesis of heavy hydrocarbons from syngas on cobalt catalysts.* Applied Catalysis A: General, 1998. **171**(2): p. 247-254.
82. Irankhah, A. and A. Haghtalab, *Fischer-Tropsch Synthesis Over Co-Ru/γ-Al2O3 Catalyst in Supercritical Media.* Chemical Engineering & Technology: Industrial Chemistry-Plant Equipment-Process Engineering-Biotechnology, 2008. **31**(4): p. 525-536.
83. Yokota, K. and K. Fujimoto, *Supercritical-phase Fischer-Tropsch synthesis reaction. 2. The effective diffusion of reactant and products in the supercritical-phase reaction.* Industrial & Engineering Chemistry Research, 1991. **30**(1): p. 95-100.
84. Challiwala, M.S., et al., *Multidimensional modeling of a microfibrous entrapped cobalt catalyst Fischer-Tropsch reactor bed.* AIChE Journal, 2017. **64**(5): p. 1723-1731.
85. Sheng, M., et al., *Novel catalyst structures with enhanced heat transfer characteristics.* Journal of Catalysis, 2011. **281**(2): p. 254-262.
86. Kalluri, R.R., D.R. Cahela, and B.J. Tatarchuk, *Microfibrous entrapped small particle adsorbents for high efficiency heterogeneous contacting.* Separation and Purification Technology, 2008. **62**(2): p. 304-316.
87. Rados, N., M.H. Al-Dahhan, and M.P. Dudukovic, *Modeling of the Fischer–Tropsch synthesis in slurry bubble column reactors.* Catalysis Today, 2003. **79-80**: p. 211-218.
88. Nanduri, A. and P.L. Mills, *Comparison of Diffusion Flux Models for Fischer-Tropsch Synthesis.* Fuel. **1**: p. C2.
89. Wang, Y.-N., et al., *Modeling of catalyst pellets for Fischer-Tropsch synthesis.* Industrial & Engineering Chemistry Research, 2001. **40**(20): p. 4324-4335.
90. Jianmin, W., et al., *Diffusion and Reaction Model of Catalyst Pellets for Fischer-Tropsch Synthesis.* China Petroleum Processing and Petrochemical Tech nology, 2013. **15**(4): p. 77-86.
91. Mamonov, N., et al., *One-dimensional heterogeneous model of a Fischer-Tropsch synthesis reactor with a fixed catalyst bed in the isothermal granules approximation.* Catalysis in Industry, 2013. **5**(3): p. 223-231.
92. Hallac, B.B., et al., *An optimized simulation model for iron-based Fischer–Tropsch catalyst design: transfer limitations as functions of operating and design conditions.* Chemical Engineering Journal, 2015. **263**: p. 268-279.
93. Ghouri, M.M., et al., *Multi-scale modeling of fixed-bed Fischer Tropsch reactor.* Computers & Chemical Engineering, 2016. **91**: p. 38-48.
94. Hussain, R., et al., *Development of Gas-to-Liquid Technologies from Micro- to Macro-scale*, in *Excellence and Impact of Research at Texas A&M at Qatar*, M. Weichold, K.R. Hall, and E. Masad, Editors. 2013, QScience: Doha, Qatar. p. 55-78.
95. Elbashir, N.O., L. Bani Nassr, and M.M. Ghouri, *Gas-to-Liquid Technology Research at Texas A&M Qatar and its Potentials*, in *The Water-Food-Energy Nexus: Processes, Technologies, and Challenges*, I.M. Mujtaba, R. Srinivasan,

and N.O. Elbashir, Editors. 2017, CRC Press Taylor & Francis Group: Bota Racon, Florida, USA. p. 427-455.
96. Stamenić, M., et al., *Multiscale and Multiphase Model of Fixed-Bed Reactors for Fischer–Tropsch Synthesis: Optimization Study.* Industrial & Engineering Chemistry Research, 2018. **57**(9): p. 3149-3162.
97. Bukur, D.B., et al., *Pore diffusion effects on catalyst effectiveness and selectivity of cobalt based Fischer-Tropsch catalyst.* Catalysis Today, 2018.
98. Mandić, M., et al., *Dynamic analysis of millimetre-scale fixed bed reactors for Fischer-Tropsch synthesis.* Chemical Engineering Science, 2018. **192**: p. 434-447.
99. Bub, G., et al., *Prediction of the performance of catalytic fixed bed reactors for Fischer-Tropsch synthesis.* Chemical Engineering Science, 1980. **35**(1-2): p. 348-355.
100. Wang, Y.-N., et al., *Heterogeneous modeling for fixed-bed Fischer–Tropsch synthesis: Reactor model and its applications.* Chemical Engineering Science, 2003. **58**(3-6): p. 867-875.
101. Marvast, M.A., et al., *Fischer-Tropsch synthesis: modeling and performance study for Fe-HZSM5 bifunctional catalyst.* Chemical Engineering & Technology: Industrial Chemistry-Plant Equipment-Process Engineering-Biotechnology, 2005. **28**(1): p. 78-86.
102. Jess, A. and C. Kern, *Modeling of Multi-Tubular Reactors for Fischer-Tropsch Synthesis.* Chemical Engineering & Technology: Industrial Chemistry-Plant Equipment-Process Engineering-Biotechnology, 2009. **32**(8): p. 1164-1175.
103. Sharma, A., et al., *A simple and realistic fixed bed model for investigating Fischer–Tropsch catalyst activity at lab-scale and extrapolating to industrial conditions.* Chemical engineering science, 2011. **66**(24): p. 6358-6366.
104. Brunner, K.M., et al., *A trickle fixed-bed recycle reactor model for the Fischer-Tropsch synthesis.* International Journal of Chemical Reactor Engineering, 2012. **10**(1).
105. Kaiser, P. and A. Jess, *Modeling of multitubular reactors for Iron-and Cobalt-catalyzed Fischer–Tropsch syntheses for application in a power-to-liquid process.* Energy Technology, 2014. **2**(5): p. 486-497.
106. Moazami, N., et al., *Modelling of a fixed bed reactor for Fischer–Tropsch synthesis of simulated N2-rich syngas over Co/SiO2: Hydrocarbon production.* Fuel, 2015. **154**: p. 140-151.
107. Wang, Y.-N., et al., *Heterogeneous modeling for fixed-bed Fischer–Tropsch synthesis: Reactor model and its applications.* Chemical Engineering Science, 2003. **58**(3): p. 867-875.
108. Le Bars, M. and M.G. Worster, *Interfacial conditions between a pure fluid and a porous medium: implications for binary alloy solidification.* Journal of Fluid Mechanics, 2006. **550**: p. 149-173.
109. Nield, D.A., *The limitations of the Brinkman-Forchheimer equation in modeling flow in a saturated porous medium and at an interface.* International Journal of Heat and Fluid Flow, 1991. **12**(3): p. 269-272.

110. Sheng, M., et al., *High conductivity catalyst structures for applications in exothermic reactions.* Applied Catalysis A: General, 2012. **445**: p. 143-152.
111. Hicks, R.E., *Pressure Drop in Packed Beds of Spheres.* Industrial & Engineering Chemistry Fundamentals, 1970. **9**(3): p. 500-502.
112. Fuller, E.N., P.D. Schettler, and J.C. Giddings, *New method for prediction of binary gas-phase diffusion coefficients.* Industrial & Engineering Chemistry, 1966. **58**(5): p. 18-27.
113. Yates, I.C. and C.N. Satterfield, *Intrinsic kinetics of the Fischer-Tropsch synthesis on a cobalt catalyst.* Energy & Fuels, 1991. **5**(1): p. 168-173.
114. Vervloet, D., et al., *Fischer–Tropsch reaction–diffusion in a cobalt catalyst particle: aspects of activity and selectivity for a variable chain growth probability.* Catalysis Science & Technology, 2012. **2**(6): p. 1221-1233.
115. Maretto, C. and R. Krishna, *Design and optimisation of a multi-stage bubble column slurry reactor for Fischer–Tropsch synthesis.* Catalysis Today, 2001. **66**(2-4): p. 241-248.
116. Ma, W., et al., *Fischer–Tropsch Synthesis: Kinetics and Water Effect on Methane Formation over 25% Co/γ-Al2O3 Catalyst.* Industrial & Engineering Chemistry Research, 2014. **53**(6): p. 2157-2166.
117. Storsæter, S., et al., *Study of the effect of water on Fischer–Tropsch synthesis over supported cobalt catalysts.* Journal of Catalysis, 2005. **231**(2): p. 405-419.
118. Schulz, H., M. Claeys, and S. Harms, *Effect of water partial pressure on steady state Fischer-Tropsch activity and selectivity of a promoted cobalt catalyst*, in *Studies in Surface Science and Catalysis*1997, Elsevier. p. 193-200.
119. Botes, F.G., *Influences of water and syngas partial pressure on the kinetics of a commercial alumina-supported cobalt Fischer− Tropsch catalyst.* Industrial & Engineering Chemistry Research, 2009. **48**(4): p. 1859-1865.
120. Bukur, D.B., et al., *Effect of CO Conversion on the Product Distribution of a Co/Al2O3 Fischer–Tropsch Synthesis Catalyst Using a Fixed Bed Reactor.* Catalysis Letters, 2012. **142**(11): p. 1382-1387.
121. Poling, B.E., J.M. Prausnitz, and J.P. O'Connell, *Pressure–volume–temperature relationship of pure gases and liquids.* The Properties of Gases and Liquids, McGraw Hill Book Co., New York, 2000: p. 33-34.
122. Yaws, C.L., *Yaws' Transport Properties of Chemicals and Hydrocarbons (Electronic Edition)*, Knovel.
123. Yaws, C.L., *Yaws' Critical Property Data for Chemical Engineers and Chemists*2012: Knovel.
124. Tobiś, J. and D. Ziółkowski, *Modelling of heat transfer at the wall of a packed-bed apparatus.* Chemical engineering science, 1988. **43**(11): p. 3031-3036.
125. Bunnell, D., et al., *Effective thermal conductivities in gas-solid systems.* Industrial & Engineering Chemistry, 1949. **41**(9): p. 1977-1981.
126. Campbell, J. and R. Huntington, *Part II.* Heat Transfer and Temperature Gradients, Petroleum Refiner, 1952. **31**(2): p. 123-131.
127. De Wasch, A. and G. Froment, *Heat transfer in packed beds.* Chemical engineering science, 1972. **27**(3): p. 567-576.

128. Specchia, V., G. Baldi, and S. Sicardi, *Heat transfer in packed bed reactors with one phase flow.* Chemical Engineering Communications, 1980. **4**(1-3): p. 361-380.
129. Bauer, R., *Effective radial thermal conductivity of packings in gas flow.* Int. Chem. Eng., 1978. **18**: p. 181-204.
130. Dixon, A.G., *Wall and particle-shape effects on heat transfer in packed beds.* Chemical Engineering Communications, 1988. **71**(1): p. 217-237.
131. Specchia, V. and S. Sicardi, *Modified Correlation for the Conductive Contribution of Thermal Conductivity in Packed Bed Reactors.* Chemical Engineering Communications, 1980. **6**(1-3): p. 131-139.
132. Plautz, D.A. and H. Johnstone, *Heat and mass transfer in packed beds.* AIChE Journal, 1955. **1**(2): p. 193-199.
133. Quinton, J. and J.A. Storrow, *Heat transfer to air flowing through packed tubes.* Chemical engineering science, 1956. **5**(6): p. 245-257.
134. Kunii, D. and J. Smith, *Heat transfer characteristics of porous rocks.* AIChE Journal, 1960. **6**(1): p. 71-78.
135. Benyahia, F. and K.E. O'Neill, *Enhanced Voidage Correlations for Packed Beds of Various Particle Shapes and Sizes.* Particulate Science and Technology, 2005. **23**: p. 169-177.
136. Nemec, D. and J. Levec, *Flow through packed bed reactors: 1. Single-phase flow.* Chemical Engineering Science, 2005. **60**(24): p. 6947-6957.
137. Elbashir, N.O., et al., *Reaction pathway and kinetic modeling of Fischer-Tropsch synthesis over an alumina supported cobalt catalyst in supercritical-hexane media.* C1 Chemistry for the Production of Ultra-Clean Liquid Transportation Fuels and Hydrogen, 2004: p. 14.
138. Yermakova, A. and V.I. Anikeev, *Thermodynamic calculations in the modeling of multiphase processes and reactors.* Industrial & Engineering Chemistry Research, 2000. **39**(5): p. 1453-1472.
139. Ermakova, A., V. Anikeev, and G. Froment, *Supercritical Fischer-Tropsch synthesis: The effect of nonideality of the reaction mixture on the reaction rate.* Theoretical Foundations of Chemical Engineering, 2000. **34**(2): p. 180-188.
140. Elmalik, E., et al., *Tropsch synthesis phase behavior in non-conventional reaction media.* Preprint Paper-American Chemical Society, Division of Fuel Chemistry, 2010. **55**(2): p. 173-175.
141. WebBook, N., *Thermophysical properties of fluid systems.* Avaliable Online: http://webbook. nist. gov/chemistry/fluid/(access on 18 January 2015), 2016.
142. Chernobaev, I., et al., *Investigation of the mechanism of methane formation in the fischer-tropsch synthesis on a Co/SiO 2· Zr IV catalyst.* Theoretical and Experimental Chemistry, 1997. **33**(1): p. 38-40.
143. Lee, W.H. and C.H. Bartholomew, *Multiple reaction states in CO hydrogenation on alumina-supported cobalt catalysts.* Journal of Catalysis, 1989. **120**(1): p. 256-271.

144. Sheng, M., et al., *Micro scale heat transfer comparison between packed beds and microfibrous entrapped catalysts.* Engineering Applications of Computational Fluid Mechanics, 2013. **7**(4): p. 471-485.
145. Challiwala, M.S., et al. *Kinetic and Thermodynamic Modelling of Methane Reforming Technologies: Comparison of Conventional Technologies with Dry Reforming*. in *2015 AIChE Annual Meeting*. 2015.
146. Challiwala, M.S., et al., *A Process Integration Approach to the Optimization of CO2 Utilization via Tri-Reforming of Methane*, in *Computer Aided Chemical Engineering*, A. Espuña, M. Graells, and L. Puigjaner, Editors. 2017, Elsevier. p. 1993-1998.
147. Saib, A.M., et al., *XANES study of the susceptibility of nano-sized cobalt crystallites to oxidation during realistic Fischer–Tropsch synthesis.* Applied Catalysis A: General, 2006. **312**: p. 12-19.
148. Elbashir, N.O. and C.B. Roberts, *Enhanced Incorporation of α-Olefins in the Fischer− Tropsch Synthesis Chain-Growth Process over an Alumina-Supported Cobalt Catalyst in Near-Critical and Supercritical Hexane Media.* Industrial & Engineering Chemistry Research, 2005. **44**(3): p. 505-521.
149. Tang, H., et al., *Supercritical Phase Fischer-Tropsch Synthesis Reaction over Highly Active Fused Iron Catalyst at Low Temperature.* Chinese Journal of Catalysis, 2008. **29**(2): p. 174.
150. Van Der Laan, G.P. and A. Beenackers, *Kinetics and selectivity of the Fischer–Tropsch synthesis: a literature review.* Catalysis Reviews, 1999. **41**(3-4): p. 255-318.
151. Huang, X., N.O. Elbashir, and C.B. Roberts, *Supercritical solvent effects on hydrocarbon product distributions from Fischer− Tropsch synthesis over an alumina-supported cobalt catalyst.* Industrial & Engineering Chemistry Research, 2004. **43**(20): p. 6369-6381.
152. Katbeh, T., N.O. Elbashir, and M. El-Halwagi, *An Energy Integrated Approach to Design Supercritical Fischer-Tropsch Synthesis Products Separation and Solvent Recovery System*, 2017.

APPENDIX A

PHYSICAL PROPERTIES CONSTANTS

Table 10: Heat capacity data of the species involved in the FT reaction

Formula	A	B	C	D	E	F	G
CH_4	44.357	-0.146	0.001	-8.74114E-07	6.78119E-10	-2.75382E-13	4.58066E-17
C_2H_4	47.318	-0.233	0.001	-2.22415E-06	2.01328E-09	-9.14455E-13	1.65116E-16
C_2H_6	45.660	-0.174	0.001	-1.93472E-06	1.70253E-09	-7.57352E-13	1.3474E-16
C_3H_6	43.224	-0.116	0.001	-2.01754E-06	1.8262E-09	-8.25379E-13	1.48304E-16
C_3H_8	49.791	-0.175	0.001	-2.75763E-06	2.51004E-09	-1.14034E-12	2.05755E-16
C_4H_8	52.945	-0.148	0.002	-2.8819E-06	2.63853E-09	-1.20072E-12	2.16678E-16
C_4H_{10}	80.786	-0.344	0.002	-4.28095E-06	3.89618E-09	-1.77236E-12	3.2021E-16
C_5H_{10}	55.436	0.068	0.001	-1.26736E-06	1.06181E-09	-4.73549E-13	8.94319E-17
C_5H_{12}	68.343	-0.149	0.002	-3.50024E-06	3.1436E-09	-1.41672E-12	2.55785E-16
C_6H_{12}	76.073	-0.045	0.001	-2.6233E-06	2.35229E-09	-1.08563E-12	2.04388E-16
C_6H_{14}	86.846	-0.255	0.003	-4.98515E-06	4.63408E-09	-2.16831E-12	4.07245E-16

Table 10 continued

Formula	A	B	C	D	E	F	G
C_7H_{14}	115.511	-0.628	0.004	-7.38174E-06	6.98506E-09	-3.30999E-12	6.2286E-16
C_7H_{16}	99.515	-0.275	0.003	-5.30451E-06	4.65818E-09	-2.02447E-12	3.48821E-16
C_8H_{16}	93.185	0.071	0.001	-2.37156E-06	2.00115E-09	-8.86976E-13	1.64712E-16
C_8H_{18}	111.038	-0.278	0.003	-5.44158E-06	4.47476E-09	-1.76528E-12	2.64998E-16
C_9H_{18}	119.737	1.085	-0.003	3.9692E-06	0.000	193.000	534.000
C_9H_{20}	1215.200	-11.498	0.049	-8.88014E-05	5.95478E-08	223.150	575.000
$C_{10}H_{20}$	137.962	1.193	-0.003	0.000	0.000	208.000	555.000
$C_{10}H_{22}$	1518.403	-14.031	0.057	-9.88927E-05	6.32141E-08	248.150	600.000
$C_{11}H_{22}$	131.914	1.366	-0.004	4.0918E-06	0.000	225.000	574.000
$C_{11}H_{24}$	-406.276	8.721	-0.039	7.79639E-05	-5.47661E-08	260.360	486.072
$C_{12}H_{24}$	129.203	1.584	-0.004	4.3851E-06	0.000	239.000	591.000
$C_{12}H_{26}$	2293.071	-22.318	0.092	0.000	1.0619E-07	268.370	506.323

Table 10 continued

Formula	A	B	C	D	E	F	G
$C_{13}H_{26}$	218.250	1.251	-0.003	3.75921E-06	0.000	250.080	590.465
$C_{13}H_{28}$	2509.025	-23.656	0.093	0.000	9.2264E-08	270.455	525.258
$C_{14}H_{28}$	231.627	1.383	-0.003	3.95339E-06	0.000	260.300	608.125
$C_{14}H_{30}$	719.546	-2.534	0.006	5.24379E-07	-5.14638E-09	286.080	543.357
$C_{15}H_{30}$	236.166	1.495	-0.004	4.08667E-06	0.000	269.420	624.805
$C_{15}H_{32}$	1975.876	-15.999	0.059	-9.1333E-05	5.24954E-08	288.110	560.247
$C_{19}H_{40}$	352.720	1.639	-0.004	4.30892E-06	0.000	0.000	0.000
$C_{22}H_{46}$	-69.933	4.884	-0.010	8.08276E-06	0.000	0.000	0.000
CO	28.505	0.010	-6.15947E-05	1.61354E-07	-1.78138E-10	9.02011E-14	-1.73591E-17
H_2	19.671	0.070	0.000	2.89493E-07	-2.22475E-10	8.81466E-14	-1.42043E-17
H_2O	33.174	-0.003	1.74365E-05	-5.97958E-09	0.000	0.000	0.000
N_2	28.717	0.007	-4.54759E-05	1.16406E-07	-1.22458E-10	5.90449E-14	-1.08748E-17

Table 11: Viscosity data of the species involved in the FT reaction

Formula	A	B	C	D
CH_4	1.26029	0.438036	-0.00024	7.09807E-08
C_2H_4	-8.59541	0.430624	-0.0002	5.34529E-08
C_2H_6	-0.48129	0.343853	-9.09809E-05	1.15419E-08
C_3H_6	-12.6908	0.384707	-0.00018	4.74312E-08
C_3H_8	-9.15355	0.359103	-0.00018	5.40963E-08
C_4H_8	-11.2711	0.334807	-0.00013	3.1182E-08
C_4H_{10}	-9.37493	0.329787	-0.00014	3.64505E-08
C_5H_{10}	-10.6788	0.2968	-8.35656E-05	1.3935E-08
C_5H_{12}	-8.06254	0.298811	-0.00013	3.34301E-08
C_6H_{12}	-8.82234	0.265083	-6.01975E-05	6.90513E-09
C_6H_{14}	-12.2389	0.287213	-0.0001	2.29109E-08
C_7H_{14}	-7.00332	0.239124	-4.10754E-05	1.14593E-09
C_7H_{16}	-11.8801	0.2547	-7.74146E-05	1.60079E-08
C_8H_{16}	-5.3211	0.216044	-2.54747E-05	-3.4121E-09
C_8H_{18}	7.86176	0.137989	7.83185E-05	-4.5043E-08
C_9H_{18}	-6.5557	993.5	0.014232	-1.4097E-05
C_9H_{20}	-6.0742	968.61	0.012677	-1.2675E-05
$C_{10}H_{20}$	-6.8845	1100.3	0.014341	-1.352E-05
$C_{10}H_{22}$	-6.0716	1017.7	0.012247	-1.1892E-05
$C_{11}H_{22}$	-7.1496	1171.3	0.014798	-1.3604E-05
$C_{11}H_{24}$	-6.7868	1168.2	0.013438	-1.2334E-05
$C_{12}H_{24}$	-7.46	1260.3	0.015116	-1.3452E-05
$C_{12}H_{26}$	-7.0687	1253	0.013735	-1.2215E-05

Table 11 continued

Formula	**A**	**B**	**C**	**D**
$C_{13}H_{26}$	-3.8333	929.42	0.003368	-1.2409E-06
$C_{13}H_{28}$	-7.2994	1324.8	0.013974	-1.2097E-05
$C_{14}H_{28}$	-6.731	1266.6	0.012388	-1.0611E-05
$C_{14}H_{30}$	-7.8717	1446.7	0.01494	-1.2495E-05
$C_{15}H_{30}$	-9.0123	1585.3	0.017951	-1.4746E-05
$C_{15}H_{32}$	-7.8643	1479.8	0.01472	-1.2148E-05
CO	18.0493	0.63753	-0.000357478	1.02867E-07
H_2	1.76113	0.341655	-0.000183676	5.11475E-08
H_2O	22.821	0.173868	0.000324648	-1.43337E-07
N_2	4.46556	0.638138	-0.000265956	5.41127E-08

Table 12: Thermal conductivity data of the species involved in the FT reaction

Formula	A	B	C	D
CH_4	0.00537671	5.15551E-05	1.66549E-07	-5.71678E-11
C_2H_4	-0.0118814	9.97294E-05	5.78107E-08	-2.26757E-11
C_2H_6	-0.00795306	7.36658E-05	1.13642E-07	-4.07229E-11
C_3H_6	-0.000355317	3.65555E-05	1.12921E-07	-5.14716E-11
C_3H_8	-0.00404765	2.5353E-05	1.88793E-07	-7.97671E-11
C_4H_8	0.00577394	-3.63424E-05	2.46986E-07	-9.43517E-11
C_4H_{10}	-0.00999135	5.73291E-05	1.12619E-07	-4.46874E-11
C_5H_{10}	-0.0104154	5.85832E-05	1.04267E-07	-3.75487E-11
C_5H_{10}	-0.0164692	8.53295E-05	5.6164E-08	-2.14684E-11
C_5H_{12}	-0.00373594	2.92584E-05	1.33259E-07	-5.20996E-11
C_6H_{12}	-0.00417947	2.45838E-05	1.24652E-07	-4.58896E-11
C_6H_{14}	-0.00768012	3.80097E-05	1.13181E-07	-4.01573E-11
C_7H_{14}	-0.00614471	2.5453E-05	1.25695E-07	-4.51341E-11
C_7H_{16}	-0.0107511	5.08345E-05	8.98372E-08	-3.66275E-11
C_8H_{16}	-0.00349329	9.29215E-06	1.46334E-07	-5.52491E-11
C_8H_{18}	-0.00531282	2.89236E-05	1.07213E-07	-3.9885E-11
C_9H_{18}	0.2	-0.00026	0	0
C_9H_{20}	0.199676	-0.000200253	-1.00196E-07	0
$C_{10}H_{20}$	0.195	-0.00023	0	0
$C_{10}H_{22}$	0.221594	-0.0003256	1.12824E-07	0
$C_{11}H_{22}$	0.19	-0.000219355	0	0
$C_{11}H_{24}$	0.231209	-0.000376575	2.5E-07	0
$C_{12}H_{24}$	0.195	-0.000213333	0	0
$C_{12}H_{26}$	0.22921	-0.00035926	2E-07	0

Table 12 continued

Formula	A	B	C	D
$C_{13}H_{26}$	0.188	-0.000193333	0	0
$C_{13}H_{28}$	0.19663	-0.0002	0	0
$C_{14}H_{28}$	0.19	-0.000183333	0	0
$C_{14}H_{30}$	0.19563	-0.0002	0	0
$C_{15}H_{30}$	0.192	-0.00019	0	0
$C_{15}H_{32}$	0.19963	-0.0002	-9.25186E-22	0
CO	9.40E-05	-4.08E-08	1.38E-11	0
H_2	0.000664106	-3.44E-07	9.73E-11	0
H_2O	1.57E-05	1.01E-07	-2.43E-11	0
N_2	0.00010746	-6.02E-08	2.23E-11	0

APPENDIX B

MODELING CALCULATIONS

The Gas Hourly Space Velocity (GHSV) for the SCF-FT case was calculated at reactor conditions due to the fact that hexane exists in the liquid phase at STP conditions. The calculations are done as follows:

The number of moles of syngas (n_{syngas}) entering the reactor system was calculated using the ideal gas law as follows:

$$n_{syngas} = \frac{P_{syngas} \times Q_{syngas,stp}}{R \times T_s} \tag{108}$$

where P_{syngas} is the partial pressure of syngas (20 bar) and $Q_{syngas,stp}$ is the volumetric flow rate of syngas at STP conditions, R is the universal gas constant and T_s is the standard temperature (273.15 K).

The number of moles of supercritical solvent hexane (n_{hexane}) entering the reactor system are calculated using the solvent to syngas ratio (3:1).

$$n_{hexane} = 3 \times n_{syngas} \tag{109}$$

The volumetric flow rate of hexane ($Q_{hexanei\_nlet}$) at the reactor inlet conditions is calculated using the ideal gas law.

$$Q_{hexane} = \frac{n_{hexane} \times \mathrm{R} \times T_{inlet}}{P_{hexane}} \tag{110}$$

where P_{hexane} is the partial pressure of hexane and T_{inlet} is the temperature as the reactor inlet. The volumetric flow rate of syngas at reactor conditions ($Q_{syngas,inlet}$) is calculated in a similar manner.

The GHSV was calculated as an inverse of the residence time which was calculated as follows:

$$\text{Residence time} = \frac{V_{reactor}}{Q_{hexane,inlet} + Q_{syngas,inlet}} \quad (111)$$

The GHSV is then defined as:

$$\text{GHSV} = \frac{1}{\text{Residence time}} \quad (112)$$